©Copyright 2014

Nicholas Walker Bigelow

Electron Energy-Loss Spectroscopy

Theory and Simulation

Applied to Nanoparticle Plasmonics

Nicholas Walker Bigelow

A dissertation
submitted in partial fulfilment of the
requirements for the degree of

Doctor of Philosophy

University of Washington
2014

Reading Committee:

David J. Masiello

Lutz Maibaum

Gary Drobny

Program Authorized to Offer Degree:

Chemistry

University of Washington

Abstract

Electron Energy-Loss Spectroscopy Theory and Simulation

Applied to Nanoparticle Plasmonics

Nicholas Walker Bigelow

Chair of the Supervisory Committee:

Assistant Professor David J. Masiello

Department of Chemistry

The vast array of potential applications for plasmons has laid bare the need for a detailed understanding of the complex interactions that occur between multiple plasmons and between plasmons and near-field probes. In this dissertation, the capacity of electron energy-loss spectroscopy (EELS) to probe plasmons is examined in detail. EELS is shown to be able to detect both electric hot spots and Fano resonances in contrast to the prevailing knowledge prior to this work. The most detailed examination of magnetoplasmonic resonances in multi-ring structures to date and the utility of electron tomography to computational plasmonics is explored, and a new tomographic method for the reconstruction of a target is introduced.

Since the observation of single-molecule surface-enhanced Raman scattering (SMSERS) in 1997, questions regarding the nature of the electromagnetic hot spots responsible for such observations still persist. A computational analysis of the electron- and photon-driven surface-plasmon resonances of monomer and dimer metal nanorods is presented to elucidate the differences and similarities between the two excitation mechanisms in a system with well understood optical properties. By correlating the nanostructure's simulated electron energy loss spectrum and loss-probability maps with its induced polarization and scattered electric field we discern how certain plasmon modes are selectively excited and how they funnel energy from the excitation source into the near- and far-field. Using a fully retarded electron-scattering theory capable of describing arbitrary three-dimensional nanoparticle geometries, aggregation schemes, and material compositions, we find that electron energy-loss spectroscopy (EELS) is able to *indirectly* probe the same electromagnetic hot spots that are generated by an optical excitation source. EELS is then employed in a scanning transmission electron microscope (STEM) to obtain maps of the localized surface plasmon modes of SMSERS-active nanostructures, which are resolved in both space and energy. Single-molecule character is confirmed by the bianalyte approach using two isotopologues of Rhodamine 6G. The origins of this observation are explored using a fully three-dimensional electrodynamics simulation of both the electron energy loss probability and the near-electric field enhancements. The calculations suggest that electron beam excitation of the hot spot is possible, but only when the electron beam is located outside of the junction region, and further that the location of the hot spot can be inferred from the node in the loss probability in the junction along with the high loss probability on the edges away from the junction.

The optical-frequency magnetic and electric properties of cyclic aromatic plasmon-supporting metal nanoparticle oligomers are explored through a combination of STEM/EELS simulation and first-principles theory. A tight-binding type model is introduced to explore the rich hybridization physics in these plasmonic systems and tested with full-wave numerical electrodynamics simulations of the STEM electron probe. Building from a microscopic electric model, connection is made at the macroscopic level between the hybridization of localized magnetic moments into delocalized magnetic plasmons of controllable magnetic order and the mixing of atomic p_z orbitals into delocalized π molecular orbitals of varying nodal structure spanning the molecule. It is found that the STEM electrons are uniquely capable of exciting all of the different hybridized eigenmodes of the nanoparticle assembly—including multipolar closed-loop ferromagnetic and antiferromagnetic plasmons, giant electric dipole resonances, and radial breathing modes—by raster scanning the beam to the appropriate position. Comparison to plane wave light scattering and cathodoluminescence (CL) spectroscopy is made. The presented work provides a unified understanding of the complete plasmon eigenstructure of such oligomer systems as well as of the excitation conditions necessary to probe each mode.

Through numerical simulation, we predict the existence of the Fano interference effect in the EELS and CL of symmetry-broken nanorod dimers that are heterogeneous in material composition and asymmetric in length. The differing selection rules of the electron probe in comparison to the photon of a plane wave allow for the simultaneous excitation of both optically bright and dark plasmons of each monomer unit, suggesting that Fano resonances will not arise in EELS and CL. Yet, interferences are manifested in the dimer's scattered near-

and far-fields and are evident in EELS and CL due to the rapid π-phase offset in the polarizations between super-radiant and sub-radiant hybridized plasmon modes of the dimer as a function of the energy loss suffered by the impinging electron. Depending upon the location of the electron beam, we demonstrate the conditions under which Fano interferences will be present in both optical and electron spectroscopies (EELS and CL) as well as a new class of Fano interferences that are uniquely electron-driven and are absent in the optical response. Among other things, the knowledge gained from this work bears impact upon the design of some of the world's most sensitive sensors, which are currently based upon Fano resonances. The Fano interference phenomenon between localized surface plasmon resonances (LSPRs) of individual silver nanocubes is then investigated experimentally using dark-field optical microscopy and electron energy-loss spectroscopy (EELS) in a scanning transmission electron microscope (STEM). By computing the polarization induced by the electron beam, we show that the hybridized modes responsible for this Fano interference are the same as those present in the resonance-Rayleigh scattering spectrum of an individual nanocube on a substrate.

Finally, a group of five semi-collinear nanoparticles are modeled both by making a guess as to the third dimension from a single top-down electron micrograph and also through electron tomography. The former technique is the conventional modeling method most often employed in creating computational models of plasmonic targets, though it is akin to modeling a sky scraper from a satellite picture of the roof. Electron tomography offers a way to reconstruct the particles fully, with a minimal amount of guesswork. The degree of similarity between the computed properties of the target built through the two different methods is examined,

as are the targets themselves. It is shown that purely far-field properties, such as the optical scattering are largely unaffected, but near-field properties, which are highly dependent on the fine-scale structure of the targets, differ considerably depending on which modeling method is employed. This work suggests that caution should be used by the theoretician when attempting to model the near-field of a physical structure, and that electron tomography offers an attractive way to overcome the problem of the third dimension.

Contents

List of Figures

GLOSSARY

AXSIA: Automated eXpert Spectral Image Analysis

CAT: Computed Axial Tomography

CL: Cathodoluminescence

EEL: Electron Energy Loss

EELS: Electron Energy Loss Spectroscopy

EM: Electromagnetic

FR: Fano Resonance

HAADF: High Angle Annular Dark Field

IR: Infrared

LDOS: Local Density Of States

LSPR: Localized Surface Plasmon Resonance

MRI: Magnetic Resonance Imaging

MVSA: Multivariate Statistical Analysis

NP: Nanoparticle

PCA: Principal Component Analysis

PET: Positron Emission Tomography

SERS: Surface-Enhanced Raman Scattering

SMSERS: Single-Molecule Surface-Enhanced Raman Scattering

SPP: Surface Plasma Polariton

SPR: Surface Plasmon Resonance

STEM: Scanning Transmission Electron Microscope

TEM: Transmission Electron Microscope

UV: Ultraviolet

VIS: Visible

ACKNOWLEDGEMENTS

There are so many people who have helped me throughout my academic career that it would be foolish to think that I could properly thank them all. I will attempt to thank as many as I can, here at the end of my schooling. Without the aid of the people enumerated here, and many more that are not, none of this work would have been possible.

First and foremost, I would like to thank my family who have supported me throughout my life. From the time I was old enough to express an interest in the natural world to the present day, they have been unwavering in their support and love. For three decades they have stood by me through all the highs and lows of my life. I do not have the words to express the depth of my gratitude to my parents, Deborah Sue and William Robert Bigelow, my grandparents, my late cousin A. Wallace Engstrom III, my uncles Roy and Dennis, and so many more.

I am also infinitely indebted to Dr. David Masiello, my advisor, whose constant mentorship has shepherded me to the successful completion of this body of work. His leadership, knowledge, and direction have been invaluable to me. Dr. Masiello invited me into his research group when I was only just beginning my work in graduate school, still working on remembering how to do basic calculus, and he has seen me through the challenges and successes that have gotten me to this point today. It would be remiss of me to fail to mention the other members of the Masiello group who have supported me and whose names appear with mine on these papers: Dr. Charles Cherqui, Niket Thakkar, Tim Sooter, Steven Quillin, Ross Grimshaw, Jonathan Litz, Christopher Baldwin, Panu Sam-ang, Harrison Goldwyn,

and Steven Spackman. Without the many fruitful conversations, significant contributions, and general support you have given me this work would not have been possible. I am deeply indebted to our experimental collaborators Dr. Jon Camden, Vigter Iberi, Philip Simmons, and Guoliang Li whose work challenges and supports my own. I would also like to thank the other grad students in the theory suite, Patrick Lestrange, Dr. Joseph May, Dr. Benjamin Van Kuiken, and so many more. A special thanks to Alex Vaschillo, who as an undergraduate worked with me on my first three papers and without whose programming experience, none of which would have been possible.

I thank Dr. Rose Ann Cattolico, who serves both as my Graduate School Representative and was previously my boss and mentor in my analytical chemistry work prior to returning to graduate school. It was Dr. Cattolico who encouraged me to return to school to pursue my PhD in 2009, and without her encouragement, I would probably still be saying "someday" to a PhD.

I am deeply indebted to the rest of my committee as well, Drs. Lutz Maibaum, Sarah Keller, Bruce Robinson, and Gary Drobny, for their guidance and wisdom. I would also like to thank Dr. William Reinhardt, who was on my general exam committee and is now enjoying being emeritus in the other Washington for being both a committee member and a mentor.

A special thanks goes out to Dr. Lewis Johnson, my partner in crime since we first tried to build an electromagnetic mass driver in middle school and who returned to Seattle to attend graduate school in theoretical chemistry here at the UW with me.

I would also like to thank my teachers and fellow students in my undergraduate career and before. In particular, Dr. Xiaosong Li, whose excellent undergraduate class in quantum mechanics first ignited my love of physical chemistry, and again Dr. Bruce Robinson, in whose lab I got my first taste of both theoretical chemistry research and programming.

There have been a great number of other teachers and mentors who do not fall into the groups already listed. Dr. James Farr at NOAA and the late Dr. Roland Anderson for their friendship and support. My teachers Ann Titterington, Whitney Tjerandsen, Brian Chapman, Mark Terry, Paul Raymond, and so many others that aren't listed here.

Last, I'd like to apologize to my girlfriend, MacKenzie, who has somehow put up with me through the last four and a half years of graduate school. To commit to a relationship with a graduate student at the start of their PhD is a special kind of masochism, and I couldn't have done it without her support.

to my parents

Chapter 1

Introduction

1.1 Surface plasmons

The interaction of optical-frequency light and metal nanoparticles has been used by humans for millennia to produce colored glass [1], but it was not until 1857 that the underlying cause of the glass to assume various colors when mixed with small fractions of silver and/or gold was discovered by Faraday [2], who explained the coloration as scattering of light off small particles of metal. However, the reason they expressed specific colors was not fully understood at that time.

The nature of the collective optical excitation of the conduction electrons in a metal was first explored by Ritchie in 1957 [3]. These collective electron excitations and can be described as quasi-particles known as plasma polaritons, or simply "plasmons" [4, 5]. The world would have to wait another five years before detailed experimental results were published for plasmons living on the surface of a metal nanoparticle [6], though an understanding of the

Figure 1.1: The Lycurgus cup contains plasmon-supporting silver and gold nanoparticles that cause it to appear green in reflection and red in transmission. Photo credit: Johnbod.

electromagnetic response of a perfect sphere with a given dielectric function had existed since Mie in 1908 [7]. A more detailed look at the surface plasmons of individual nanoparticles followed throughout the next several years [8–10]. After a period of relative inactivity, optical frequency excitations of conduction electrons in nanostructures have enjoyed a rapid growth in research interest in the past decade [11], as plasmons have found use in photovoltaics [12–17], chemical sensing [18–21], ultramicroscopy [22–24], medicine [25–27], and many other applications. A full understanding of plasmonic behavior is necessary to realize their potential, and many problems remain unexplored in the field of plasmonics, particularly in the complex interactions between plasmons that occur in aggregates of several plasmon-supporting nanoparticles.

Recently, attention has focused on a form of resonant energy transfer known as the Fano resonance, in which energy from one plasmon is transferred to another in the near-field. If the frequency of interrogating light is below the energy of the Fano resonance, then the energy transfer will occur with the two plasmons in phase and the effect will be constructive, forming a "bright" mode. Above the energy of the Fano resonance, the transfer will be out of phase and thus the effect will be destructive and a "dark" mode will occur. Transitions between bright and dark states can be sudden, with less than 0.1 eV separating them, making plasmonic Fano resonances very appealing as sensors of the dielectric environment [28–30]. Further, plasmonic nanoparticles arranged in rings may support collective plasmonic modes which set up a circulating oscillatory current and thus a corresponding linear magnetic field normal to the plane of the particles. These strong magnetic responses live at optical frequencies and similar materials are found nowhere in nature.

1.2 Electron spectroscopies performed in an electron microscope

1.2.1 Electron energy-loss spectroscopy

Traditional experimental methods for probing plasmonic behavior rely on excitation by and then measurement of optical far-field light. This method provides excellent sensitivity in frequency, but the spatial resolution is limited by diffraction to approximately one-half wavelength of the interrogating light, which is on the order of 100s of nm, several times larger

than the structure of the plasmons which is on the order of 10s of nm [11].

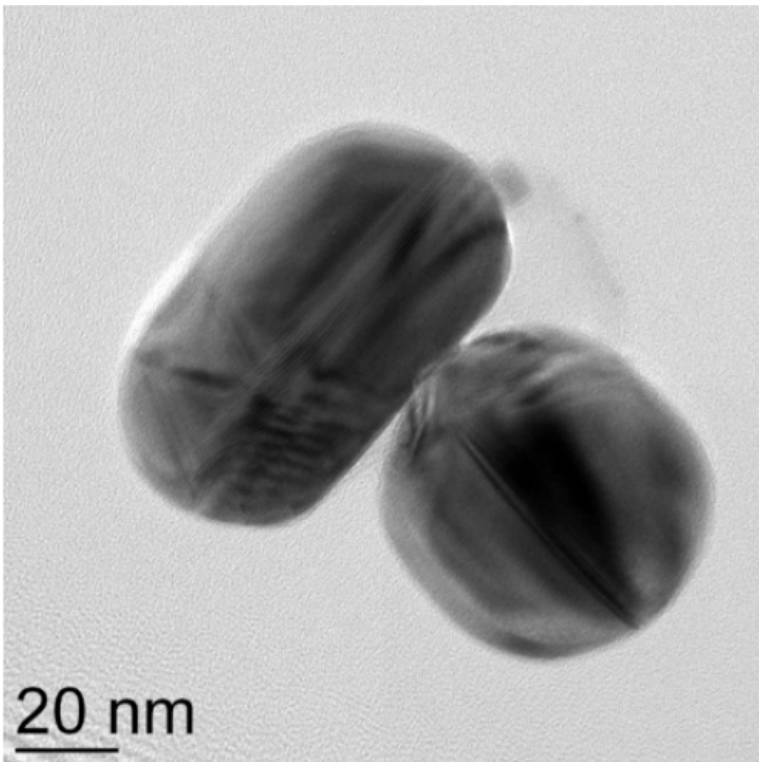

Figure 1.2: Transmission electron micrograph of two Ag nanoparticles, showing fine detail well below the diffraction limit of visible light [31].

Several new techniques for exciting or measuring plasmon/electromagnetic interactions have been developed to improve spatial resolution to the point that the electronic structure of the plasmons may be directly resolved, all relying on near-field interactions between probe and target. Near-field measurements of plasmons can take place in a variety of ways, including direct near-field measurements of far-field optically-excited plasmonic fields with fine metal probes [32] or the use of electrons to excite plasmons instead of light [8, 11], for which initial experiments date to the late 1950s and the original research into surface plasmons in metal nanoparticles [33–35]. The large reduction in wavelength provided by using electrons

instead of photons yields proportionally finer spatial resolution. The interaction is quantitated by measuring the amount of energy lost by the probing electron after interaction with the nanoparticle. This method is known as Electron Energy Loss Spectroscopy, or EELS [11]. EELS is attractive in that the equipment necessary is relatively easy to obtain and operate and experimental setup is relatively straightforward compared to other near-field plasmonic probes [11].

Most modern EEL instruments use made by adding an electron calorimeter that is capable of measuring the kinetic energies of electrons to a precision of $\sim$0.1 eV to the detector in a scanning transmission electron microscope (STEM). The STEM provides a well-collimated source of electrons with known kinetic energies (typically on the order of hundreds of keV $\pm$0.4 eV) that can be focused to a sub-nanometer spot size, courtesy of the magnetic lenses in the STEM and the relativistic electron's ($v \geq 0.5c$, also called a "swift" electron) picometer-scale de Broglie wavelength [36]. A representative TEM image is shown in 1.2, illustrating the degree of spatial resolution possible with such an instrument. Recently, some STEMs have had energy filters placed between the electron source and the target, giving the incident beam an energy uncertainty of $\pm$0.1 eV, dramatically improving the energy resolution of the EEL-STEM [37].

EELS is primarily used to probe plasmons to understand their behavior when illuminated with far-field light, as is most commonly encountered in end-user applications. However, there are a number of differences between excitation by a swift electron and far-field light which must be accounted for in order to understand the interaction with the far-field from

EELS data. Thus, in order to understand the experimental results being produced by EELS, it is necessary to have a strong theoretical understanding of the electron/particle interactions. Theory can provide information hidden to the experimentalist, such as the internal polarization of, or the induced electric field near the target, which can help elucidate the complex interactions that occur in EELS. Chief among these differences is the different geometry of the exciting electric field.

1.3 Theory and simulation

1.3.1 Light scattering and absorption

Light scattering and absorption are processes by which the wave vector, $\mathbf{k}$, of a plane wave may be changed when it encounters a target. Much like acceleration, the change in $\mathbf{k}$ can take the form of either a change in magnitude (in absorption, also often called "absorbance") or direction (in scattering), while the total cross-section is the sum of the two and is known as extinction. For an arbitrary target, the scattering cross-section may be written

$$C_{sca} = \frac{8\pi^3}{3}\frac{|\alpha|^2}{\lambda^4} \tag{1.1}$$

while the absorption cross-section is,

$$C_{sca} = \frac{2\pi}{\lambda}\mathrm{Im}[\alpha] \tag{1.2}$$

where α is the linear polarizability of the target. A great deal of physics is hidden in α, as the target's geometry and composition is encoded within. For the sphere, the polarizability

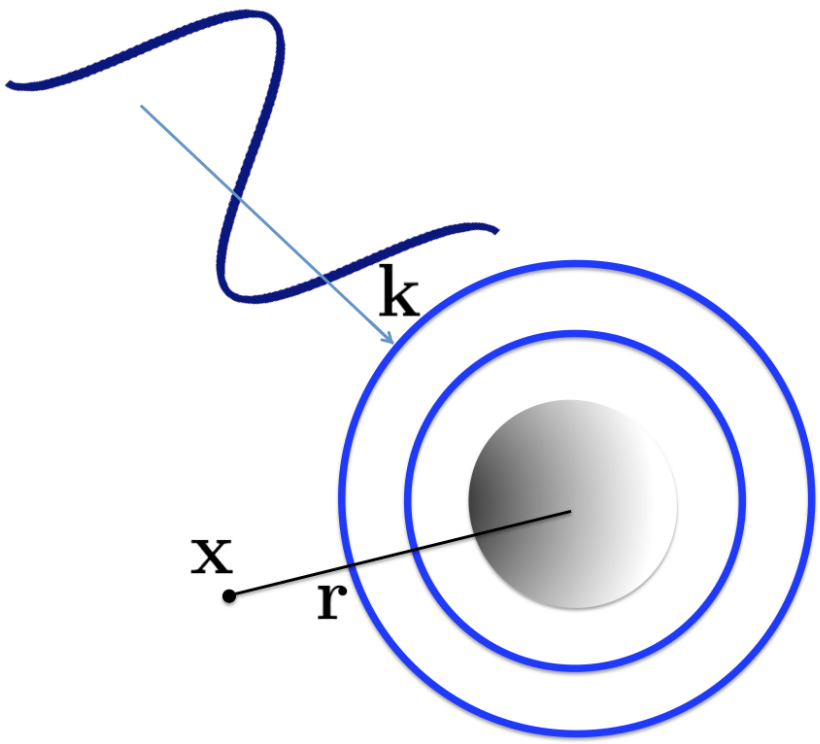

Figure 1.3: A plane wave, $\mathbf{E}_{pw}(\mathbf{x},t) = \mathbf{E}_0 e^{i(\mathbf{k}\cdot\mathbf{x}-\omega t)}$, is incident on a nanoparticle much smaller than the wavelength of light (size exaggerated for clarity), where $\mathbf{E}_0$ is the incident intensity. An outgoing spherical wave is scattered from the particle, per $\mathbf{E}_{sca} = \mathbf{C}_{sca} e^{i(\mathbf{k}\cdot\mathbf{r}-\omega t)}$, where $\mathbf{r}$ is the distance from the target and $\mathbf{C}_{sca}$ is the scattering amplitude. Additional energy from the plane wave may be lost internally through Ohmic heating.

is known from Mie [7] and is written

$$\alpha_j(\omega) = V_j \frac{\epsilon_j(\omega) - 1}{\epsilon_j(\omega) + 2}, \tag{1.3}$$

,

where ϵ_j and V_j are the associated dielectric function and volume, respectively [38]. 1.3 diagrammatically shows the scattering of far field light with wavevector $\mathbf{k}$ and amplitude $\mathbf{E}_0$ ($\mathbf{E}_{pw} = \mathbf{E}_0 e^{i(\mathbf{k}\cdot\mathbf{x}-\omega t)}$) is being scattered off a spherical metal nanoparticle, producing an outgoing spherical wave at point $\mathbf{x}$ a distance of $\mathbf{r}$ from the particle with scattering

amplitude $\mathbf{C}_{sca}$ ($\mathbf{E}_{sca} = \mathbf{C}_{sca} e^{i(\mathbf{k}\cdot\mathbf{r}-\omega t)}$). Analytical expressions for the polarizability of other simple geometries exist, though the spherical result is perhaps the best known, and will be useful in the coming sections on numerical methods.

1.3.2 The discrete-dipole approximation

When plane wave light encounters a simple target, such as a sphere, the electromagnetic response can be well-described analytically. However, light scattering off of arbitrary targets presents a non-trivial challenge to the theoretician. Due to the necessity of finding such solutions, there exist a wide variety of algorithms for numerically solving Maxwell's equations on arbitrary geometries, including finite difference time domain methods [39], boundary element methods [40], and pseudospectral methods [41], among many others. The method of coupled dipoles is particularly attractive to us, as it does not require the discretization of any homogenous background media around the target and the incident electric field is easily parametrized for many excitation sources.

The method of coupled dipoles (also known as the discrete-dipole approximation, or "DDA"), was first suggested by DeVoe in 1964 [42], but it was Purcell and Pennypacker in 1973 [43] who added the effects of retardation, bringing the coupled dipole approximation to the form that we use today. Several implementations of the DDA followed in the ensuing decades [44–46]. The DDA combines linear response theory and dipolar radiation theory to model the electromagnetic properties of an arbitrary target that is discretized into a finite number of dipoles, each with an associated dielectric function. In Gaussian units, the polarizability

of the j^{th} dipole, α_j, is known from the Clausius-Mossotti relationship given in 1.3. The polarization electric field generated by each dipole, $\mathbf{P}_j$, is then known from linear response theory:

$$\mathbf{P}_j = \alpha_j \mathbf{E}_j. \tag{1.4}$$

For multiple dipoles, the electric field $\mathbf{E}_j$ is not trivial, as it includes contributions from both the prescribed incident field and from the polarizations of the other dipoles. The electric field at point j from the other dipoles is given by the dipole relay tensor:

$$\mathbf{E}(\mathbf{x}_l, \omega) = \sum_{j \neq l} \frac{e^{ikr_{jl}}}{r_{jl}} \Big[k^2 (|\hat{\mathbf{r}}_{jl}|^2 - \mathbf{1}_3) + \frac{ikr_{jl} - 1}{r_{jl}^2} (3|\hat{\mathbf{r}}_{jl}|^2 - \mathbf{1}_3) \Big] \mathbf{P}_j = \mathbf{A}_{lj} \mathbf{P}_j \tag{1.5}$$

in which $\hat{\mathbf{r}}_{jl}$ is a normal vector pointing from the j^{th} to the l^{th} dipole, r_{jl} is the interdipole distance, k is the wavenumber at the frequency of incident light, and $\mathbf{1_3}$ is a 3×3 identity matrix [47, 48]. The electric field at the point j is simply the sum of $\sum_l \mathbf{E}(\mathbf{x}_l, \omega)$ and the incident electric field. Thus, the elements of the linear matrix, $\mathbf{A}_{jl}$ are 3×3 matrices given by eqn. 1.5 on the off-diagonals and

$$\mathbf{A}_{jj} = \boldsymbol{\alpha}_j^{-1} \tag{1.6}$$

on the diagonal, where $\boldsymbol{\alpha}$ is the full vector polarizability of the target. Then, beginning with

an initial guess for the polarizations, the linear equation

$$\sum_{j=1}^{N} \mathbf{A}_{lj}\mathbf{P}_j = \mathbf{E}_{inc,l}, \tag{1.7}$$

may be brought to self-consistency to find the polarization of each dipole, $\mathbf{P}_j$. Once the polarizations are known, properties such as the near and far electric fields, the relative scattering, absorbance, and total extinction may be derived.

The only approximation made in DDA, beyond those implicit in linear response theory and dipole radiation theory, is in the discretization of the continuous target into a finite number of dipoles, which implies that DDA is very accurate so long as these dipoles are much smaller than any physical feature of target or of the incident electric field [47]. As DDA operates without energy loss to the incident field, the electron is treated adiabatically in this treatment. In experiment, the kinetic energy of the probing electrons is on the order of 10^5 eV, while the energy of the optical plasmons are on the order of 1 eV, which implies that the adiabatic approximation is very accurate [11].

1.3.3 Simulating EELS with the DDA

In electron energy-loss spectroscopy, a target is probed using high-energy electrons ($E > 100$ keV, $v > 0.5c$), which are dilute enough that each interaction may be treated as occurring independently [11, 49]. As the speed of the electrons is generally greater than $0.5c$, a fully relativistic treatment of the electric field is necessary. The electron is modeled as travelling

along the the same axis as the wavevector in conventional DDA for consistency. Starting with an expression for a charge moving in a straight line and Fourier transforming it to frequency space, we find an expression for the interrogating electric field that is compatible with frequency-space Maxwell's equation solvers, like the DDA:

$$\mathbf{E}(\mathbf{x},\omega) = \frac{2e\omega}{v^2\gamma} e^{i\omega z/v}\Big[\frac{i}{\gamma}K_0\Big(\frac{\omega R}{v\gamma}\Big)\hat{\mathbf{z}} - K_1\Big(\frac{\omega R}{v\gamma}\Big)\hat{\mathbf{R}}\Big], \tag{1.8}$$

where $\mathbf{x} = (\mathbf{R}, z)$ and $\mathbf{R} = (x, y)$, with $R = |\mathbf{R}|$. K_ν are the modified Bessel functions of the second kind of order ν. Relativistic considerations have been accounted for by inclusion of the standard Lorentz contraction in space, γ, as per

$$\gamma = \frac{1}{\sqrt{1 - \left(\frac{v}{c}\right)^2}}, \tag{1.9}$$

where appropriate [11, 38]. Equation 1.8 may the be substituted for the right hand side of equation 1.7 to simulate EEL experiments. Note that in taking the Fourier transform, no consideration has been given to any momentum transfer to the target. This is the adiabatic or non-recoil approximation, which is accurate so long as the energy lost in the interaction with the target is very small compared to the kinetic energy of the electron ($\hbar q \ll m_e v^2/2$). As expected, the electric field of the swift electron displays radial symmetry orthogonal to the motion of the charge. Parallel to the motion of the charge the electric field is non-zero and varies sinusoidally. This is in direct contrast to plane wave light, wherein the electric field is isotropic about, and only has non-zeros components perpendicular to, the wavevector.

These differences between the *structure* of the exciting electric fields from plane wave and electron beam sources will play a pivotal role in understanding the correlation between the plasmons excited by each source.

Replacing the plane wave electric field used in the standard DDA ($\mathbf{E}_{inc,l}$ in eqn. 1.7) with eqn. 1.8 allows DDA to perform EEL calculations. To that end, we have produced an in-house code where the right hand side of 1.7 was replaced with 1.8, based on the DDSCAT code by Draine, et. al. [47]. In our code, which we call the electron driven DDA or simply the *e*-DDA, the incident plane wave electric field has been replaced with that of an aloof, relativistic electron, which efficiently models the EELS experiment. The implementation of the coupled dipole method known as DDSCAT that we used as the framework for our own *e*-DDA was developed in the 1980s by Draine and coworkers at Princeton for the study of interstellar dust [47]. It was quickly understood that the code could be applied to the study of the interaction between plane wave light and other objects — including nanoparticles — without modification [50]. With modification to the incident field, it is possible to simulate EELS experiments using the DDA. This method of simulation enjoys the maturity and simplicity of the DDSCAT code. This method of simulating EELS was suggested by García de Abajo in early 2010 [11], though it appears only very preliminary work has been done on electron-driven DDA. Geuquet and Henrard modeled the electric field of the electron as a point charge travelling with non-relativistic linear motion in a completely new DDA code and applied the model to several simple nanoparticles [48], but to date all other EELS simulations have used other code, often with even greater simplifications to the incident field [51]. In Draine's DDA code, the incident field is generated by a dedicated subroutine "evale.f90", making substitu-

tion of the new electric field easy. Modified Bessel functions were generated by additional subroutines employing a polynomial approximation sourced from Numerical Recipes [52]. The author's modified version of the code is available free of charge via a GNU license online at `http://faculty.washington.edu/masiello/Masiello_Group_Website/e-DDA.html` and the code necessary to modify DDSCAT to function as the *e*-DDA in its basic form is included in the appendices of this work.

Finally, loss probability per unit energy, $\Gamma(\hbar\omega)$, is found by integrating the rate of doing work by the scattered field of the target back on the electron, *via*

$$dW/dt = \int_V \mathbf{J} \cdot \mathbf{E}_{sca} d^3x \tag{1.10}$$

where $\mathbf{J}(\mathbf{x}, t) = -e\mathbf{v}\delta(\mathbf{x} - \mathbf{v}t)$ and $\mathbf{v}$ is the velocity of the electron. The total loss energy can then be written

$$\Delta E = \int_0^\infty d(\hbar\omega)\, \Gamma(\hbar\omega). \tag{1.11}$$

where $\Gamma(\hbar\omega)$ is the loss probability per unit energy, $\hbar\omega$. We write $\Gamma(\hbar\omega)$ as

$$\Gamma(\hbar\omega) = \frac{1}{\pi\hbar^2}\Sigma_j^N \mathrm{Im}[\mathbf{E}^{inc}(\mathbf{x}_j, \omega) \cdot \mathbf{P}_j(\omega)], \tag{1.12}$$

which can be though of as comparing the work done by the electron in polarizing the tar-

get back on the electron, mediated by the induced electric field. In principle eqn. 1.11 is complete and exactly describes the total energy loss of the electron, though rarely is the dielectric data the target complete from the DC limit to the gamma rays and beyond. Fortunately, our energetic region of interest spans only the optical and near optical, so it is not necessary to calculate ΔE, and $\Gamma(\hbar\omega)$ will provide us with all the information we require.

1.3.4 Cathodoluminescence

A plasmon created by the swift electron can radiate to the far-field if it has a non-zero dipole moment. This process of plasmon-mediated photon emission following an electron excitation is called cathodoluminescence. Cathodoluminescence, or CL, from plasmons was first predicted by Ferrell in 1958 [53], and detected by Steinmann two years later [54] in thin films. The comparative ease with which far-field photons can be counted and their energies quantitated makes CL an attractive method for investigating plasmonic structures with electrons, though care must be taken not to confuse CL with EELS. EELS involves both a near-field excitation and measurement, whereas in CL the excitation occurs in the near-field, but the measurement in the far-field. CL response can be thought of as the convolution of the far-field radiation spectrum and the EEL spectrum, as it is the product of both the dipole transition moment and the loss probability.

We calculate the CL intensity once eqn. 1.7 is brought to self-consistency and the polarizations are known, at which point the scattered electric field at any point $\mathbf{x}$ may be computed using eqn. 1.5. The energy flux radiated by the target is given by Poynting's theorem.

Integrating the outgoing energy over the surface of a sphere centered at the target and over all time will yield the total energy radiated per electron interaction, in Gaussian units as

$$\Delta E = \int dt\, r^2 \int d\Omega\, \hat{\mathbf{r}} \cdot \mathbf{S}(\mathbf{r}, t) = \frac{c}{4\pi} \int dt\, r^2 \int d\Omega\, \hat{\mathbf{r}} \cdot (\mathbf{E}(\mathbf{r}, t) \times \mathbf{B}(\mathbf{r}, t)) \tag{1.13}$$

in vacuum, where $\mathbf{S}$ is the Poynting vector and Ω is the solid angle. If the spherical shell of integration is sufficiently large ($r_{sphere} \gg \frac{2\pi c}{\omega}$), we can write the form of the outward propagating field as the product of a spherical wave multiplied by a vector scattering amplitude:

$$\mathbf{E}^{sca}(\Omega, r) = \mathbf{f}(\Omega)\frac{e^{ikr}}{r}, \tag{1.14}$$

where $k = \omega/c$ in vacuum. Assuming that $\mathbf{E}^{sca}$, $\mathbf{B}^{sca}$, and $\hat{\mathbf{r}}$ are mutually orthogonal and Fourier transforming eqn. 1.14 into frequency space, with the electric field given by eqn. 1.5, we can write the CL intensity per electron, per unit energy:

$$\Delta E(\hbar\omega) = \frac{r^2}{4\pi^2 \hbar k} \int d\Omega |\mathbf{E}^{sca}(\Omega, r)|^2. \tag{1.15}$$

We may then use eqn. 1.15 with far-field calculations from the *e*-DDA to compute cathodoluminescence spectra or cathodoluminescence maps in the same way as with the loss probability. It may also be of interest that the CL response scales as the magnitude of the polarizability, whereas the EEL scales as the imaginary component of the polarizability. Comparing

this knowledge to 1.1 and 1.2, we see that CL and EELS encode the same information about the target as optical scattering and absorbance, respectively [55].

1.3.5 Electron tomography

Tomography, coming from the Greek $\tau\acute{o}\mu o\varsigma$ meaning "slice", is the process by which a three-dimensional model of an object can be built from many two-dimensional images of that object taken at different angles. The mathematical basis for tomography was initially explored by Radon in 1917 [56] and the method was first suggested to produce two-dimensional maps from single-dimensional radio data by Bracewell in 1956 [57]. Tomography was expanded to the third dimension by Cormack seven years later [58] and it has subsequently become a central tool in medicine, engineering, and many other fields [59]. Magnetic resonance imaging (the "MRI"), computed axial tomography ("CAT scans"), and positron emission tomography ("PET scans") are all examples of tomography familiar to the general public due to their ubiquitous nature in modern medicine, though each of these three forms of tomography use a different method to build their constituent two-dimensional images. In principle, any method of generating a two-dimensional image of a target can be used in tomography, so long as the images can be made from multiple different angles.

Electron microscopy is one such method, and the resulting electron tomography allows for fully three dimensional models to be made with the same sub-nanometer resolution afforded by the electron beam. This method is of great interest to the plasmonics community as it allows us to build complete models of real plasmon-supporting structures with a minimal

amount of inference about the third dimension. This takes much of the guesswork out of the electrodynamic modeling of plasmonic structures and helps promote theory from qualitation to full quantitation.

1.4 Electromagnetic hot spots

the capability of plasmons to focus optical-frequency electromagnetic fields into deep sub-diffraction limit volumes is at the central to their function in most applications [11]. For example, single-molecule surface-enhanced Raman scattering (SMSERS) which relies on electric hot spots to amplify the Raman signal while quenching fluorescence to the extent that Raman spectra can be obtained from a single molecule [18, 19]. Electromagnetic hot spots tend to form in the junction between two adjacent nanoparticles when plasmons supported on each particle are arranged in a "bonding" fashion; that is, when the polarizations of each particle are arranged in a head-to-tail manner at the point of nearest approach between the particles. By placing a positive charge at the head of one of the polarizations nearest the negative charge at the tail of the other, the bonding arrangement is stabilized compared to the converse anti-bonding arrangement, and the close proximity of the large positive and negative charges leads to very high electromagnetic fields inside the junction. In this arrangement, the junction can be thought of as a capacitor, with a large amount of energy from around the nanoparticle stored in the very strong field in the junction [60, 61].

Despite the importance of the hot spot in most practical applications of plasmons and the utility of EELS in investigating the plasmons on their own length scales, it was the prevailing

understanding in the field that EELS is "completely blind to the hot spot" [62]. This belief was based on the (correct) assertion that the radial symmetry of the electron's electric field would not excite a bonding arrangement of the plasmons in a multi-particle system when the beam is at the location of the hot spot. However, in contrast to the prevailing belief, the work in this thesis will show that it is still possible to infer the existence of a hot spot with EELS [60].

1.5 Magnetoplasmonics

Circular aggregates of nanoparticles support plasmonic eigenmodes in which all the polarizations are arranged head to tail, forming a loop. These loop eigenmodes support electric hot spots in all the junctions between the particle *and* a magnetic hot spot in the center of the ring of particles, as the loop of polarizations forms an oscillating circular current [63–65]. This system, which is effectively an LC-circuit [66], is highly significant because the magnetic field exists at the same frequency as the plasmons that collude to create it, that is, in or near the optical. No materials found in nature have are known to have a significant magnetic response at optical frequencies, and as such, magnetic hot spot supporting plasmonic structures have properties "beyond" normal materials and belong to a category of materials that has come to be known as the "metamaterials".

Most metamaterials are still in their infancy, and magnetoptical materials are no exception. Prior work has established a solid introduction to magnetoplasmonics, but no detailed studies of complex structures of multiple rings existed prior to this work. Much like a single

nanoparticle can support an array of electric modes, so too can multi-ring aggregates support an array of magnetic modes, a fact which had gone unexplored until this year.

1.6 Fano resonances

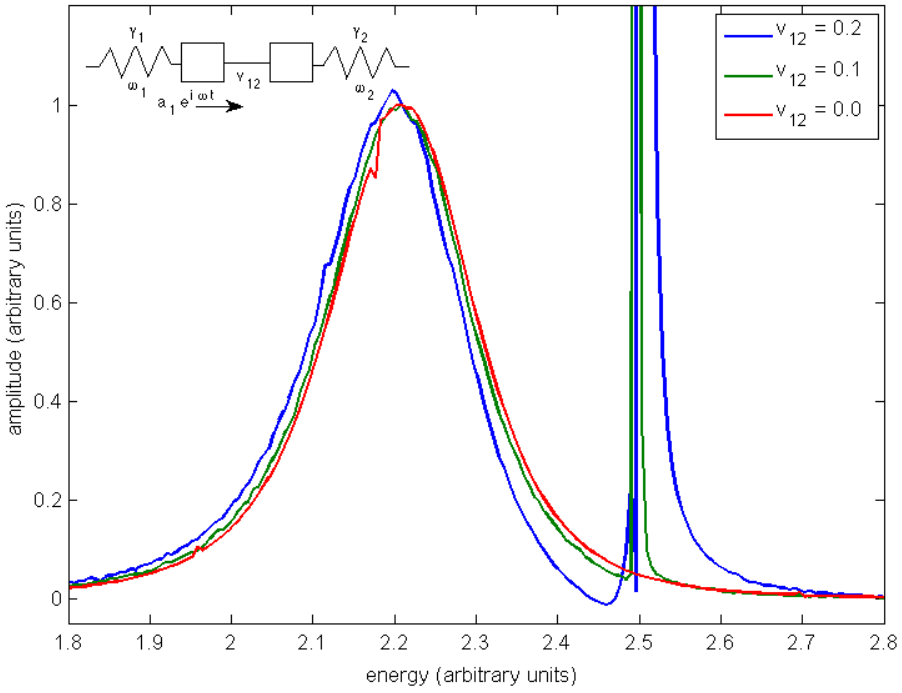

Figure 1.4: Spectra for two coupled, damped oscillators, only one of which is driven, found by solving the damped, driven oscillator equation for a wide range of driving frequencies ω. For this model $\omega_1 = 2.223$, $\omega_2 = 2.5$, $\gamma_1 = 0.32$, $\gamma_2 = 0$, and $a_1 = 1$. The coupling potential v_{12} was varied from 0.0 to 0.2 to show the development of a classical Fano resonance in in the high-energy peak in analogy to bringing two nanoparticles together, one which is optically bright and one which is dark. A schematic of the two oscillators is drawn in the upper left corner.

The coupling of two plasmons can form a Fano resonance, a type of interference in which one of the plasmon modes transfers energy through the electric near-field to another mode either in phase or out of phase. This leads to the creation of a super-radiant mode when

the transfer is in phase and constructive, and a sub-radiant mode when it is out of phase and destructive. Because the phase flip occurs very quickly as the frequency of the incident electric field increases past the resonant frequency of one of the modes, Fano resonances can be extremely narrow. Fano resonances have been described as being "of significant importance particularly in the development of high-sensitivity plasmon-based sensors, where Fano resonances currently underlie some of the world's best" [67]. Fano resonances are a general wave phenomena that can occur anywhere two oscillatory phenomena can couple to one another. First described by Ugo Fano in 1961 in the neutron scattering spectra of helium [68], Fano resonances have since been found in everything from classical masses on springs [69] to excited electrons in high temperature superconductors [70].

The Fano resonance can be modelled by treating the two interfering plasmons as coupled harmonic oscillators in which only one is driven. This is known as the Alzar model [69], and can be instructive in designing a plasmonic Fano resonance. The results of a numerical solution of the Alzar model is shown in 1.4 as an example of a Fano resonance, with comparison to the uncoupled oscillator (red), and two coupled oscillators of increasing coupling strength (green and blue, respectively). The spectrally-sharp asymmetric feature between 2.4 and 2.6 energy units is the Fano resonance. Transparency can be observed in the reduced response relative to the uncoupled oscillator below 2.48 energy units, while dramatically increased response is seen in above 2.48 energy units. The asymmetric line shape that is characteristic, though not diagnostic, of a Fano resonance.

Because a Fano resonance requires one mode to be (relatively) undriven by the driving field, it was thought that EELS would not be able to resolve a Fano resonance, as the electron

beam can access all plasmon modes at once [51, 71]. However, a Fano resonance can occur when one mode is simply less driven by the incident field than another, allowing for EELS to show the phenomenon for a beam location that favors one mode over another. If one of the modes is also optically dark, the Fano resonance can appear enhanced in the CL spectrum as well. This is shown for the first time in this work [72].

1.7 Outline

1.7.1 Publications

The author's peer-reviewed work in the Masiello group spans six published papers, one in review, and four more in preparation, for a total of eleven publications, with two additional papers published prior to the author's graduate school work, not enumerated here. Nicholas W. Bigelow's publications in the Masiello group are as follows:

1. ***Characterization of the Electron- and Photon-Driven Plasmonic Excitations of Metal Nanorods***

   N. W. Bigelow, A. Vaschillo, V. Iberi, J. P. Camden, and D. J. Masiello.

   ACS Nano **6**, 7497 (2012)

2. ***Signatures of Fano Interferences in the Electron Energy Loss Spectroscopy and Cathodoluminescence of Symmetry-Broken Nanorod Dimers***

   N. W. Bigelow, A. Vaschillo, J. P. Camden, and D. J. Masiello.

   ACS Nano **7**, 4511 (2013)

3. ***Single-Molecule Surface-Enhanced Raman Scattering: Can STEM/EELS Image Electromagnetic Hot Spots?***

   N. Mirsaleh-Kohan[#], V. Iberi[#], P. D. Simmons Jr., N. W. Bigelow, A. Vaschillo, M. M. Rowland, M. D. Best, S. J. Pennycook, D. J. Masiello, B. S. Guiton, and J. P. Camden.

   Journal of Physical Chemistry Letters **3**, 2303 (2012)

4. *Thermal Signatures of Plasmonic Fano Interferences: Toward the Achievement of Nanolocalized Temperature Manipulation*

   C. L. Baldwin, N. W. Bigelow, and D. J. Masiello.

   J. Phys. Chem. Lett. **5**, 1347 (2014)

5. ***Resonance-Rayleigh Scattering and Electron Energy Loss Spectroscopy of Silver Nanocubes***

   V. Iberi, N. W. Bigelow, N. Mirsaleh-Kohan, S. Griffin, P. D. Simmons, B. S. Guiton, D. J. Masiello, and J. P. Camden.

   Journal of Physical Chemistry C **118**, 10254 (2014)

6. ***A Combined Tight-Binding and Numerical Electrodynamics Understanding of the STEM/EELS Magneto-Optical Responses of Aromatic Plasmon-***

Supporting Metal Oligomers

C. Cherqui[#], N. W. Bigelow[#], A. Vaschillo, H. Goldwyn, and D. J. Masiello.

ACS Photonics **1**, 1013 (2014)

7. *Nanoscopic imaging of energy transfer from single plasmonic particles to semiconductor substrates via 3D STEM/EELS*

   G. Li, C. Cherqui, N. W. Bigelow, G. Duscher, P. J. Straney, J. E. Millstone, D. J. Masiello, and J. P. Camden.

   This work is currently under review.

8. ***Electron Tomography and its Importance to Quantitative Modeling of Experiment***

   N. W. Bigelow, T. L. Sooter, K. Munechika, D. S. Ginger, and D. J. Masiello.

   This work is currently in progress.

9. *EEL spectra on individual Ag nanospheres spanning 10 - 200 nm in diameter*

   C. Cherqui, G. Li, N. W. Bigelow, J. P. Camden, and D. J. Masiello.

   This work is currently in progress.

10. *Experimental study of individual alloy nanospheres of varying concentration*

    G. Li, C. Cherqui, N. W. Bigelow, N. Thakkar, D. J. Masiello, and J. P. Camden.

    This work is currently in progress.

11. *Theoretical study of plasmonic energy transfer at a metal nanoparticle-semiconductor substrate interface*

    G. Li, C. Cherqui, N. W. Bigelow, D. J. Masiello, and J. P. Camden.

    This work is currently in progress.

[#]These authors contributed equally to this work.

Papers that Nicholas W. Bigelow is first author or first theory author have their titles bolded in the list above. This dissertation is composed of five of the six published papers in which the author is either first author, or first theory author and has direct ownership of a major part of the work. Chapters 2 through 6 are works already published and chapter 7 is work currently in preparation.

1.7.2 The form of this dissertation

The work contained in this thesis is broken into three main parts: first, the capability of EELS to resolve electromagnetic hot spots in contrast to the published literature is predicted in chapter 2, then experimentally verified in chapter 3. Chapter 2 develops the concept of hot spot inference by first comparing the plasmon modes excited by an electron beam and plane wave light, where it is found that modes at the same energy are structurally identical regardless of excitation source. Once the interchangeability of the exciting electric field is established, the capacity for an electron beam to generate an electric hot spot in a hot spot

spatially removed from the electron beam is shown, and in this way the problem of the electron beam's symmetry is avoided. Armed with this knowledge, this work then *predicts* that the existence of an electric hot spot can be inferred from EEL data when there is a peak in the loss probability at the distal ends of the particles, and a node in the probability in the junction. This is in direct contrast to the prevailing opinion prior to the publication of this work.

Chapter 3 shows the experimental verification of the ability to infer the existence of an electric hot spot with EEL data, as predicted in chapter 2. This chapter is an experimentally-led paper in which the author provided all theoretical and computational results. The existence of an electric hot spot is determined by finding an aggregate of nanoparticles that is SMSERS-active, then characterizing that aggregate with electron microscopy and EELS. Electron micrographs of the aggregate are used to construct a computational model of the system, and EEL and scattered electric near-field data is computed and compared to experiment. As predicted, at the energy at which an electromagnetic hot spot is known to exist around the structure, the EEL data shows maximal loss probability far from the junction, and a node in the loss probability in the junction, confirming EEL's ability to detect and characterize electric hot spots.

Chapter 4 extends the work on electric hot spots to magnetic hot spots in ring structures. The work presented here is the most complete examination of magnetic hot spots to date, and structures that support multiple different ferromagnetic and antiferromagnetic hot spots are examined. The structure and energetics of the magnetic hot spots is explored in depth,

and the location of the electron beam for the excitation of all magnetic modes in the studied structures is presented. Several theoretical models of magnetoplasmonic phenomena, including the LC-circuit model, the Hückel model, the coupled-dipole model and full computational electrodynamics, are explored as well.

Chapter 5 predicts the ability to generate and detect Fano resonances with the electron beam, which had previously been deemed impossible, or at least very challenging [51, 71]. A bi-metallic system of two collinear metal rods, whose lengths have been chosen such that the dipolar (optically bright) plasmon of the small rod overlaps energetically with the quadrupolar (optically dark) plasmon on the larger rod. The Fano resonance that occurs from the hybridization of these two modes is readily evident in optical scattering, as expected, and also in the EEL experiment when the electron beam is placed near the end of the smaller rod. A second energy-reversed Fano resonance is also found when the electron beam is placed at a distance below the junction. The latter Fano resonance is not found in the optical experiment and is of a type entirely new to science. Its "birth" is shown in detail as the electron beam is raster-scanned away from the junction, "unpinning" the polarizations and allowing for a complete phase flip in the rods. This is the first time an EEL Fano resonance has been predicted in the literature.

Chapter 6 is the first experimental verification of a Fano resonance in an EELS experiment. Like chapter 3, this chapter is an experimentally-led paper in which the author provided all theoretical and computational results. A plasmon-supporting nanocube is placed on a substrate and its optical and EEL spectra are measured. The cube on a substrate is a sys-

tem that had previously been show to support a Fano resonance [73]. Through comparison of experiment and theory, this work verifies the existence of a Fano resonance in the EEL experiment, and in the process develops a richer language with which to understand the phase transitions endemic to Fano resonances.

The last chapter prior to the conclusion compares and contrasts the plasmonic properties of two models of the same real multi-particle target: one generated in the standard way from a single electron micrograph looking down from above the target and the other a fully three-dimensional tomographic reconstruction of the target. Some properties, such as the far-field plane wave spectrum are shown to be very similar between the two models, but properties that are highly dependant on the fine structure of the target, such as the hot spot volume, are shown to differ considerably between the guess and tomographic reconstructions. The utility of tomography for future work on plasmonics thus shown, this dissertation concludes.

Chapter 2

Characterization of the Electron- and Photon-Driven Plasmonic Excitations of Metal Nanorods

This work has previously been published in the following article:

N. W. Bigelow, A. Vaschillo, V. Iberi, J. P. Camden, and D. J. Masiello.

ACS Nano **6**, 7497 (2012)

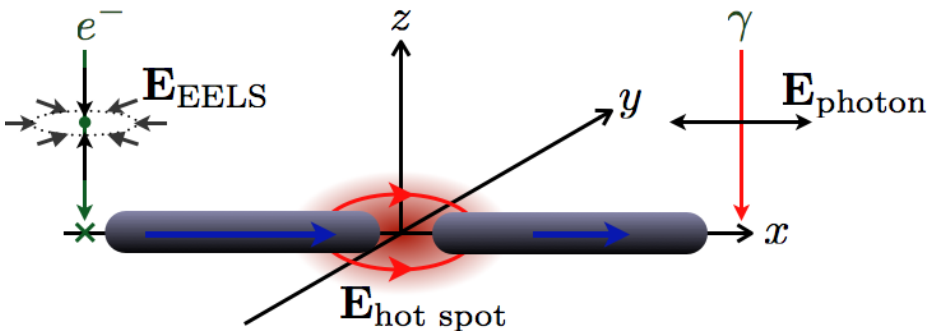

Figure 2.1: Abstract figure.

2.1 Abstract

A computational analysis of the electron- and photon-driven surface-plasmon resonances of monomer and dimer metal nanorods is presented to elucidate the differences and similarities between the two excitation mechanisms in a system with well understood optical properties. By correlating the nanostructure's simulated electron energy loss spectrum and loss-probability maps with its induced polarization and scattered electric field we discern how certain plasmon modes are selectively excited and how they funnel energy from the excitation source into the near- and far-field. Using a fully retarded electron-scattering theory capable of describing arbitrary three-dimensional nanoparticle geometries, aggregation schemes, and material compositions, we find that electron energy-loss spectroscopy (EELS) is able to *indirectly* probe the same electromagnetic hot spots that are generated by an optical excitation source. Comparison with recent experiment is made to verify our findings.

2.2 Introduction

The mechanisms by which a swift ion can deposit energy into metallic films, spawning both individual and collective electronic excitations, have been well established [11, 33, 74–76]. The experimental techniques developed to probe these phenomena and their related theoretical underpinnings are now seeing a renaissance in the fields of nanophotonics and nanoplasmonics. Recent experimental interrogation of nanoscopic metal triangular prisms [77–79], spheres [80, 81], rods [82–84], cubes [85], and decahedra [86] with swift electrons has exposed a variety of new information that is not resolvable with standard optical techniques alone. The observation of optically dark plasmonic modes [81, 84] evidences the differing selection rules between electron- and photon-excitation sources. Also, the direct spatial mapping of plasmon resonances and, with correlated optical techniques, their associated evanescent near-field and electromagnetic far-field demonstrates the unique resolving power of the electron [87, 88]. Still, questions remain that call for the implementation of theories capable of describing the electron-driven excitation of plasmonic nanoparticle assemblies of arbitrary geometry, aggregation scheme, and material composition. Examples include the following: 1) Is there a difference between the plasmons generated at the same excitation energy but by an electron rather than a photon source? 2) What is the difference between their associated evanescent near-fields? 3) How similar are their far-fields? 4) What is the signature of electromagnetic hot spots in EELS and what is their relationship to optical excitation?

In the following, we address these questions within the context of monomer and dimer silver nanorods using an electron-scattering theory based upon a modification [11] of the discrete-

dipole approximation (DDA) [43, 47]. An interesting result of our work is that EELS is capable of *indirectly* probing electromagnetic hot spots, such as those responsible for surface-enhanced Raman scattering (SERS). Our argument, which relies upon correlating electron and photon spectroscopies, is that the spatial locations of high electron energy loss and intense photonic near-fields need not be colocated; yet they are related in a simple way by noticing that the near-field generated by an electron probe, when positioned properly, is directionally identical to that set up by an optical source. Recent experiment is consistent with this prediction [89].

The motion of a swift ion generates an electric field whose structure and dynamics are governed by the equation of motion [38]

$$\nabla \times \nabla \times \mathbf{E} + \epsilon\mu\ddot{\mathbf{E}}/c^2 = -4\pi\mu\dot{\mathbf{J}}/c. \tag{2.1}$$

Accordingly, an electron of charge $-e$ moving uniformly along the trajectory $\mathbf{r}(t) = \mathbf{v}t$ imposes the field

$$\mathbf{E}_{\mathrm{EELS}}(\mathbf{x},\omega) = \frac{2e\omega}{v^2\epsilon\gamma}e^{i\omega z/v}\Big[\frac{i}{\gamma}\mathrm{K}_0\Big(\frac{\omega b}{v\gamma}\Big)\hat{\mathbf{v}} - \mathrm{K}_1\Big(\frac{\omega b}{v\gamma}\Big)\hat{\mathbf{b}}\Big] \tag{2.2}$$

upon a point $\mathbf{x}$ located a distance $|\mathbf{x}| = \sqrt{|\mathbf{b}|^2 + z^2}$ away from its path. The structure of this field is markedly different from that of a plane wave in that it has polarization components perpendicular to ($\hat{\mathbf{b}} \perp \hat{\mathbf{v}}$) *and* along the direction of propagation ($\hat{\mathbf{v}} \parallel \hat{\mathbf{e}}_z$). Both

components decay radially as the modified Bessel functions K_0 and K_1, and are not spatially isotropic for $v < c$. Rather the electric field of the electron is spatially localized and spectrally broadband, exactly the opposite of the spatially isotropic and monochromatic plane wave. Experiments like EELS exploit these unique electromagnetic properties by using electrons with keV kinetic energies to probe the electronic structure of matter with sub-Ångstrom spatial resolution [90]. Such experiments [77–88] and their correlation with optical spectroscopies now represent the next generation of light-matter interaction in nanoplasmonics and nanophotonics offering unprecedented spatial, spectral, and temporal resolution.

Metal nanorods with high aspect ratios and their aggregates serve as a good test bed for our numerical approach as they support a clear progression of longitudinal multipolar plasmon resonances that hybridize in a straightforward manner upon aggregation [91]. The symmetry of the rod establishes electronic density disturbances that are eigenfunctions of parity, i.e., $\Pi\Omega_{g,u}(\mathbf{x}) = \Omega_{g,u}(-\mathbf{x}) = \pm\Omega_{g,u}(\mathbf{x})$. One would expect that only the transitions $\langle\Omega_u|\mathbf{x}|\Psi_0\rangle$ from the many-electron (symmetric) ground state Ψ_0 of the metal to transient, odd-parity plasmons Ω_u will be dipole-allowed, whereas those transitions to even-parity plasmons Ω_g, which have no net dipole moment, will be forbidden. This is the case for a plane wave excitation source in the so-called long-wavelength or electric-dipole interaction approximation. However, this approximation is inappropriate for electron-driven transitions because the variation of the electron's associated electric field over the target is significant and, further, carries a wavelength that is reduced by a factor of v/c in comparison to a photon of the same energy. Because of this, the electron source is able to probe transitions that are optically inaccessible [81, 84].

Our numerical approach, which we call electron-driven DDA (e-DDA), imposes the exciting electric field $\mathbf{E}_{\mathrm{EELS}}$ of a swift electron (2.2) instead of a plane wave upon each point $\mathbf{x}_j$ of the target [11]. Through electric-dipole radiation each dipole couples to all others in the same manner as in the DDA, yielding a similar

$$\sum_{k=1}^{N}[\boldsymbol{\alpha}_{jk}^{-1}(\omega) - (1-\delta_{jk})\boldsymbol{\Lambda}_{jk}] \cdot \mathbf{P}_k(\omega) = \mathbf{E}_{\mathrm{EELS}}(\mathbf{x}_j, \omega) \tag{2.3}$$

problem for every spatial position $\mathbf{b}$ of the electron beam with respect to the target, the latter described by its bulk dielectric function $\epsilon(\omega)$ through the linear polarizability $\boldsymbol{\alpha}_{jk}(\omega) \equiv \boldsymbol{\alpha}_j(\epsilon(\omega))\delta_{jk}$ of each point j. Iterative solution of these e-DDA equations from the initial guess $\mathbf{P}_j = \mathbf{0}_j$ at each ω determines the polarization induced in the target by the loss of energy $\hbar\omega$ from the electron beam.

The probability per unit energy $P_{\mathbf{b}}$ for the incident electron to lose kinetic energy is determined from the rate of doing work by the electric field of the electron back upon itself, i.e., $dW/dt = \int_V \mathbf{J} \cdot \mathbf{E}_{\mathrm{EELS}}\, d^3x$. Assuming that the electron undergoes no recoil as it moves along its trajectory, its current density becomes $\mathbf{J}(\mathbf{x}, t) = -e\mathbf{v}\delta(\mathbf{x} - \mathbf{v}t)$, which leads to the following loss probability [11],

$$P_{\mathbf{b}}(\hbar\omega) = \frac{1}{\pi\hbar^2}\mathrm{Im}\sum_{j,k=1}^{N} \mathbf{E}^{*}_{\mathrm{EELS}}(\mathbf{x}_j, \omega) \cdot [\boldsymbol{\alpha}^{-1}(\omega) - (1-\delta)\boldsymbol{\Lambda}]^{-1}_{jk} \cdot \mathbf{E}_{\mathrm{EELS}}(\mathbf{x}_k, \omega). \tag{2.4}$$

Computation of $P_{\mathbf{b}}$ allows us to determine the energy loss spectrum of each spatial point $\mathbf{b}$ in the plane of the target in direct analogy to experiments where the scanning transmission electron microscope (STEM) is rastered over the target and the energy loss spectrum of the electron is collected at each point. We emphasize that this e-DDA allows us to compute the fully retarded electron-driven plasmonic responses of a three-dimensional nanoparticle assembly of arbitrary geometry, aggregation scheme, and material composition. This differs from other recent theoretical approaches to EELS that work within the quasi-static approximation to study idealized, flat, disk-shaped nanoparticles [62], or that antisymmetrize the polarization of the plane wave to mimic the transverse polarization of the electron's electric field [81]. The e-DDA is, however, similar to the coupled-dipole/DDA approach implemented by Geuquet and Henrard [48], with the main difference being that we work within the existing framework of Draine's DDSCAT code [47] to numerically implement the working equations in parallel. The flexibility and efficiency of the existing algorithm, which relies upon a bi-conjugate gradient method for the iterative solution of 2.3, allow us to easily extract the plasmonic polarization and scattered electromagnetic field at any point in space induced by the loss of energy from a passing swift electron. This e-DDA approach should compare similarly to other rigorous and efficient theoretical/numerical approaches to EELS such as the boundary-element [92] and T-matrix [93] methods. Both map the full three-dimensional electromagnetic scattering problem onto a two-dimensional boundary-value problem defined at the interface between dielectric media. Also, an implementation of EELS in COMSOL has recently been reported [94]; however, due to the brevity of its description it is difficult to compare to the e-DDA.

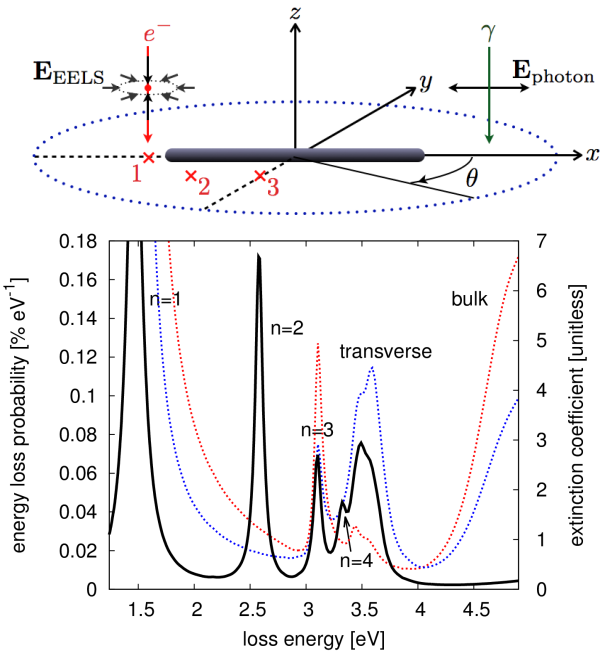

Figure 2.2: Energy loss spectrum (black) of a 202 nm × 40 nm silver nanorod on an amorphous SiN_x substrate. The rod is excited by a 0.1 MeV electron beam positioned 1 nm away from the rod's tip as indicated by position 1 in the upper panel. The beam is propagating normal to the plane of the substrate (not shown). For comparison, the optical extinction spectrum of the rod is displayed in the background. The red (blue) curve corresponds to light propagating normal to the substrate and polarized along ($\theta = 45°$ with respect to) the rod axis. The four lowest energy resonances correspond to the lowest lying longitudinal plasmon modes of which the first ($n = 1$) and third ($n = 3$) are optically bright and the second ($n = 2$) and fourth ($n = 4$) are optically dark. The latter two are absent in the optical extinction spectrum.

2.3 Results and discussion

2.3.1 EELS spectra and maps.

2.2 presents the e-DDA-based EELS spectrum (black) of a 202 nm × 40 nm silver nanorod supported upon an amorphous SiN_x substrate. The propagation direction of the 0.1 MeV electron beam is oriented normal to the long axis of the rod (also normal to the substrate, which is not shown) as shown in the upper panel of the figure. For comparison, the computed optical extinction spectra for light propagating normal to the substrate and polarized both

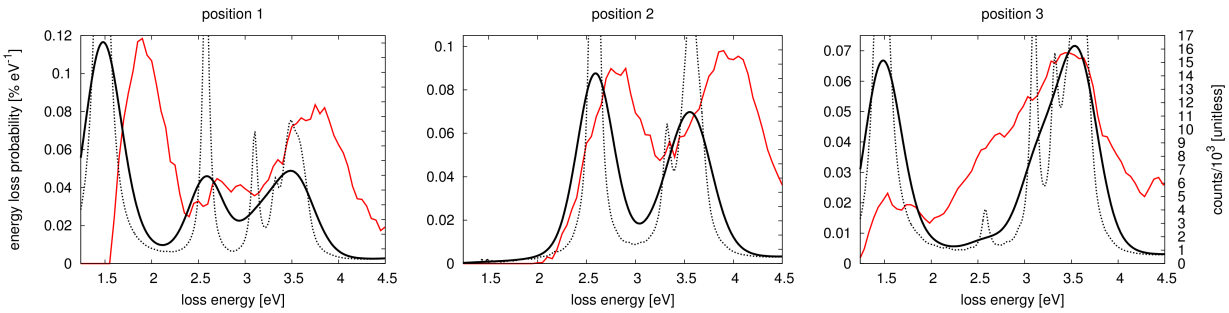

Figure 2.3: Experimental (red, right vertical axis) and theoretical (black, left vertical axis) EEL spectra corresponding to three positions of the electron beam as shown in the upper panel of 2.2. To mimic the instrumental resolution, each point in the computed spectra (dotted black) is convoluted with a Gaussian function whose full width at half-maximum is 0.4 eV (solid black). The height of each Gaussian at each spectral point is chosen so that its area is equal to the corresponding loss probability at that point.

along (red) and $\theta = 45°$ (blue) from the rod axis are also displayed across the same spectral range using the DDA. A progression of collective electronic resonances arise in the low loss energy part of the spectrum corresponding to the excitation of multipolar surface plasmons that are spatially delocalized along the longitudinal axis of the rod. Interestingly, while the EELS spectrum shows both odd and even order plasmonic resonances, the optical resonance features skip all even orders because their wave functions exhibit no net dipole moment and are, therefore, optically dark. Indeed, the consequences of plasmon symmetry are immediately evident in comparing the electronic and optical spectra of the nanorod. At higher loss energies near 3.5 eV, surface-plasmon resonances that oscillate transverse to the rod's long axis are excited by the $\hat{\mathbf{v}}$-dependence of the polarization (2.2), before the excitation of the bulk plasmon at even higher energies.

A set of silver nanorods similar to this was recently characterized under STEM/EELS by

Guiton, Camden, and co-workers [82]. Their experiment correlated, for the first time, EELS plasmon maps with optical scattering from the exact same nanoparticles. 2.3 displays the experimental EELS spectra (red) measured at three different spatial points surrounding the rod as shown in the upper panel of 2.2. EEL spectra computed at the same three points are displayed in the background as the dotted black curves. For comparison between the two spectra, each point is convolved with a Gaussian function having a full width at half-maximum of 0.4 eV (blue), the area of which is equal to the computed loss probability at that point. The width of 0.4 eV is not an adjustable parameter, but rather is dictated by the resolution of the STEM/EELS instrument. No shifting is performed on either the computed or observed spectra, yet their agreement is quite good. Some reasons for the differences between the spectra, particularly at low loss energies, may be due to the fact that the zero-loss peak must be subtracted from the experimental EEL spectrum. In general, this is a difficult task even with good signal-to-noise ratios. Small imperfections in the shape of the rod and/or substrate can alter the rod's local dielectric function, thereby affecting the EELS spectrum. This, in addition to the distance/angle between rod and substrate, is challenging to quantify experimentally and, therefore, was not accounted for in the computations. Also, it is not unreasonable to speculate that the electron beam is damaging the target and/or the substrate, providing a further spatial-dependent modification of the dielectric functions of each [81].

At the energy of the two lowest lying longitudinal plasmon resonances of the rod monomer (2.2) and dimer (not shown) we compute a spatial mapping of the loss probability $P_{\mathbf{b}}$. The dimer is oriented along the x axis and is composed of co-linear 111 nm $\times$ 11 nm monomer

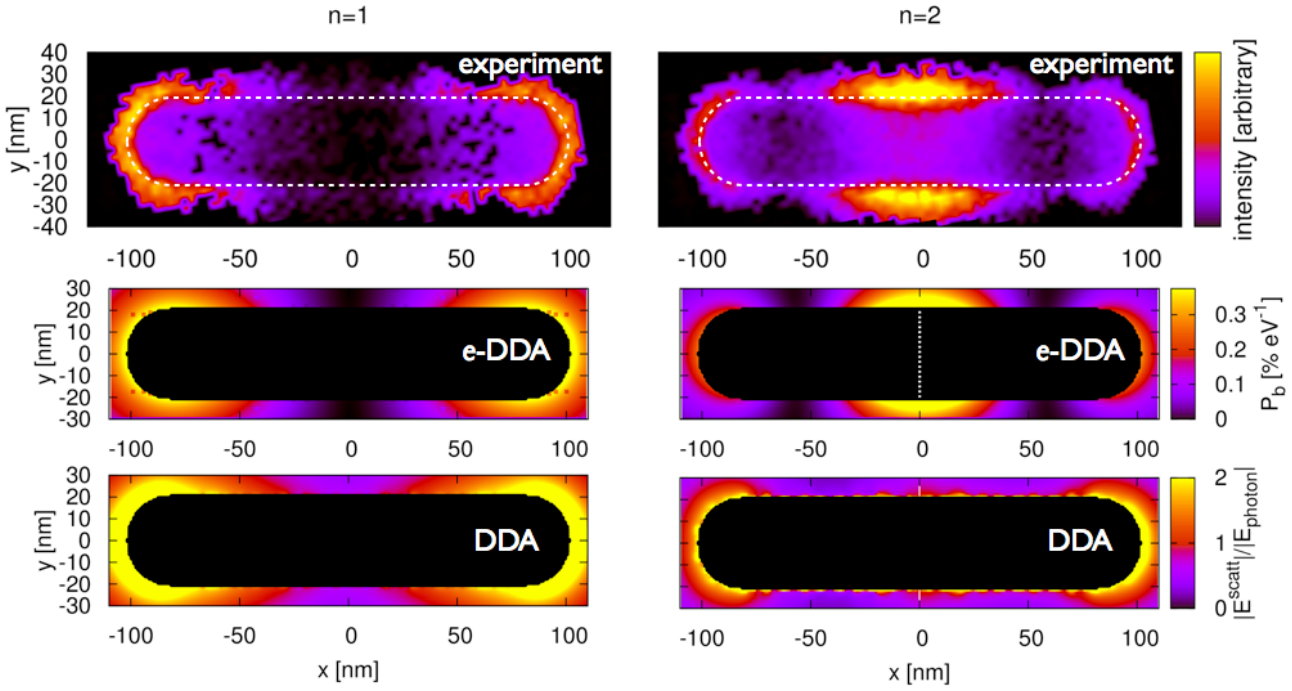

Figure 2.4: Loss-probability maps of the two lowest lying longitudinal plasmon modes of a silver nanorod supported on an amorphous SiN_x substrate. $n = 1$ (1.50 eV) and $n = 2$ (2.61 eV) correspond to the first bright and dark plasmon modes of the monomer. The upper two panels display the experimentally measured loss-probability maps, adapted from Ref. [82], while the middle two panels display the same observable computed *via* the *e*-DDA. Each map indicates where in space the incident electron is likely to deposit the fraction $\hbar\omega$ of its initial 0.1 MeV kinetic energy into a multipolar plasmon mode. The white dotted line in the middle right panel indicates the spatial location of the node of the first dark plasmon mode of the rod monomer. The lower two panels display the magnitudes of the corresponding electric fields scattered from the rod after excitation by a plane wave, computed *via* the DDA; these near-field magnitudes are taken in ratio to the magnitude of the incident plane wave, $\mathbf{E}_{\text{photon}}$. For the $n = 1$ mode the incident field's direction of propagation (electric polarization) is normal (parallel) to the long axis of the rod. While for the $n = 2$ mode, the incident field propagation and polarization directions lie in the plane of the long axis of the rod and its normal, but are tilted by $\pm 45°$ with respect to the normal. This arrangement allows for light to couple into a mode of the rod that is dark under normal incidence. In order to symmetrize the $n = 2$ scattered electric field, we average together both $\pm 45°$-polarizations [82]. It is clear that the loss-probability maps (upper four panels) and the photonic local density of states [95], which is related to the scattered electric field magnitude [96] (bottom two panels), are not simply related to each other in this case [62, 97].

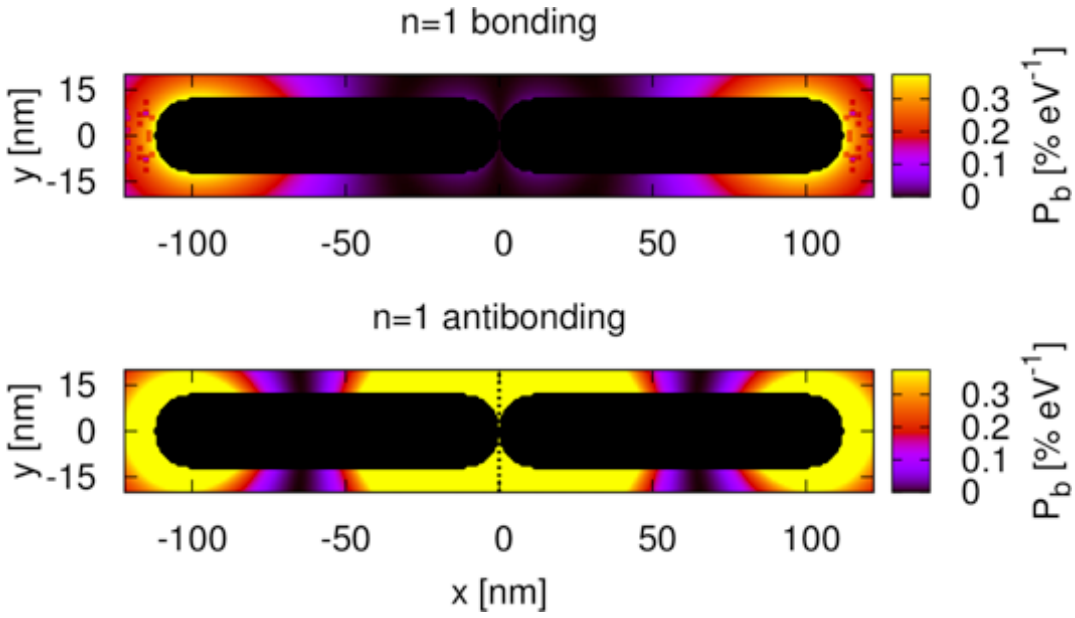

Figure 2.5: Loss-probability maps of the two lowest lying longitudinal ($n = 1$ bonding and antibonding) plasmon modes of a silver nanorod dimer supported on an amorphous SiN_x substrate. The rods are arranged to have a 1 nm gap in the junction between monomers. Each map indicates where in space the incident electron is likely to deposit the fraction $\hbar\omega$ of its initial 0.1 MeV kinetic energy into a multipolar plasmon mode. The black dotted line in the lower panel indicates the spatial location of the node of the first antibonding plasmon mode of the rod dimer. For the bonding mode, the loss-probability in the junction is nearly zero, which has led to the belief that EELS is blind to electromagnetic hot spots [62].

subunits separated by a 1 nm gap. For both monomer and dimer, $P_{\mathbf{b}}$ is projected onto the plane that bisects the long axis of the rod and that is perpendicular to the direction of propagation of the electron beam. This requires solving 2.4 across a two-dimensional grid of impact parameters $\mathbf{b}$ surrounding the target. Its pattern shows where in space the electron is likely to deposit the fraction $\hbar\omega$ of its initial 0.1 MeV kinetic energy. By computing the electronic polarization induced in the target by the electron beam we see that the regions of high loss-probability occur at the characteristic nodes of each plasmonic wave function and at the rod ends, which are also effectively nodes. This is due to the fact that the longitudinal components of the electric force $F_{\parallel} = -eE_{\parallel}$ exerted by the electron beam maximally

coincide with the opposing plasmonic polarization vectors at each node of the plasmon wave function. This means that the potential energy of interaction between the polarization of the electron beam's electric field and the polarization of the plasmonic target is minimized at the position of each node. Depending upon the magnitude of the loss energy, $\hbar\omega$, different multipolar plasmons are excited, each with its own nodal structure (i.e., no nodes, 1 node, 2 nodes, *etc.*) and associated loss probability map.

In 2.4, we compare the experimentally determined loss-probability maps of the two lowest lying longitudinal plasmon resonances, labeled $n = 1, 2$, of the rod monomer (upper panels) with those computed *via* the *e*-DDA (middle panels). Excellent agreement between these data (as well as for the spectra in 2.2) indicates that the *e*-DDA provides a reasonable description of these electron-driven plasmonic excitations. For comparison, the lower two panels of 2.4 display the magnitude of the corresponding electric fields scattered from the rod when driven by a plane wave, computed *via* the DDA. To optically excite the $n = 2$ plasmon mode, which is dark, we rotate the propagation direction by $\pm 45^\circ$ from the normal in the plane containing the rod's long axis, and average the two scattered fields together to symmetrize the electric field magnitude; this rotation and averaging technique was used previously [82] to explain the observed loss-probability maps of dark plasmon modes. However, here we see that the scattered electric field magnitude misses certain details in the loss-probability map. For example, in the case of the $n = 2$ dark mode, $P_{\mathbf{b}}$ is largest in the middle of the rod and is smaller at the rod's ends; the electric field inverts these trends, even in the case of a monomer.

2.5 displays the loss-probability maps of the lowest energy bonding and antibonding plasmon

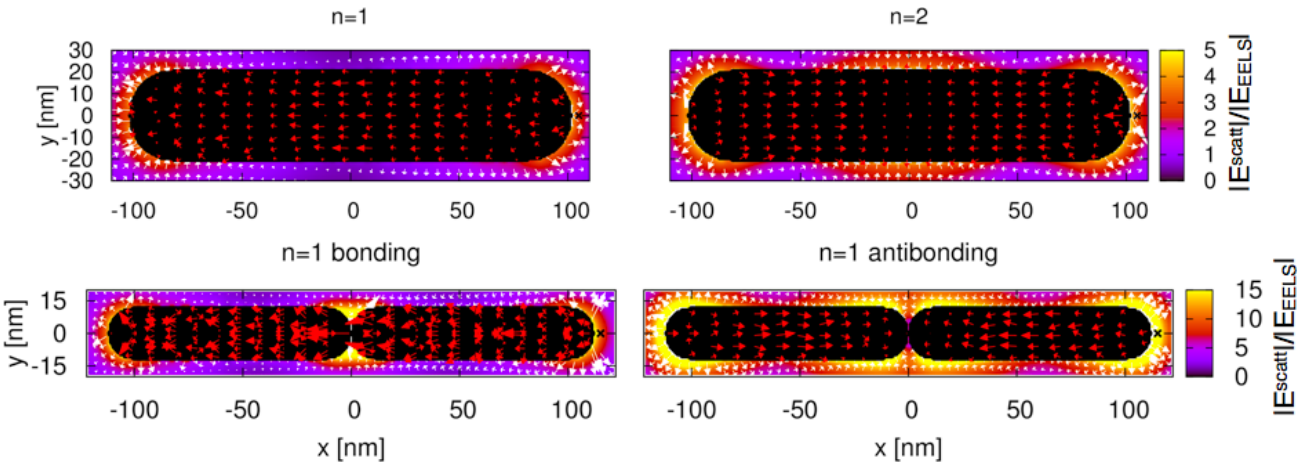

Figure 2.6: Induced polarization and electric field scattered from the nanorod monomer and dimer upon excitation by a 0.1 MeV electron beam located 1 nm away from the rod's right tip, as indicated by the "x". Both the polarization vectors (red arrows) and electric field vectors (white) and magnitude (background) are plotted in the plane bisecting the rod. Here the near-field magnitude is taken in ratio to the spatially anisotropic exciting field magnitude, corresponding to $\mathbf{E}_{\mathrm{EELS}}$. Each map is computed at the loss energies corresponding to the $n = 1$ (1.50 eV) and $n = 2$ (2.61 eV) bright and dark modes of the monomer and the $n = 1$ bonding (1.50 eV) and antibonding (1.95 eV) modes of the dimer; the former resonances are displayed in 2.2. Even with electron excitation, an electromagnetic hot spot is formed in the junction of the dimer at the loss energy corresponding to the $n = 1$ bonding mode.

resonances of the rod dimer, computed *via* the e-DDA. It is important to point out that $P_{\mathbf{b}}$ is nearly zero in the junction of the dimer at the loss energy corresponding to the bonding mode. Yet when excited by a plane wave at this energy, polarized along the dimer axis, the dimer supports an electromagnetic hot spot in the junction (not shown), implying a corresponding increase in the photonic local density of states. A related observation in the case of flat, disk-shaped dimers, showing the disconnect between EELS and the photonic local density of states, was demonstrated by Hohenester *et al.* [62] in contrast to earlier work [97]. This has led to the belief that EELS is unable to probe electromagnetic hot spots such as those responsible for SERS.

2.3.2 Electron-induced target polarization and electric near-field.

It is instructive to visualize the polarization induced in the nanorod target at different loss energies when the electron beam is fixed at a single point in space. The polarizations (red vectors) of the two lowest lying longitudinal plasmon resonances of the rod monomer and dimer are displayed in 2.6 in the plane that bisects the long axis of the rod, and that is perpendicular to the direction of propagation of the electron beam. Interestingly, it is clear that a single position of the electron beam (denoted by an "x") is sufficient to excite a spatially delocalized, multipolar, plasmonic resonance of the rod. Each plasmon mode, being a transient and oscillatory electronic density disturbance, generates a corresponding electromagnetic field as a decay channel by which to remove (conserve) energy. The near-zone scattered electric component of each is displayed in 2.6 with its magnitude shown in the background and its vector structure indicated by the overlaid white vectors. Because of the localized nature of the excitation source the induced polarizations and scattered electric fields are not symmetric, unlike the corresponding (g, u) plasmon eigenmodes induced by a plane wave of the same frequency.

2.3.3 Comparison of the electron- and photon-induced plasmon polarizations and scattered electric fields.

To compare the nature of the multipolar plasmonic excitations generated by either a photon (plane wave) or electron (EELS) source at the same excitation energy we define the following overlap measure

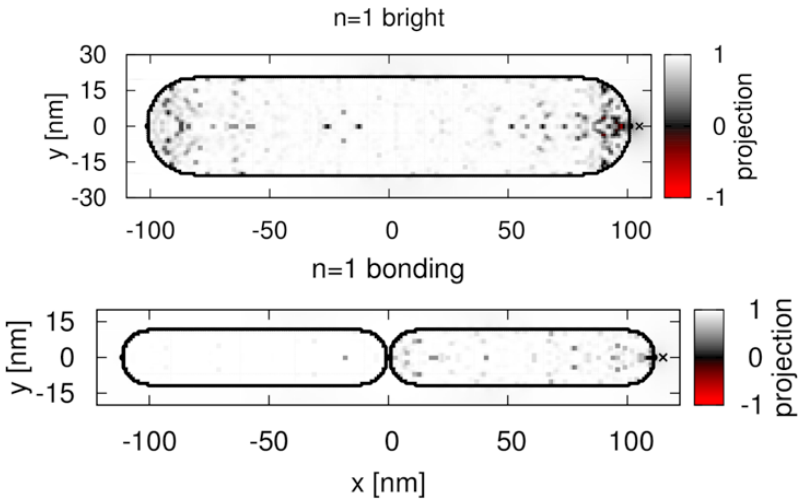

Figure 2.7: Projections of the electron- and photon-induced polarizations, $\Delta_{\mathbf{P}}$, and the electron- and photon-induced scattered electric near-fields, $\Delta_{\mathbf{E}}$, of the nanorod monomer and dimer. $\mathbf{P}$ and $\mathbf{E}^{\text{scatt}}$ are normalized to have unit length, making the projections a measure of the overlap of their directions only. Both the $n = 1$ monomer and $n = 1$ bonding dimer modes are optically bright. Spatial regions where the two polarization and scattered electric fields are the same (white) or opposite (red) in direction are clearly visible. Interestingly, the $n = 1$ bonding dimer mode shows that the electric field set up in the junction by a swift electron has the same directional dependence as the junction field induced by a plane wave. The position of the electron beam is denoted by an "x" and the polarization of the plane wave is directed along the long axis of the rod.

$$\Delta_{\mathbf{g}} = \frac{\mathbf{g}_{\text{photon}}}{|\mathbf{g}_{\text{photon}}|} \cdot \frac{\mathbf{g}_{\text{EELS}}}{|\mathbf{g}_{\text{EELS}}|}, \tag{2.5}$$

with $\mathbf{g} = \mathbf{P}$ or $\mathbf{E}^{\text{scatt}}$. We choose to normalize the plasmon polarization $\mathbf{P}$ and scattered electric field $\mathbf{E}^{\text{scatt}}$ from both sources to expose the directional dependence of the overlap, independent of their differing magnitudes. Clearly $-1 \leq \Delta_{\mathbf{g}} \leq 1$, with 1 implying that the directionality of $\mathbf{g}_{\text{photon}}$ and $\mathbf{g}_{\text{EELS}}$ is the same, -1 implying their directionality is opposite, and 0 implying they are orthogonal. 2.7 displays the projections $\Delta_{\mathbf{P}}$ and $\Delta_{\mathbf{E}}$ for both the rod monomer and dimer in the plane that bisects the long axis of the rod and that is

perpendicular to the direction of propagation of the electron and photon beams. The lowest energy $n = 1$ bright (1.50 eV) and bonding (1.50 eV) plasmonic excitations are chosen for comparison. For both monomer and dimer, the position of the electron beam is indicated by an "x" in the figures and the polarization of the plane wave is directed along the longitudinal axis of the rod.

It is evident from $\Delta_{\mathbf{P}}$ and $\Delta_{\mathbf{E}}$ that the optically bright plasmon modes of the monomer and dimer and their associated electric near-fields are almost directionally identical for both excitation sources. In the case of the dimer, it is important to point out that the electric field in the junction that is set up by the electron-driven bonding plasmon has near unit overlap with the junction field set up by a plane wave at the same energy. This is interesting because it shows that a swift electron can *indirectly* excite a junction field that is similar to the electromagnetic hot spot generated by plane wave excitation. In fact the two fields are directionally identical. This observation adds a *softening* of the statement that EELS is "completely blind to the hot spot" [62] that was based upon a comparison between EELS and the photonic local density of states. Through our numerical experimentation, comparing EELS to the vector-valued electric field itself, we see that EELS is not blind to hot spots if the observer knows how to correlate the loss probability map to the scattered electric near-field. For example, the loss probability map of the bonding dimer mode is bright at the ends of the dimer (2.4), indicating that this is the most efficient way to set up the bonding arrangement of the plasmon polarization needed to generate a capacitive- or hot spot-like field in the junction. This implies that the location where EELS probes may be spatially separated from where a hot spot is generated. Recent collaborative work with experiment

has shown this reasoning to be true even for complex three-dimensional aggregates that are determined to be single-molecule SERS active [89].

Lastly, we compute the projections, $\Delta_{\mathbf{E}}$, of the scattered electric far-fields induced by electron and photon sources (cathodoluminescence *versus* photoluminescence) for the two lowest energy plasmonic modes of the rod monomer and dimer. For these projections we evaluate $\mathbf{E}^{\text{scatt}}$ along a distant circle of radius 2 μm surrounding the target in the plane perpendicular to the direction of propagation of the electron and photon beams; the upper panel of 2.2 shows a representation of this distant circle in blue. For both the monomer's and dimer's $n = 1$ bright and bonding modes, $\Delta_{\mathbf{E}} \approx 1$ for all angles (not shown). This indicates that the electric field scattered by the monomer and dimer into the far-field are nearly identical in direction for both excitation sources for these modes. Knowing how these near- and far-fields behave suggests an electron-driven version of SERS experiment, where the flow of energy may be tracked between the electron source and a Raman-active molecule located within an electromagnetic hot spot.

2.4 Conclusion

In summary, we numerically implement the *e*-DDA, adding the exciting electric field of a swift electron [38] to the standard DDA of Draine [47]. This allows us to efficiently compute the plasmon polarization within and the electric field scattered from an arbitrary nanotarget excited by an electron source and to correlate these quantities with their photon-induced analogs, computed *via* the DDA. In our numerical investigations of the nanorod monomer

and dimer we learn how both bright and dark multipolar plasmons are selectively excited and how they funnel energy from the near-field to the far-field. We also learn, in the case of the nanorod dimer, that EELS can indirectly indicate the presence and even location of a junction field that is directionally identical to the hot spot set up by plane wave excitation. This is demonstrated by comparing the loss-probability map to the vector-valued electric near-field, rather than to the photonic local density of states. Recent experiment has demonstrated that this numerical observation on rod dimers is also true for more complex nanostructures [89].

2.5 Methods

2.5.1 Continuum electrodynamics simulations.

The DDA is routinely used to study the response of metal nanoparticles subjected to optical-frequency radiation [98]. In this approximation the target is discretized into a finite collection of polarizable point dipoles $\mathbf{P}_j$, $1 \leq j \leq N$, each driven by an exciting plane-polarized electric field as well as by the fully retarded electric-dipole field $\sum_{k \neq j}^{N} \mathbf{\Lambda}_{jk} \cdot \mathbf{P}_k$ generated by all other points; here $\mathbf{\Lambda}_{jk} = e^{ikr_{jk}}\{(1/r_{jk}^3 - ik/r_{jk}^2)[3\hat{\mathbf{n}}_{jk}\hat{\mathbf{n}}_{jk} - \mathbf{1}_{jk}] - k^2\hat{\mathbf{n}}_{jk} \times (\hat{\mathbf{n}}_{jk} \times)/r_{jk}\}$ is the standard

dipole tensor that relays the electric field generated by a dipole at one point in space $\mathbf{x}_j$ to another $\mathbf{x}_k$ a distance $r_{jk}\hat{\mathbf{n}}_{jk} = |\mathbf{x}_j - \mathbf{x}_k|\hat{\mathbf{n}}_{jk}$ away. In this manner, the responses of the system that are optically accessible can be computed once each dipole is brought into self consistency with all others at a certain excitation frequency, ω. This is accomplished through the iterative solution of the following equation,

$$\sum_{k=1}^{N}[\boldsymbol{\alpha}_{jk}^{-1}(\omega) - (1-\delta_{jk})\boldsymbol{\Lambda}_{\mathbf{jk}}] \cdot \mathbf{P}_k(\omega) = \mathbf{E}_{\text{photon}}(\mathbf{x}_j, \omega), \tag{2.6}$$

and depends upon the frequency-dependent linear polarizability $\boldsymbol{\alpha}_{jk}(\omega) \equiv \boldsymbol{\alpha}_j(\epsilon(\omega))\delta_{jk}$ of the target point j. The polarizability is related to the dielectric function through the lattice dispersion relation [99].

Our numerical approach, which we call e-DDA, replaces the exciting field of the plane wave, $\mathbf{E}_{\text{photon}}$, with that of a swift electron, $\mathbf{E}_{\text{EELS}}$, given in 2.2[38]; $\gamma = 1/\sqrt{1-\epsilon(v/c)^2}$ is the Lorentz factor involving the dielectric function ϵ of the background medium, which is taken to be vacuum in all calculations, and v is the electron's incident velocity corresponding to the incident kinetic energy $m\gamma c^2 - mc^2$. We choose the phase $e^{i\omega z/v} = 1$ at the z-height of the mass centroid of the target. Otherwise, we use the existing DDSCAT numerical algorithm to solve the resulting e-DDA equations. This allows us to efficiently compute the EEL spectra at hundreds to thousands of points surrounding the nanotarget, in parallel. The e-DDA source code is distributed free of charge under the GNU General Public License at `http://faculty.washington.edu/masiello` [100].

All e-DDA and DDA simulations performed in this article involve nanorods that are supported upon a 5 nm thick amorphous SiN_x substrate. The substrate is located directly below the target, with no gap in between the two media. All target structures are excited by a 0.1 MeV electron beam directed normal to the substrate; the corresponding velocity of the electrons in the beam is 0.55 c. Only points external to the target are considered in the simulations and the two-dimensional grid of impact parameters $\mathbf{b}$ for the electron beam is chosen to have a 1 nm spacing. Dielectric data from Johnson and Christy [101] is used for silver, while those for the substrate are taken from Palik [102]. An interdipole spacing of 1 nm for both target and substrate is used throughout; other dipole spacings were tested to ensure that all spectra are converged at this value. Similarly, all electric fields are evaluated on a grid with 1 nm grid spacing.

2.5.2 STEM/EELS experiment.

A description of the correlated optical and STEM/EELS data collection methods are described in detail elsewhere [82]. Briefly, a 2 μL aliquot of the colloidal nanoparticles is drop-coated onto a TEM grid and allowed to dry in air. The sample is subsequently loaded onto an inverted optical microscope equipped with a dark-field condenser and wide-field imaging camera. Under dark-field conditions, the resonance Rayleigh spectra of the individual nanoparticles is recorded, as well as the wide-field image showing the individual particles as diffraction-limited spots. After transferring the sample to an aberration-corrected STEM equipped with EELS, the wide-field images obtained on the optical and electron microscopes

are compared and pattern-matching is used to determine the particle of interest [103]. The nanoparticles, when viewed on the STEM, are observed to be monodisperse and comprise a range of shapes and sizes. EEL spectra are recorded for every pixel in the region of interest, which encompasses the entire nanorod. From this large data set, we extract either EEL spectra at a particular spatial point (2.3), or we plot the loss intensity for a specific energy loss (2.4). The energy resolution of the EELS is determined from the full width half-maximum of the zero-loss peak, and is 0.4-0.5 eV for the current experiments.

2.6 Acknowledgements

This work was supported by the University of Tennessee, the UT/ORNL Joint Institute for Advanced Materials, and the U.S. Department of Energy, Office of Basic Energy Sciences under award number DE-SC0004792 (J.P.C.). D.J.M. acknowledges financial support from the University of Washington College of Arts and Sciences and Department of Chemistry. All computations were performed through the University of Tennessee's Newton HPC Program.

2.7 Supporting information available.

Download instructions for the *e*-DDA source code. This information is available free of charge *via* the Internet at `http://pubs.acs.org`.

Chapter 3

Single-Molecule Surface-Enhanced Raman Scattering: Can STEM/EELS Image Electromagnetic Hot Spots?

This work has previously been published in the following article:

N. Mirsaleh-Kohan[#], V. Iberi[#], P. D. Simmons Jr., N. W. Bigelow, A. Vaschillo, M. M. Rowland, M. D. Best, S. J. Pennycook, D. J. Masiello, B. S. Guiton, and J. P. Camden.

Journal of Physical Chemistry Letters **3**, 2303 (2012)

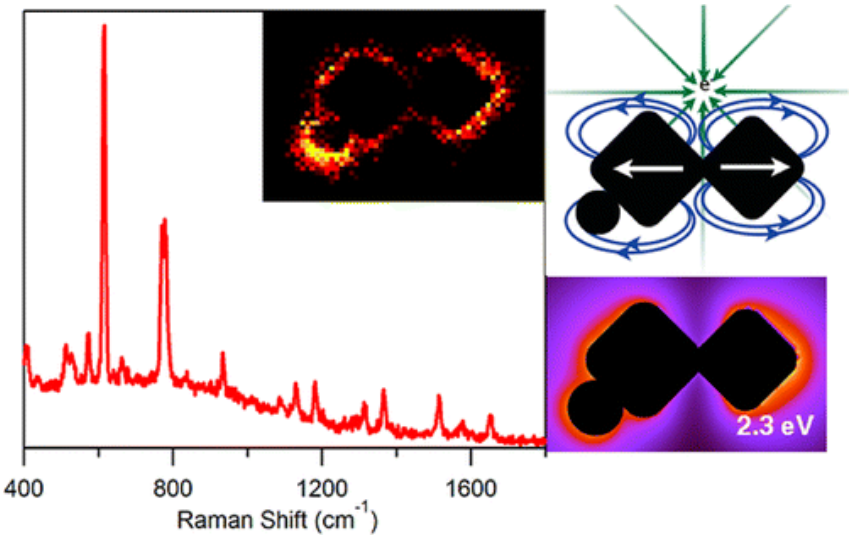

Figure 3.1: Abstract figure.

3.1 Abstract

Since the observation of single-molecule surface-enhanced Raman scattering (SMSERS) in 1997, questions regarding the nature of the electromagnetic hot spots responsible for such observations still persist. For the first time, we employ electron energy-loss spectroscopy (EELS) in a scanning transmission electron microscope (STEM) to obtain maps of the localized surface plasmon modes of SMSERS-active nanostructures, which are resolved in both space and energy. Single-molecule character is confirmed by the bianalyte approach using two isotopologues of Rhodamine 6G. Surprisingly, the STEM/EELS plasmon maps do not show any direct signature of an electromagnetic hot spot in the gaps between the nanoparticles. The origins of this observation are explored using a fully three-dimensional electrodynamics simulation of both the electron energy loss probability and the near-electric field enhancements. The calculations suggest that electron beam excitation of the hot spot is possible, but only when the electron beam is located outside of the junction region.

3.2 Can STEM/EELS image electromagnetic hot spots?

Surface-enhanced Raman scattering (SERS) [104–106], discovered more than three decades ago, relies on the localized surface plasmon resonance (LSPR) [107, 108] to deliver large Raman enhancement factors ($10^6 - 10^{10}$) to molecules located close to the surface of plasmonic nanostructures. The SERS effect is so dramatic that, despite the weakness of Raman scattering, the vibrational spectrum of a single molecule can be easily observed [18, 19]. The claims of single-molecule SERS (SMSERS) were initially met with skepticism because of the extraordinary enhancements proposed (10^{15}), and efforts immediately turned to proving the existence of SMSERS [109–111] and characterizing the nanostructures that gave rise to such massive enhancements [112–115]. More than 15 years later it has become widely accepted that electromagnetic hot spots play a major role in SMSERS. In the electromagnetic mechanism (EM) of SERS, excitation of the LSPR in a plasmonic nanostructured material leads to a significant electric field enhancement (EFE) at the particle surface, and the Raman cross section of molecules in this enhanced field can be increased by several orders of magnitude [108, 116]. Electromagnetic enhancements of $10^{10} - 10^{11}$ at the junction between two closely spaced metallic particles (hot spots) have been predicted [112, 117, 118], although the maximum achievable enhancements are moderately reduced when quantum effects are taken into account [119]. Also, studies have shown that more modest enhancement factors (on the order of $10^7 - 10^8$) are sufficient to observe a single molecule in SERS for a resonant molecule such as Rhodamine 6G (R6G) [120].

While the idea of electromagnetic hot spots in SERS is well-known [121, 122], Brus and

co-workers [20, 123] showed using polarization studies that hot spots formed at the junction of two nanoparticles likely play a major role in SMSERS. This claim was further supported by atomic force microscopy showing that SMSERS-active structures are aggregates of Ag nanoparticles. A study correlating high resolution transmission electron micros-copy (HRTEM), SMSERS, and LSPR showed that multiple aggregate nanostructures 100 nm in size were suitable for observing SMSERS and continuum electrodynamics calculations on the simplest SMSERS-active aggregates, also confirming that the hot spot was located near the interparticle junctions [21, 31]. Wustholz et al. [124] demonstrated that the EFE can reach its maximum when two particles are in subnanometer proximity or have coalesced to form crevices. Studies performing high-resolution two-dimensional (2D) imaging of SMSERS hot spots measured the spatial distribution of the SMSERS centroid position and the SERS intensity [125, 126], and these studies were later expanded to include images of the active aggregates [127]. A recent theoretical investigation of the spatial, spectral, and polarization dependence of the electro-magnetic SMSERS-active hot spots showed that high electro-magnetic field strength can be produced at multiple *spectral* and *spatial* locations [31]. This study further demonstrated that some hot spots exist due to the collective and phase-uniform excitation of LSPRs, while others originate from interfering plasmonic excitations resulting from scattering from gaps and surfaces.

Despite the large body of evidence in favor of electromagnetic hot spots, only now have techniques emerged that can image plasmons with the spatial (¡1 nm) and energy resolutions (0.1-0.3 eV) necessary to observe the elusive electromagnetic hot spots, which are thought to be essential for SMSERS. One such technique is electron energy-loss spectroscopy (EELS)

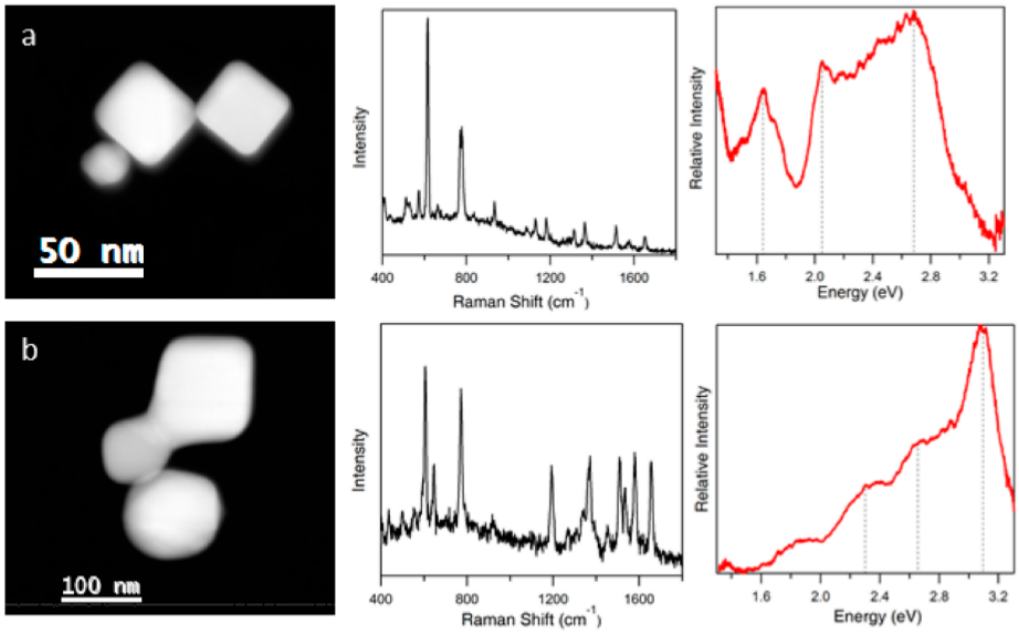

Figure 3.2: ADF images (left), Raman scattering (middle), and resonance-Rayleigh (right) scattering spectra of two SMSERS-active trimer structures. Single molecule character was confirmed using the isotopologue method.

in a scanning transmission electron microscopy (STEM) [11, 55, 79–81, 83, 84, 94, 128, 129]. The power of this technique is derived from its ability to experimentally render the photonic local density of states (LDOS). Using a Greens function approach, Garcia de Abajo and Kociak [97] concluded that the energy loss probability is directly related to the LDOS in arbitrary systems. Numerical simulations support this conclusion, and they further emphasize the correspondence between the projection of the LDOS onto the electron trajectory and the EELS signal [97]. Hohenester, Ditlbacher, and Krenn [62] considered this same question and instead concluded that there exists no clear-cut relation between EELS and LDOS [62]. They further examined coupled, flat metallic nanostructures and state that EELS can be blind to the hot spots in the gap region between particles. These theoretical studies focused on structures that are quasi-planar, and it is not clear to what extent the results apply to the

complex three-dimensional (3D) nanoaggregates encountered in SMSERS, where the imaging of hot spots takes on primary importance. Previous experimental studies have examined (mostly planar) coupled nanoparticle structures [79, 81, 84, 94, 128], although none of them were known to be SMSERS-active.

Herein, we present the first STEM/EELS imaging study of plasmon modes in nanostructures *confirmed* to be SMSERS-active. Our STEM/EELS studies do *not* show an enhanced EEL in the gap regions between nanoparticles, where one would expect the electromagnetic hot spots to be located. Further, we support our experimental findings with a fully three-dimensional electrodynamics simulation of both the near-electric field enhancement (hot spot) and EELS loss probability, for the exact nanoparticle geometry obtained from the experiment. The simulations are in full agreement with the experimental results and yield insights into the specific EEL signatures associated with hot spots.

In our experiment, SMSERS-active clusters were identified using the bianalyte approach [109, 130], which relies on two isotopologues of Rhodamine 6G, 9R6G $-$ d_0 and R6G $-$ d_4. Briefly, Ag nanoparticles were treated with a low concentration of the mixture of R6G $-$ d_0 and R6G $-$ d_4 (ca. $10^{-}9M$) such that approximately one R6G molecule, either R6G $-$ d_0 or R6G $-$ d_4 was adsorbed per active site according to the Poisson distribution [110] (see Supporting Information (SI), Figure 3.6). Many SMSERS-active aggregates were analyzed with our correlated STEM/EELS/optical approach to ensure a representative data set. 3.2 presents correlated annular dark field (ADF) images and optical spectra of two representative nanostructures confirmed to be SMSERS-active. In good agreement with previous HRTEM

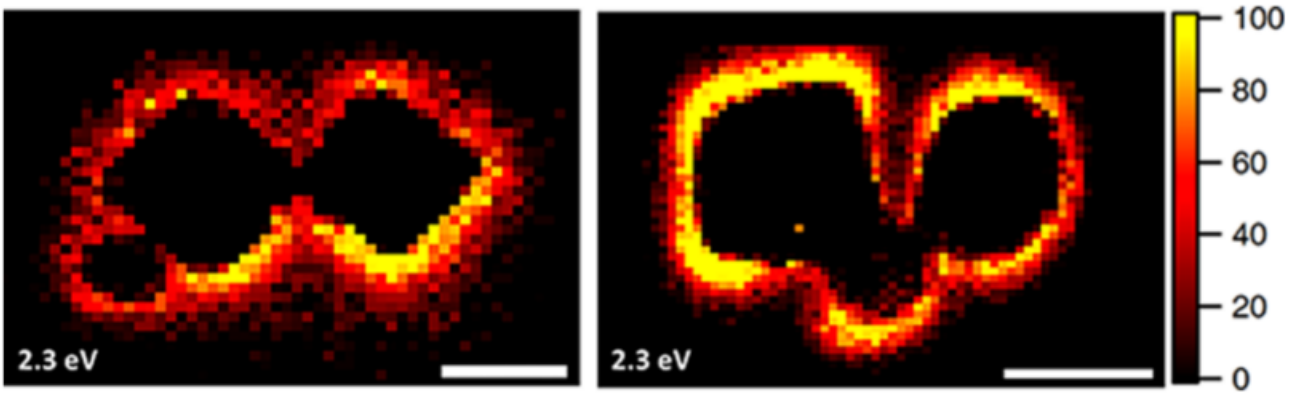

Figure 3.3: Spatially resolved EEL maps for a loss energy of 2.3 eV for SMSERS-active trimers. Images have been normalized to the ZLP. A complete EEL spectrum is obtained for every pixel in the region of interest (defined by the ADF in 3.2); however, we focus on the loss energy of 2.3 eV as this corresponds to the energy of the Raman laser (532 nm, 2.3 eV) used in the SMSERS experiment. (Images for other loss features are available in the SI.) While it is assumed that the largest electromagnetic enhancement is obtained at the gap region, no localization of the EEL intensity is observed in the gaps. Scale bars are 50 nm (left) and 100 nm (right).

studies [21], our structures consist of a number of nanoparticles with varying degrees of contact. These contact regions, which we calljunctions, arise from coalesced or closely spaced structures and are thought to support electromagnetic hot spots. 3.2 also displays the Raman spectra, without baseline or background correction, and the resonance-Rayleigh scattering measurements of the two SMSERS-active particles. As previous studies have indicated, there is no correlation between the SERS enhancement factor and the LSPR maximum [20, 21].

When preparing SMSERS-active nanoclusters via aggregation, only a few percent of the total aggregates are found to be active [131]. This small population of active aggregates is due, in part, to the low analyte concentrations required to ensure single molecule character; however, it is additionally assumed that only special aggregates generate an electromagnetic

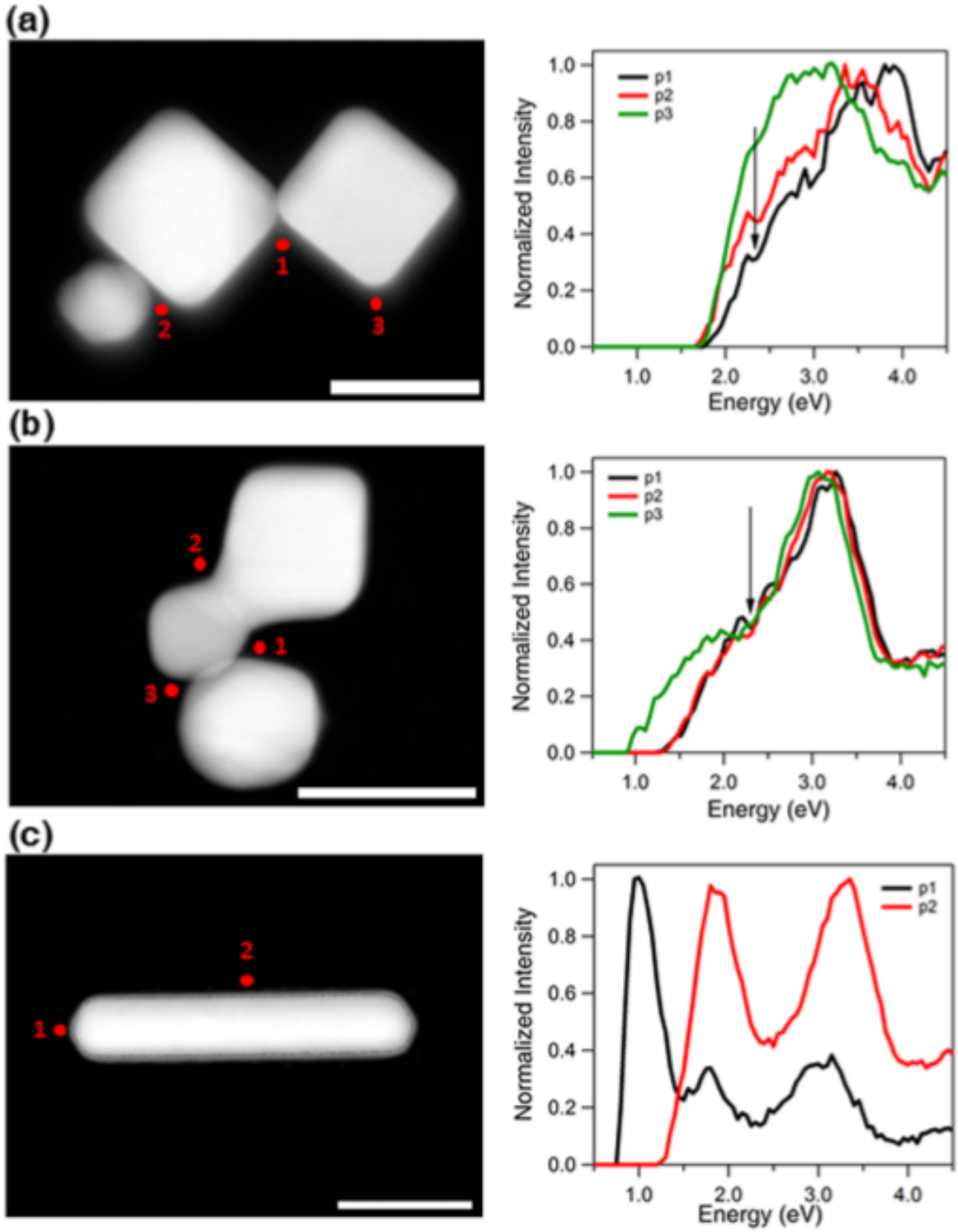

Figure 3.4: ADF images (left) and EEL spectra (right) for selected points around the SMSERS-active structures (a,b). For comparison, the EEL spectra and ADF images of a nanorod are adapted from [129]. The energy of the laser line used in our experiment (532 nm $\approx$ 2.3 eV) is indicated with an arrow in the graphs. The spectra have been normalized so the highest point is 1. Scale bars are 50 nm (a), 100 nm (b), and 50 nm (c).

hot spot on resonance with the excitation laser. In this picture, these special aggregates lead to the strongest SMSERS signal; although, theoretical studies [31] have cautioned that one aggregate may have multiple hot spots and that the maximum electromagnetic enhancement may be a weak function of the laser excitation energy. To examine the possibility of an electromagnetic hot spot at the energy of our resonance-Raman experiments (532 nm, 2.3 eV) we plot, in 3.3, the spatially resolved intensity corresponding to an electron energy loss of 2.3 eV for the structures shown in 3.2. We emphasize that the image obtained in 3.3 is not dependent on the EELS data processing method. Raw energy slices of EEL (spectra after centering, normalizing to the zero loss peak (ZLP), and subtracting the ZLP), and plasmon modes extracted using the Automated eXpert Spectral Image Analysis (AXSIA) program, are similar to those presented in 3.3 (see SI Figures 3.7b, 3.8b, 3.9c, 3.10b). These results demonstrate that there is no localization of the EEL intensity in the gaps at 2.3 eV, even at the junctions between the particles.

We have also extracted EEL spectra from the gap regions and display them in 3.4. This allows us to probe resonances occurring at energies *different* from the excitation laser, e.g., an exceptionally bright aggregate may yield SMSERS activity, even when the laser is off resonance from the hot spot. As evident from 3.4a,b, we do not observe any sharp resonance for either trimer at the points located between the nanoparticles. One might object that the energy resolution of the current experiment (0.5 eV) is insufficient to resolve some of the modes (e.g., modes corresponding to the gap between the nanoparticles); therefore, for comparison, we have also included in 3.4 EELS data for a nanorod adapted from our previously published work [129]. For the nanorod, we observe well-resolved (spatial and spectral)

plasmon resonances.

While it is well-known that extreme near-electric-field enhancements can be obtained at locations near sharp surface protrusions or in nanogaps [112, 117, 118], our EELS results do not show a clear localization of the EEL intensity at the junction of two nanoparticles. In order to examine this observation in detail, we employ a modified version of the discrete-dipole approximation (DDA), called *electron-driven* DDA (*e*-DDA) [60], which imposes the electric field of a swift electron [76, 132],

$$\mathbf{E}_{\mathrm{EELS}}(\mathbf{x},\omega) = \frac{2e\omega}{v^2\epsilon\gamma} e^{i\omega z/v}\Big[\frac{i}{\gamma}\mathrm{K}_0\Big(\frac{\omega b}{v\gamma}\Big)\hat{\mathbf{v}} - \mathrm{K}_1\Big(\frac{\omega b}{v\gamma}\Big)\hat{\mathbf{b}}\Big] \tag{3.1}$$

rather than a plane wave upon a fully three-dimensional target located a distance $|\mathbf{x}| = (|\mathbf{b}|^2 + z^2)^{1/2}$ away from the direction of propagation, $\hat{\mathbf{v}}$. In this expression, v is the speed of the electron, chosen to propagate along the z-axis, $\gamma = 1/(1-\epsilon(v/c)^2)^{1/2}$, and K_0 and K_1 are modified Bessel functions. As in the DDA, the target is discretized into a finite collection of N polarizable points that are each driven by the field of the electron (eq 1) and by the electric-dipole field of all other target points. Each point is described by a linear polarizability that depends upon the complex-valued and frequency-dependent dielectric function of the bulk material [102]. When the electron beam is positioned near the target, the EEL spectra at each impact parameter b can be computed from the loss probability per unit frequency [11, 133],

$$P_{\mathbf{b}}(\omega) = \frac{1}{\pi\hbar}\mathrm{Im}\sum_{j=1}^{N}\mathbf{E}^{*}(\mathbf{x}_j,\omega)\cdot\mathbf{P}_j(\omega) \tag{3.2}$$

where $\mathbf{P}_j$ is the dipole moment of the j^{th} target dipole, and $\mathbf{E}$ is the electric field of the swift electron evaluated at position j. Further details of the theoretical methods are available in the SI, and an in-depth comparison of e-DDA calculations with experimental STEM/EELS measurements are the subject of a companion manuscript [60].

3.5(a) compares compares the calculated electric near-field magnitude, obtained from plane wave excitation (DDA), and the energy loss-probability map, obtained from a 100 keV electron beam (e-DDA). The calculation in both cases is performed at an energy of 2.3 eV corresponding to excitation with 532 nm light or a 2.3 eV energy loss from the electron beam.

The calculated loss-probability map (3.5a, right panel) compares well with the experiment (3.3), although small differences are observed, likely due to the complex nature of the nanoaggregates, imperfect reconstruction of the experimental ADF image to an array of dipoles, and variations in the local environment of the aggregate. Even though this structure is predicted to have an intense electromagnetic hot spot in the junction region under plane wave excitation (3.5a, left panel), and is known to be SMSERS-active, a strong EEL probability in the junction region at 532 nm is not observed in either the STEM/EELS experiment or the e-DDA theory. We do, however, observe strong loss features at points external to the junctions (3.5).

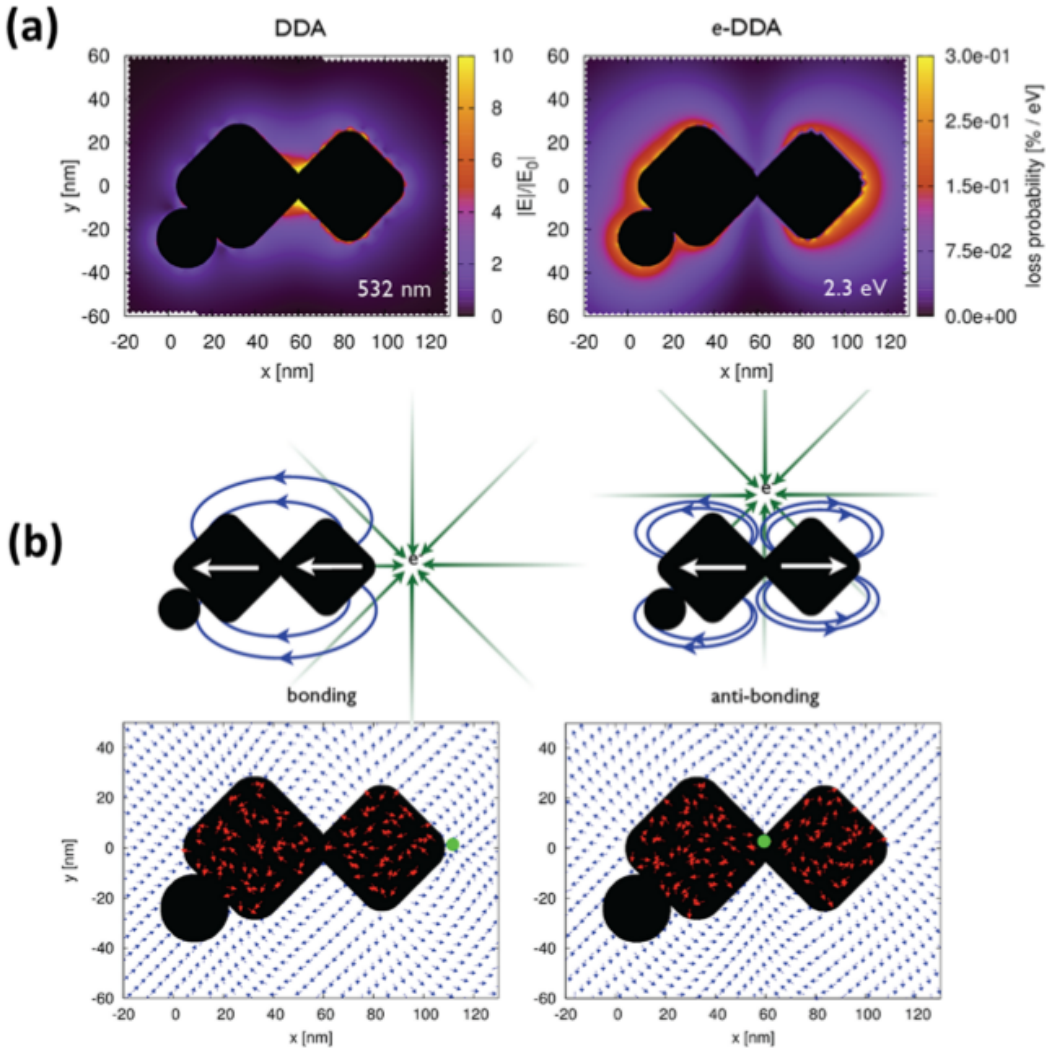

Figure 3.5: (a) Comparison of the calculated electric near-field magnitude obtained from plane wave excitation (left) with the EEL probability map for a 100 keV electron beam (right) for the SMSERS-active trimer displayed in 3.2. Simulation of the plane wave excitation is performed via the DDA at a wavelength of 532 nm. The wave vector of the excitation field is directed along the z axis and is polarized along the x-axis. The 2D slice displayed corresponds to the plane where the electric-field magnitude is maximized. Other polarizations, wave-vector directions, and projection planes were examined and show similar localization of the field in the junction regions. The loss probability map, computed via the *e*-DDA, is displayed at a corresponding loss energy of 2.3 eV. In agreement with the experiment, the EEL map does not show an intense loss probability in the junction region. (b) Induced polarization maps (2.3 eV) obtained for two different positions of the electron beam (green bullet). Placement of the electron beam in the junction leads to a net antibonding arrangement of dipoles (right), whereas placement of the electron beam on the outside right corner leads to a net bonding arrangement (left). Also shown is the induced polarization (red vectors) and resulting scattered electric field (blue vectors), both normalized to unity to aid visualization. Both panels display 2D slices taken from fully 3D simulations of the trimer. The plane of visualization was chosen to lie at the height of the centroid of the two cubes.

Insight into these features can be explored by computing the polarization induced in the target at 2.3 eV for different electron-beam positions (3.5b). Our analysis suggests that the planar model of bonding and antibonding dipoles [62] is applicable to the more complex geometries observed in SMSERS. When the electron beam is positioned in the junction, the calculations show that a net *antibonding* arrangement of the targets polarization vectors is induced. This leads to a node of the scattered electric field in the junction and a small loss probability results. When the electron beam is positioned on the right side of the nanoaggregate, a net *bonding* arrangement of the induced polarization vectors is obtained. This underlies a capacitive electric field that is localized in the junction and is characteristic of an electro-magnetic hot spot. In fact, we show in a related paper that the electron-induced junction field and the hot spot set up by plane wave excitation are directionally identical [60].

Both of these arrangements of the targets electronic polarization are due to the forces exerted by the polarization of the electric field of the swift electron. Interestingly, this means that the electromagnetic hot spot can indeed be excited by the electron beam, and that it is in principle possible to induce Raman scattering from the single molecule with the electron beam.

In summary, we present, for the first time, plasmon maps of SMSERS-active nanoparticles employing STEM/EELS. Although it is widely accepted that electromagnetic hot spots are responsible for SMSERS activity, and are located between the gaps of nanoparticles, we do *not* see a large EEL intensity in these regions. We have rigorously confirmed that each

structure examined indeed gives rise to SMSERS before EELS imaging. Our experimental results are complemented with a fully 3D simulation that builds the electron-beam excitation directly into the DDA and utilizes shape parameters derived from the experiment. The simulations are in good agreement with the experimental results and yield insights into the specific EEL signatures associated with hot spots. In other words, the electromagnetic hot spot can be excited when the electron beam is positioned at the periphery of the nanoaggregate. With the rapid emergence of STEM/EELS as a tool for probing the plasmonic properties of nanostructures, we believe the work presented here will impact a wide range of STEM/EELS plasmon imaging experiments going forward.

3.3 Methods

R6G $-$ d_4 was synthesized according to the procedure described by Blackie and co-workers,48 with NMR and mass spectrometry data of the resulting compound matching this prior report. Ag nanoparticles were treated with a low concentration of the mixture of R6G $-$ d_0 and R6G $-$ d_4 (ca. 10^{-9} M) such that approximately one R6G molecule, either R6G $-$ d_0 or R6G $-$ d_4 was adsorbed per active site according to the Poisson distribution [110] (3.6). Silver nanoparticles were obtained from nanoComposix and used without further purification. In our experiment, no salt was added to the SMSERS solution since previous nanoparticle studies had demonstrated the existence of sufficient aggregations, and, for the purpose of this study, simpler structures with not many overlapping nanostructures were desired. Two hundred mesh Cu grids coated with holey carbon (SPI supplies #3540C-FA) were used as

TEM supports. A 3 μL aliquot of the SMSERS solution was drop-coated directly onto the TEM grid, and the solvent was allowed to evaporate. After deposition, the sample was placed on a coverslip, mounted in a custom-designed sample holder, and purged with dry nitrogen. For the Raman scattering, the sample was irradiated with 532 nm linearly polarized laser light (Spectra Physics, model J-20) at a grazing incidence with a power density of 0.03 W/cm^2. Optical measurements were carried out on an inverted microscope (Nikon, Ti-U) equipped with a dark field condenser (Nikon, NA = 0.95-0.80) and an ultrasteep Raman long-pass edge filter (Semrock) to block the laser Rayleigh line. Raman spectra were collected using a 100X (Nikon, $0.7 < \text{NA} < 1.4$, oil immersion) objective and detected on a liquid nitrogen-cooled back-illuminated charge-coupled detector (CCD) (Princeton Instruments, PIXIS 100). Resonance-Rayleigh scattering measurements were performed on the SMSERS-active nanoparticles after removing the long-pass edge filter utilizing the unpolarized light output of a tungsten-halogen lamp. A wide-field image of the silver nanoparticles on the TEM grid was also recorded to serve as a map for subsequent characterization in the STEM. This method enabled correlated optical and STEM measurements of the exact same SMSERS-active nanostructures with an average of 15 active clusters per grid.

After identification and optical characterization of active SMSERS nanoparticles, the sample was inserted into an aberration-corrected, cold-field-emission STEM (VG Microscopes HB501UX STEM with Nion aberration corrector and Gatan Enfina EEL spectrometer). The SMSERS-active nanoparticles were found by comparing the dark-field optical map to the pattern of particles visible in the STEM at very low resolution [103]. After identification, a high-resolution ADF image and an EEL spectrum image were collected from the ZLP

containing region, i.e., an EEL spectrum is recorded at each pixel over the entire region of interest. The spectrometer dispersion was set to 0.05 eV per channel with an exposure time of 0.05 s per spectrum. The pixel size/density (60 $\times$ 37 pixels for 3.3, left and 57 $\times$ 76 pixels for 3.3, right, with a spatial resolution of $\sim$3 nm per pixel) was chosen to give a total acquisition time of around 11 min for a single spectrum image. Shorter acquisition times were used to avoid accumulation of contaminations caused by the electron beam. The energy resolution, determined by the full-width-half-maximum of the ZLP, was $\sim$0.5-0.55 eV. The STEM/EELS data were analyzed using three different approaches: in the first approach, the raw EELS data were examined after centering the ZLP of each spectrum at 0 eV, normalizing to the ZLP, and subtracting the ZLP, leaving only the inelastic contributions to the spectrum image. In the second approach, for a particular pixel of interest, the complete EEL spectra, after centering and subtracting the ZLP, were background subtracted and plotted for different probe positions on the entire structure. In a third and final approach, multivariate statistical analysis employing the AXSIA program [134, 135] was applied to the data to extract statistically significant component spectra and maps; details of this analysis have been discussed in our previously published work [82]. The data analysis using AXSIA is presented in the SI. Our experimental measurements are also supported by electrodynamics simulations based on the DDA [47, 136] and the details are presented in the SI.

3.4 Supplimental information

3.4.1 Simulation methods

Discrete Dipole Approximation (DDA) calculations [47, 136] were utilized to examine the electromagnetic-field properties of the trimer aggregate shown in the Figure 1a of the manuscript. In the DDA the target is discretized in to a collection of polarizable points, each induced by its interaction with an incident plane wave and with fields arising from the other polarizable elements. Structural parameters for the SMSERS-active nanostructures, such as the edge length, corner rounding (radius of curvature), and the gaps between the nanoparticles were obtained from the experimental annular dark field (ADF) image and were used to build the dipole array. These fields are calculated half a grid spacing from the surface, instead of immediately on the surface, in order to avoid numerical instabilities that arise at the surface. The grid spacing used was 2 nm, the dielectric constants of silver were from Palik [102], and the effective medium approximation of 1.35 was employed to include the substrate effect implicitly. The effective medium approximation is a well-documented method to include the effects of substrate and the environment of the nanoparticles and defines an average dielectric function to describe the optical response of the entire aggregate [137]. Simulation of the plane wave excitation is performed at a wavelength of 532 nm. The wave vector of the excitation field is directed along the z-axis and is polarized along the x-axis. The two-dimensional slice displayed corresponds to the plane where the electric-field magnitude is maximized. Other polarizations, wave-vector directions, and projection planes were examined and show similar localization of the field in the junction regions. The loss-probability map, computed via the *e*-DDA, is displayed at a corresponding loss energy of 2.3 eV. In agreement with the

experiment, the EEL map does not show an intense loss probability in the junction region.

3.5 Author contributions

#These authors contributed equally to this work.

3.6 Notes

The authors declare no competing financial interest.

3.7 Acknowledgements

This research was supported by the Eugene P. Wigner Fellowship program of the Oak Ridge National Laboratory and University of Kentucky (B.S.G.), University of Tennessee (UT) Office of Research, College of Arts and Sciences, and Department of Chemistry, the UT/ORNL Joint Institute for Advanced Materials, and the U.S. Department of Energy, Office of Basic Energy Sciences, under Award Number DE-SC0004792 (V.I., N.M.K., J.P.C.); the Office of Basic Energy Sciences, Materials Sciences and Engineering Division, U.S. Department of Energy (S.J.P.); the National Science Foundation under Awards CHE-0954297 and DMR-0906752 (M.D.B., M.M.R.); the University of Washington College of Arts and Sciences and Department of Chemistry (N.W.B., A.V., D.J.M.). N.M.K. and V.I. also thank Dr. Andrew R. Lupini for assistance with the EELS data analysis.

3.8 Supplimental figures

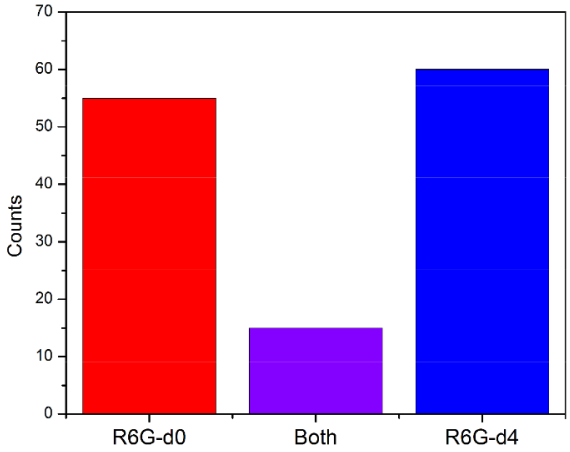

Figure 3.6: Histogram showing the frequency with which only $R6G - d_0$ (red), only $R6G - d_4$ (blue) and both $R6G - d_0$ and $R6G - d_4$ (purple) vibrational modes were observed. Nanoparticles were treated with a low concentration of the mixture of $R6G - d_0$ and $R6G - d_4$ (ca. 10^{-9} M) such that approximately one R6G molecule, either $R6G - d_0$ or $R6G - d_4$ was adsorbed per active site according to the Poisson distribution.

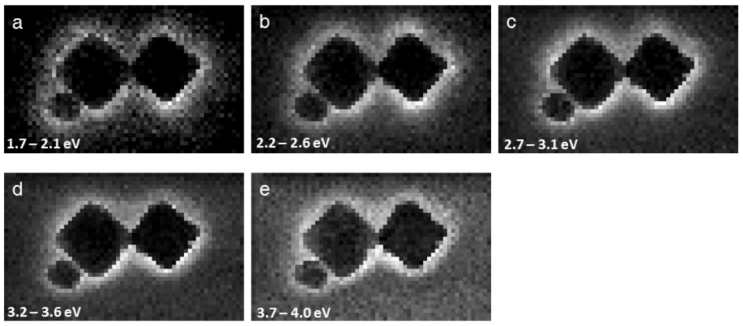

Figure 3.7: Energy slices from the spectrum image of trimer, *after* centering, normalizing to zero-loss peak (ZLP) and subtracting ZLP, but *before* noise reduction with principal components analysis.

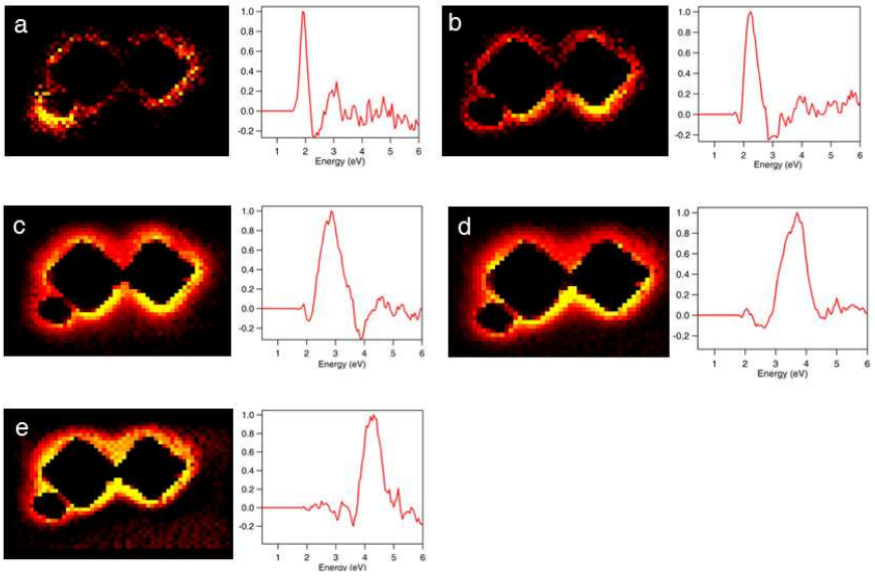

Figure 3.8: Plasmon maps and loading spectra of SMSERS active nanostructures using AXSIA. Multivariate statistical analysis (MVSA) employing the AXSIA program, was applied to the data to extract statistically significant component spectra and maps.

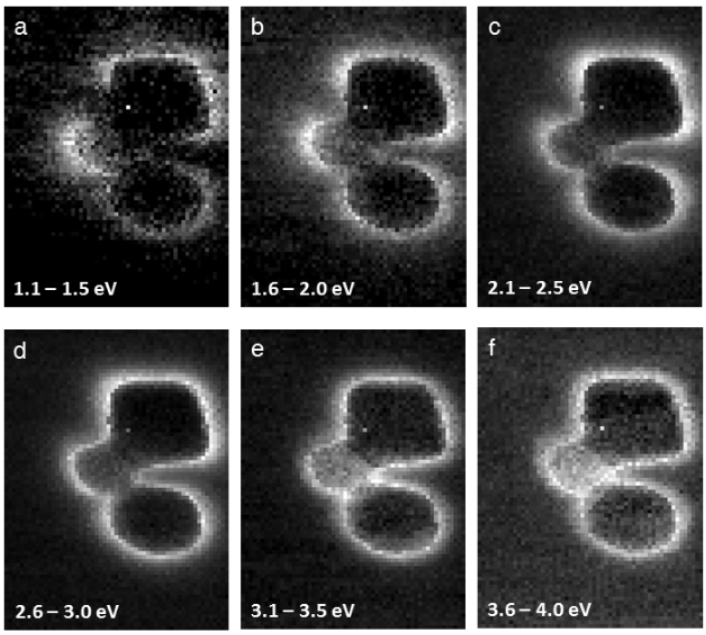

Figure 3.9: Energy slices from the spectrum image of trimer, *after* centering, normalizing to zero-loss peak (ZLP) and subtracting ZLP, but *before* noise reduction with principal components analysis.

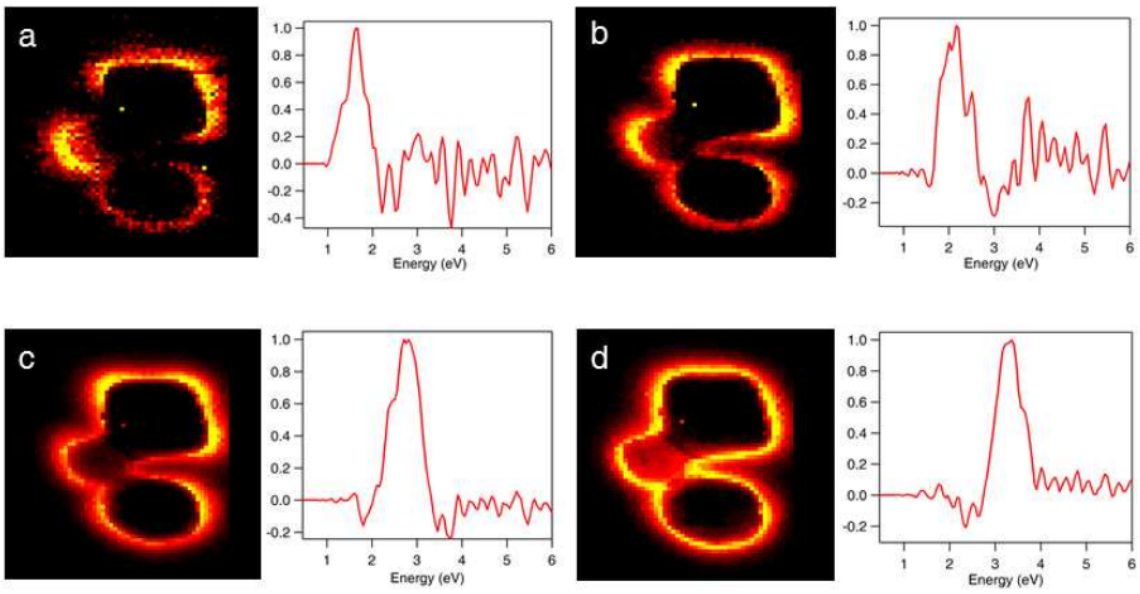

Figure 3.10: Plasmon maps and loading spectra of SMSERS active nanostructures using AXSIA. Multivariate statistical analysis (MVSA) employing the AXSIA program, was applied to the data to extract statistically significant component spectra and maps.

Chapter 4

A Combined Tight-Binding and Numerical Electrodynamics Understanding of the STEM/EELS Magneto-Optical Responses of Aromatic Plasmon-Supporting Metal Oligomers

This work has previously been published in the following article:

C. Cherqui[#], N. W. Bigelow[#], A. Vaschillo, H. Goldwyn, and D. J. Masiello.

ACS Photonics **1**, 1013 (2014)

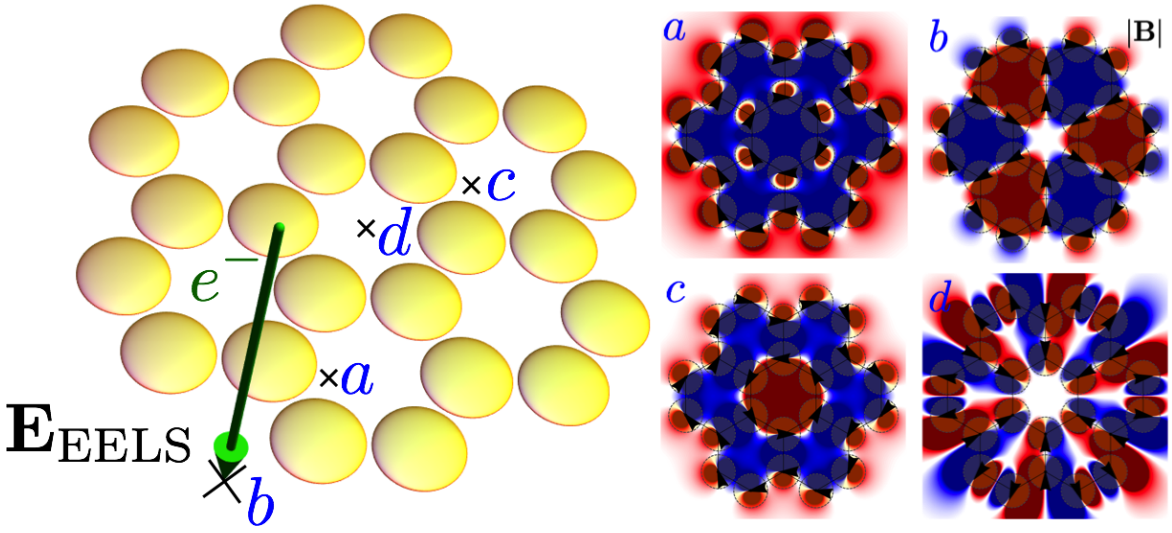

Figure 4.1: Abstract figure.

4.1 Abstract

The optical-frequency magnetic and electric properties of cyclic aromatic plasmon-supporting metal nanoparticle oligomers are explored through a combination of scanning transmission electron microscopy (STEM)/electron energy-loss spectroscopy (EELS) simulation and first-principles theory. A tight-binding type model is introduced to explore the rich hybridization physics in these plasmonic systems and tested with full-wave numerical electrodynamics simulations of the STEM electron probe. Building from a microscopic electric model, connection

is made at the macroscopic level between the hybridization of localized magnetic moments into delocalized magnetic plasmons of controllable magnetic order and the mixing of atomic p_z orbitals into delocalized π molecular orbitals of varying nodal structure spanning the molecule. It is found that the STEM electrons are uniquely capable of exciting all of the different hybridized eigenmodes of the nanoparticle assembly—including multipolar closed-loop ferromagnetic and antiferromagnetic plasmons, giant electric dipole resonances, and radial breathing modes—by raster scanning the beam to the appropriate position. Comparison to plane wave light scattering and cathodoluminescence (CL) spectroscopy is made. The presented work provides a unified understanding of the complete plasmon eigenstructure of such oligomer systems as well as of the excitation conditions necessary to probe each mode.

4.2 Introduction

The magnetic permeability of the coinage metals is nearly that of vacuum in the visible part of the electromagnetic spectrum. However, when a localized surface plasmon resonance is excited on a metal nanoparticle, its electron density oscillation induces a small local magnetic field that is 90 degrees out of phase from its electric field. In spite of the relative weakness of this magnetic field, in 2005 Alù and Engheta [138] predicted that a sizable effective magnetic resonance could be generated within a collection of metal nanoparticles arranged on the corners of a rigid polygon due to the collective electric polarization of each particle [63–65]. This collective mode may hybridize in the "bonding" configuration (i.e., as electric dipoles organized head-to-tail around the polygon ring in a closed loop) to mimic a split-ring resonator [139] with multiple splits. When the system is driven resonantly at the frequency

of its lowest lying eigenmode with either far-field plane wave radiation [140, 141] or in the near-field with an electric or magnetic dipole [142, 143], a polarization current is set up that oscillates back and forth on each constituent nanoparticle. All together the nanoparticles conspire to localize their weak intrinsic magnetic fields constructively toward the ring center. This collective magnetic resonance has an effective magnetic moment—a so-called *magnetic plasmon*—that oscillates between north (counterclockwise) and south (clockwise) at optical frequencies. Assemblies of nanoparticles that support magnetic plasmon modes are defined to be magnetic metamaterials, meaning that they possess anomalous magnetic properties beyond that of ordinary metals.

As multiple nanoparticle-based polygon assemblies are fused together into extended metal oligomers, the magnetic plasmon resonances of each ring unit cell mix and hybridize [144–146] just as electric plasmon resonances do [147], forming new delocalized magnetic plasmons of varying magnetic character and nodal order. Evidence of this hybridization has already been predicted in near-linear chains of fused nanoparticle rings [142, 143], where the long-range propagation and interference of the maximally nodal antiferromagnetic plasmon was demonstrated. The existence of magnetic plasmon modes has also been demonstrated in metallodielectric nanoclusters [148], where certain magnetic plasmon modes were transmuted to new ones through the addition of dielectric nanoparticles. Beyond the fundamental magnetic plasmon resonances described in these papers, the theory of plasmon hybridization further dictates the existence of delocalized plasmon resonances of varying magnetic and electric character and multipolar order. However, to date no systematic and unifying first-principles understanding of the complete hybridized plasmon eigenstructure of such oligomer

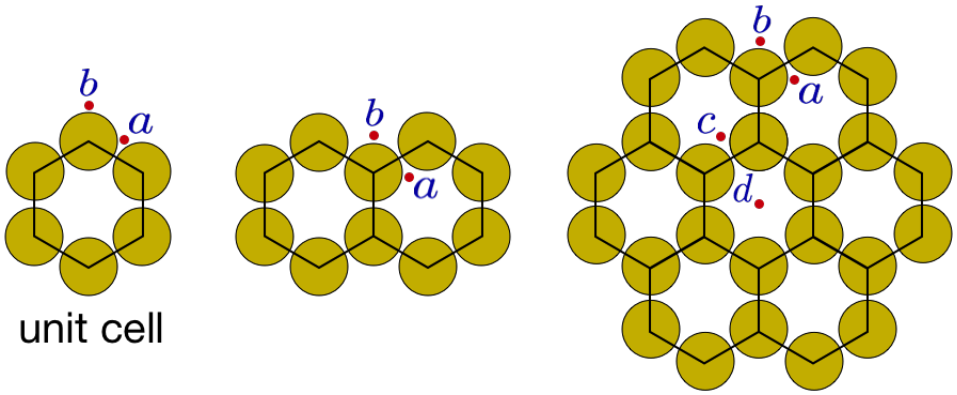

Figure 4.2: Planar cyclic assemblies of metal nanoparticles—so-called metal *oligomers*—arranged into a 1-mer (left), 2-mer (middle), and 6-mer (right), mimicking the aromatic molecules benzene, naphthalene, and coronene. Each system is constructed from the same hexagonal unit cell depicted in the left image. When resonantly driven at frequencies near the electric dipole plasmon resonance of an individual nanoparticle, the N-mer exhibits collective plasmon resonances of both electric and magnetic character that are delocalized across the entire assembly. The magnetic plasmon resonances of these N-mer systems are especially interesting as they support optical frequency magnetic moments of antiferromagnetic or ferromagnetic character of varying nodal order, all of which may be controllably excited by the electron beam of a STEM and detected in EELS. The particular aloof beam positions labeled a, b, c, and d (and their symmetric equivalents) will be investigated in the following.

systems of arbitrary morphology has appeared in the literature. Nonetheless, magnetic plasmons have recently been the focus of intense interest [66, 141–146, 148–176] due to their potential application in the design of metamaterials. The exploration of Fano effects based on the interference between magnetic and electric plasmon resonances has also attracted considerable investigation recently [141, 149, 177]. Beyond this literature, particular attention should be given to the work of van Aken and co-workers on the detection of toroidal modes in plasmonic nanocavities using energy-filtered transmission electron microscopy [178, 179]. Babinet's principle dictates how the surface plasmon modes of an array of nanocavities are related to an array of nanoparticles of the same shape. Yet, this analogy has yet to be explored for these nanocavity arrays and the exotic magnetic resonances that they support. It is a main purpose of this paper to construct a complete picture of both magnetic and

electric plasmon hybridization across a family of experimentally accessible cyclic aromatic oligomer systems of arbitrary morphology and metallic composition. To illustrate the formalism in detail, we focus on the particular structures displayed in 4.2. The geometries under consideration are composed of planar cyclic assemblies of metal nanoparticles arranged to mimic certain aromatic molecules [180]. This similarity allows us to exploit a corresponding microscopic electric and macroscopic magnetic tight-binding model. The tight-binding model for aromatic molecules is known as Hückel theory and is mathematically equivalent to the model of magnetic plasmon hybridization used in this paper [181]. Using these models, we find that such structures support a progression of hybridized multipolar magnetic plasmons of varying ferromagnetic and antiferromagnetic character as well as multipolar electric plasmons of giant dipole and radial breathing character. We further demonstrate through simulation that these hybridized plasmons can be individually excited by a scanning transmission electron microscope (STEM) and identified in electron energy-loss spectroscopy (EELS) and cathodoluminescence (CL) experiments. Such experiments are simulated with the full-wave electron-driven discrete-dipole approximation (e-DDA) code, which numerically solves for the electrodynamics of a swift ion and its interaction with nearby metal surfaces [11, 92, 182–184]. The results are found to be in excellent agreement with those stemming from the tight-binding analysis.

The work presented here differs from previous studies of magnetic plasmons in several ways: earlier studies have focused on a few of the modes possible in single ring systems [64, 138, 149] and in near-linear chains of coupled systems [143]. However, excitation of the complete eigenspectrum of collective magnetic and electric plasmon modes in aromatic nanoparticle

oligomers by a STEM electron beam has not been explored previously. Consequently, their complete hybridization structure has not been fully appreciated. Larger and more extended systems exhibit even richer magnetic properties that could be useful in the development of magneto-inductive wave guides [185, 186] and metamaterials [187–190]. The keV electrons generated within the STEM possess a high degree of spatial localization due to their sub-Ångstrom de Broglie wavelength, allowing one to specifically control the spatial location where energy is deposited into the system. This provides a mechanism for the systematic excitation of the entire plasmon eigenspectrum, which cannot be achieved with plane wave excitation. It is the purpose of this paper to elucidate these diverse and controllable properties of extended cyclic magnetic-plasmon supporting nanostructures using analytic theory combined with STEM/EELS simulations.

4.3 Tight-binding models of interacting localized surface plasmon resonances

4.3.1 Electric tight-binding model

To model the electric plasmon resonances occuring in cyclic metal nanoparticle assemblies such as those displayed in 4.2 we follow the coupled oscillator formalism of Lucas and co-workers [191]. This model treats the electric dipole response induced in the ith nanoparticle as a fictitious surface plasmon oscillator of mass m_{sp} and dipole moment $\mathbf{p}_i(\omega) \equiv \mathbf{p}(\mathbf{R}_i, \omega) = \boldsymbol{\alpha}(\omega) \cdot \mathbf{E}(\mathbf{R}_i, \omega)$ and is equivalent to the well-known hybridization theory [147] in the dipole limit. Particles located at positions $\mathbf{R}_i$ and $\mathbf{R}_j$ are coupled through their

mutual electric dipole-electric dipole interaction, $-\mathbf{p}_i(t)\mathbf{\Lambda}^0_{ij}\mathbf{p}_j(t)$, where $\mathbf{\Lambda}^0_{ij} \equiv \mathbf{\Lambda}^0(\mathbf{R}_i, \mathbf{R}_j) = [3\hat{\mathbf{n}}_{ij}\hat{\mathbf{n}}_{ij} - \mathbf{1}_{ij}]/|\mathbf{R}_i - \mathbf{R}_j|^3$ is the near-field component of the standard electric dipole relay tensor evaluated in the quasi-static limit ($kd \ll 1$) and $\hat{\mathbf{n}}_{ij} \equiv (\mathbf{R}_i - \mathbf{R}_j)/|\mathbf{R}_i - \mathbf{R}_j|$. In the case where each particle is an isotropic metal nanosphere of radius d then its linear polarizability may be decomposed into the sum of two terms,

$$\boldsymbol{\alpha}(\omega) = \boldsymbol{\alpha}_C + \boldsymbol{\alpha}_{\rm sp}\frac{\omega^2_{\rm sp}}{\omega(\omega + i\gamma) - \omega^2_{\rm sp}}, \tag{4.1}$$

the first corresponding to the ionic core response and the second to the response of the electron gas confined to the surface of a sphere, giving it a resonant frequency of $\omega_{\rm sp} = \Omega_{\rm pl}/\sqrt{\epsilon_\infty + 2}$ in terms of the plasma frequency $\Omega_{\rm pl}$, a bulk dephasing rate of γ, and an infinite frequency relative permittivity ε_∞. Here, $\boldsymbol{\alpha}_C = d^3\mathbf{1}(\varepsilon_\infty - 1)/(\varepsilon_\infty + 2)$ and $\boldsymbol{\alpha}_{\rm sp} = 3d^3\mathbf{1}/(\varepsilon_\infty + 2)$ are based upon the Drude model $\epsilon(\omega) = \epsilon_\infty - \Omega^2_{\rm pl}/\omega(\omega + i\gamma)$ for the electronic response of the metal.

If we ignore the polarization of the core we find that the time evolution of the dipole moment of the surface conduction electrons induced by an electric field $\mathbf{E}$ is described by

$$\mathbf{p}(\mathbf{R}, t) = \boldsymbol{\alpha}_{\rm sp}\omega^2_{\rm sp}\int_{-\infty}^{t} dt' \frac{\sin\sqrt{\omega^2_{\rm sp} - (\gamma/2)^2}(t - t')}{\sqrt{\omega^2_{\rm sp} - (\gamma/2)^2}} e^{-\gamma(t-t')/2}\mathbf{E}(\mathbf{R}, t'), \tag{4.2}$$

which is the solution of the damped and driven harmonic oscillator $\ddot{\mathbf{p}}(\mathbf{R}, t) + \gamma\dot{\mathbf{p}}(\mathbf{R}, t) + \omega^2_{\rm sp}\mathbf{p}(\mathbf{R}, t) = (-e/m_{\rm sp})\mathbf{E}(\mathbf{R}, t)$. Neglecting damping, this equation can be derived from the

classical Hamiltonian

$$H_0 = \frac{\wp^2}{2m_{\mathrm{sp}}} + \frac{1}{2}m_{\mathrm{sp}}\omega_{\mathrm{sp}}^2\mathbf{u}^2 - (-e)\mathbf{u}\cdot\mathbf{E} \tag{4.3}$$

expressed in terms of its generalized coordinates for the displacement $\mathbf{u} = \mathbf{p}/(-e)$ and momentum $\wp$ of the fictitious plasmon oscillator of mass $m_{\mathrm{sp}} = e^2/\alpha_{\mathrm{sp}}\omega_{\mathrm{sp}}^2$, where α_{sp} is defined according to $\boldsymbol{\alpha}_{\mathrm{sp}} = \alpha_{\mathrm{sp}}\mathbf{1}$. Extension of 4.3 to an assembly of n metal nanoparticles interacting pairwise through the electric dipole-electric dipole potential energy $-\mathbf{p}_i(\omega)\boldsymbol{\Lambda}_{ij}^0\mathbf{p}_j(\omega)$ results in the total Hamiltonian

$$H = \sum_i \left[\frac{\wp_i^2}{2m_{\mathrm{sp}}} + \frac{1}{2}m_{\mathrm{sp}}\omega_{\mathrm{sp}}^2\mathbf{u}_i^2\right] - \frac{e^2}{2}\sum_{ij}\mathbf{u}_i\cdot\boldsymbol{\Lambda}_{ij}^0\cdot\mathbf{u}_j, \tag{4.4}$$

where the electric field appearing in H_0 is here generated by the $n-1$ other nanoparticles according to $\mathbf{E}(\mathbf{R}_i,t) = \sum_{j\neq i}\boldsymbol{\Lambda}_{ij}^0(-e)\mathbf{u}_j(t)$. The first term in brackets is the sum of kinetic and potential energies for the localized surface plasmon resonance on each particle. The second term is the interaction energy of the ith plasmon with the electric field produced by the jth plasmon.

It is convenient to recast 4.4 in terms of the dimensionless variables $\mathbf{Q}_i(t) = \sqrt{m_{\mathrm{sp}}\omega_{\mathrm{sp}}/\hbar}\mathbf{u}_i(t)$ and $\boldsymbol{\Pi}_i(t) = \wp_i(t)/\sqrt{\hbar m_{\mathrm{sp}}\omega_{\mathrm{sp}}}$ yielding

$$\frac{H}{\hbar\omega_{\rm sp}} = \frac{1}{2}\sum_i [\mathbf{\Pi}_i^2 + \mathbf{Q}_i^2] - \frac{1}{2}\sum_{ij} g_{ij}\left[3\mathbf{Q}_i\cdot\hat{\mathbf{n}}_{ij}\hat{\mathbf{n}}_{ij}\cdot\mathbf{Q}_j - \mathbf{Q}_i\cdot\mathbf{Q}_j\right] \tag{4.5}$$

with the dimensionless coupling constant $g_{ij} = \alpha_{\rm sp}/d^3 r_{ij}^3 = (1/r_{ij}^3)(3/[\epsilon_\infty + 2])$ and dimensionless distance between nanoparticles, $r_{ij} = |\mathbf{R}_i - \mathbf{R}_j|/d$. Restricting the nanoparticles to lie within a common plane and further restricting to nearest neighbor interactions removes the ij-dependence from r and g when the nanoparticles are positioned at the vertices of a regular polygon, such as is the case of the three N-mer assemblies displayed in 4.2. This has the effect of simplifying the Hamiltonian even further by removing a direction of space (i.e. the direction normal to the plane) and simplifying the coupling constants. A route to quantization of the surface plasmon is now apparent by promoting the dynamical variables in 4.5 to operators and imposing upon them the commutation relations associated with boson statistics [192, 193]. Interestingly, the coupling constant g is independent of the sphere radius and only depends on the ratio of the distance between the particles to their radius. This lack of dependence on the sphere radius is to be expected given that the quasi-static approximation is built into our tight-binding model. Furthermore, since the dipole that represents the response of a nanosphere is located at the sphere center, there is a minimum value for r and in the limit that two spheres touch g has a maximum of $(1/2^3)(3/[\epsilon_\infty + 2]) \neq \infty$.

It should be noted that this model neglects all quantum effects due to electron wave function spill out, electron tunneling between metal nanoparticles, and the discretization of energy levels as the particles becomes small enough to be classified as metal clusters. Such effects are important for nanoparticles separated at distances less than ~ 0.5 nm or for radii of

only a few nanometers, imposing a lower bound on the validity of our model. Despite these limitations, it provides a reliable description of the energy eigenspectrum for the hybridized plasmon responses occuring within the N-mer nanoparticle assemblies discussed in this paper.

Diagonalization of the Hamiltonian in 4.5 for the planar 1-mer unit cell composed of six nanoparticles (see 4.2, left panel) yields a set of 12 hybridized plasmon eigenmodes, $\{\mathbf{p}_i(t)\}_\nu$, labeled by $\nu = 1, \ldots, 12$. The spatial dependence of the magnetic field magnitude $|\mathbf{B}_\nu|$ associated with each through the curl of the vector potential $\mathbf{A}_\nu(\mathbf{x}, t) = \sum_{i=1}^{6}(-ik)\mathbf{p}_i^\nu(t)\exp(ik|\mathbf{x} - \mathbf{R}_i|)/|\mathbf{x} - \mathbf{R}_i|$ is displayed in 4.3; here $k = \omega/c$ is the wave vector of light. The ground state is characterized as having electric dipole moments oriented tangent to the circle circumscribing the hexagon on which they lie. This head-to-tail or closed-loop arrangement of the dipoles allows for the concentration of the individual magnetic fields produced by each sphere toward the center of the unit cell, leading to a non-trivial focusing of the magnetic field into a *magnetic hot spot* with an effective magnetic moment. This is a well known result, first proposed in 2005 by Alù and Engheta [138] and is similar to how a split ring resonator operates.

When a collection of N unit cells is arranged into an N-mer, such as the 2-mer and 6-mer displayed in 4.2, the spectrum of the Hamiltonian in 4.5 contains an even greater diversity of eigenmodes. Magnetic plasmons that are hybridizations of the effective magnetic moments of each unit cell arise as do fundamentally different plasmons of giant electric dipole and radial breathing character, among many others. 4.4 and 4.5 display the magnetic field magnitude, $|\mathbf{B}|$, corresponding to five eigenmodes of the 2-mer and the lowest lying nine eigenmodes of

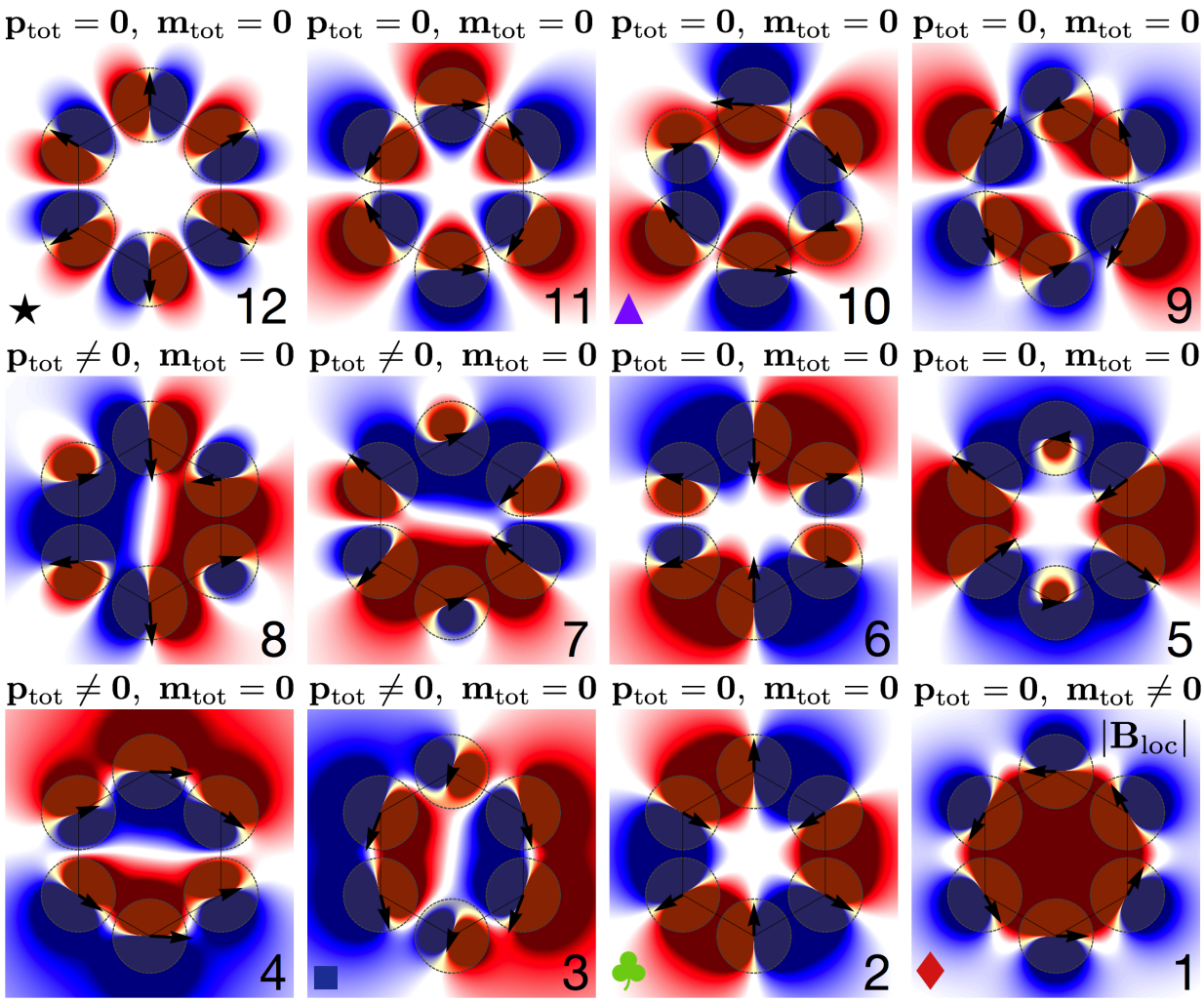

Figure 4.3: $|\mathbf{B}_{\rm loc}|$ associated with each of the 12 tight-binding model eigenmodes of the 1-mer unit cell arranged in increasing energy order, labeled by $\nu = 1, \ldots, 12$. Red (blue) represents a north (south) oriented magnetic dipole, while white represents the absence of a magnetic moment. The black arrows in each panel depict the electric dipole moments of the corresponding eigenmode. Circles are overlaid upon each dipole to indicate the locations of the underlying nanoparticles, although the latter are not explicitly included in the tight-binding model. The dipole moments of the ground state ($\nu = 1$) form a closed loop and act to localize their magnetic field into the center of the unit cell. They present no net electric dipole moment but they collectively generate an effective magnetic moment. The latter is called a magnetic plasmon resonance [64, 138]. In addition there are eigenmodes that correspond to giant electric dipoles ($\nu = 3, 4$) and even a radial breathing mode ($\nu = 12$). Depending on the location of the STEM electron beam, each one of these features can be controllably excited and detected in EELS. The symbols appearing in each panel correspond to certain spectral positions in 4.6. The net electric and magnetic moments $\mathbf{p}_{\rm tot}$ and $\mathbf{m}_{\rm tot}$ are overlaid above each eigenmode.

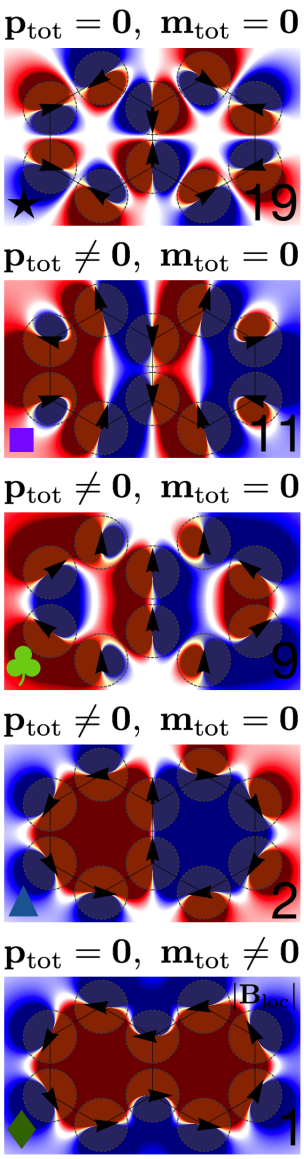

Figure 4.4: $|\mathbf{B}_{\rm loc}|$ associated with five of the tight-binding model eigenmodes of the 2-mer arranged in increasing energy order, labeled by $\nu = 1, 2, 9, 11, 19$. 15 other eigenmodes also appear in the spectrum, which we do not display. With only two units cells, the 2-mer possesses only two hybridized magnetic plasmons. The ground state ($\nu = 1$) is ferromagnetic in character with the magnetic moments on each unit cell pointing in the same direction. The opposite is true for the first excited state ($\nu = 2$) which is antiferromagnetic in character. A giant electric dipole plasmon ($\nu = 9$) also appears in the spectrum. Depending on the location of the STEM electron beam, each one of these features can be controllably excited and detected in EELS. The symbols appearing in each panel correspond to certain spectral positions in 4.7. The net electric and magnetic moments $\mathbf{p}_{\rm tot}$ and $\mathbf{m}_{\rm tot}$ are overlaid above each eigenmode. Those eigenmodes of closed-loop magnetic character having $\mathbf{m}_{\rm tot} = \mathbf{0}$ are antiferromagnetic, while those with $\mathbf{m}_{\rm tot} \neq \mathbf{0}$ are ferromagnetic.

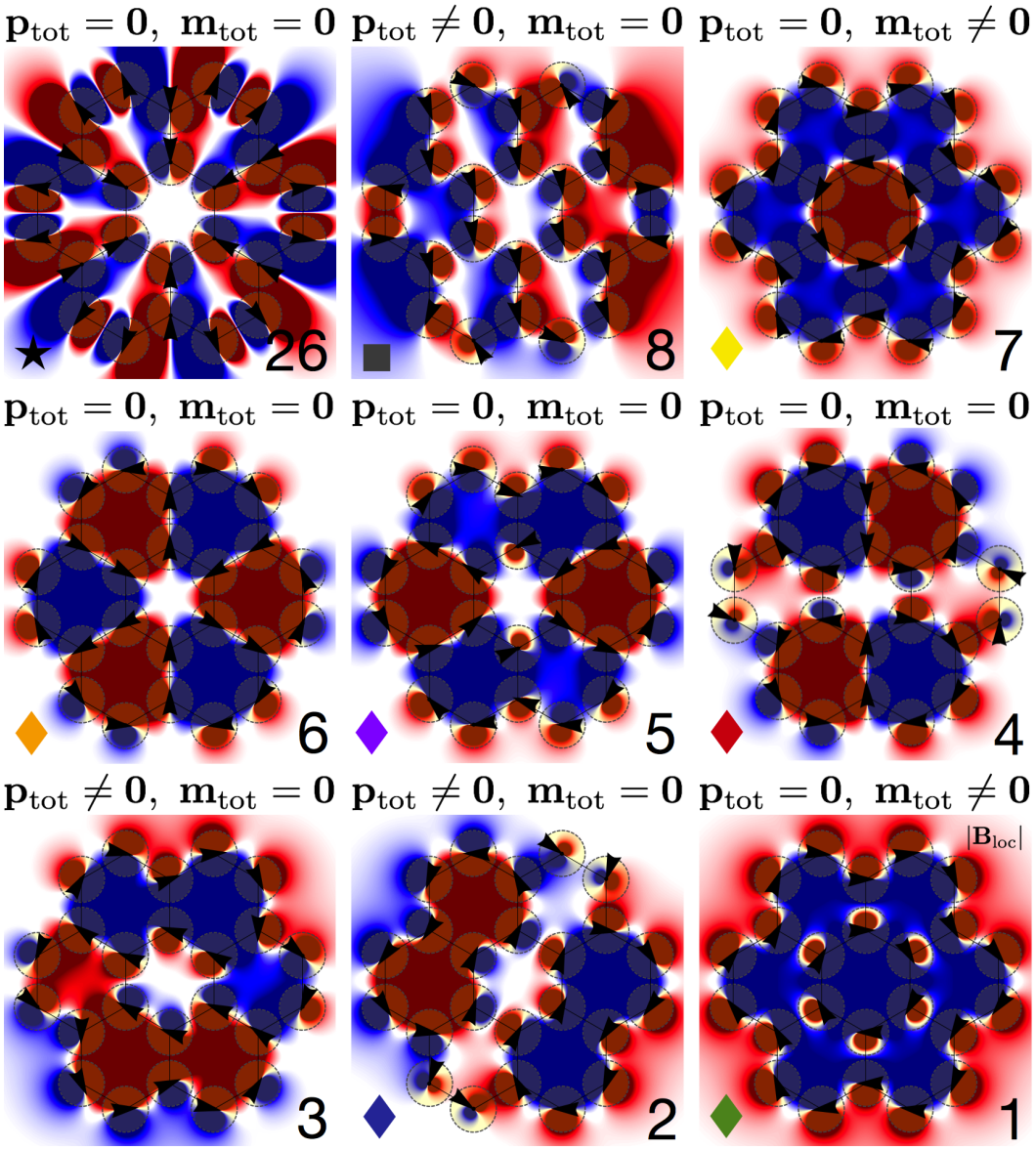

Figure 4.5: $|\mathbf{B}_{\rm loc}|$ associated with nine of the tight-binding model eigenmodes of the 6-mer arranged in increasing energy order, labeled by $\nu = 1, \ldots, 8, 26$. 39 additional eigenmodes also appear in the spectrum, which we do not display. With six units cells, the 6-mer possesses seven hybridized magnetic plasmons. The ground state ($\nu = 1$) is ferromagnetic in character with the magnetic moments on each unit cell pointing in the same direction. Beyond this appears a multipolar progression of hybridized magnetic plasmons ($\nu = 2 - 6$) of antiferromagnetic character and increasing angular nodal order. The ground state taken together with the ferromagnetic excited state with one radial node ($\nu = 7$) bookend this collection of antiferromagnetic modes. A giant electric dipole ($\nu = 8$) and giant radial breathing mode ($\nu = 26$) also exist above all magnetic eigenmodes. The STEM electron beam can access each of these modes by raster scanning to the appropriate position. The symbols appearing in each panel correspond to certain spectral positions in 4.8. The net electric and magnetic moments $\mathbf{p}_{\rm tot}$ and $\mathbf{m}_{\rm tot}$ are overlaid above each eigenmode. Those eigenmodes of closed-loop magnetic character having $\mathbf{m}_{\rm tot} = \mathbf{0}$ are antiferromagnetic, while those with $\mathbf{m}_{\rm tot} \neq \mathbf{0}$ are ferromagnetic.

the 6-mer, computed from H in 4.5; the 2-mer has 20 and the 6-mer has 48 total hybridized eigenmodes. Some of the general features exposed by this model are:

1. All ferromagnetic plasmon modes contain a net zero electric dipole moment and a net nonzero magnetic dipole moment.

2. The hybridized plasmon eigenenergies split with respect to the electric dipole response, $\hbar\omega_{\mathrm{sp}}$, of a single nanoparticle, with the closed-loop magnetic modes all lying at the bottom, bounded from above by the collective giant dipole modes. All hybridized plasmon resonances of either electric or magnetic character reduce to that of the single nanoparticle's dipole plasmon in the limit where $g \to 0$.

3. The dynamics of the system is governed by nearest neighbor interactions, meaning that the local environment of each nanoparticle dominates the energetics of the collective assembly. Since all magnetic plasmon modes are composed of electric dipoles on adjacent particles oriented in a head-to-tail arrangement, they are all nearly energetically degenerate. This means that choosing an excitation source with the right spectral and more importantly spatial behavior will be important when trying to excite a particular magnetic plasmon.

It is important to point out that because the electric Hamiltonian (4.5) was derived within the quasi-static limit, it does not account for the total energy of the system whenever a non-trivial amount of energy is contained within the magnetic field. But this is precisely the case for all of the closed-loop magnetic modes of the N-mer. The consequences of this shortcoming are that the energy ordering of the magnetic modes among themselves is incorrect. For example, in the case of the 2-mer, the antiferromagnetic plasmon (mode 2 in 4.4)

is predicted to have a lower energy than the ferromagnetic plasmon (mode 1 in 4.4). However, as will be shown in the following, full-wave electrodynamics simulations reveal that the ferromagnetic mode is the ground state and the antiferromagnetic mode is the first excited state of the 2-mer. This inverse ordering should be expected if one adopts a circuit model in which in-phase current loops form the lowest energy configuration of the system [145, 194]. Interestingly, while the specific energy ordering of the magnetic modes is incorrectly predicted by H, the specific polarization of individual nanoparticles for any given magnetic mode is nearly exactly predicted by the electric tight-binding formalism. This is the case for all N-mer systems. This breakdown in the model marks a transition from a system whose energetics are electrically dominated to a system where both electric and magnetic effects are important. To resolve this issue, several options exist, the most rigorous of which is to solve Maxwell's equations, which we do in the following. Another approach is to coarse grain the N-mer into a collection of interacting magnetic moments, parametrized by their underlying electric interactions. The details of the latter will now be described.

4.3.2 Magnetic tight-binding model

As kd becomes smaller, the electric near-field extends to infinity and the magnetic field becomes negligible. It is, therefore, not surprising that the previous quasi-static electric tight-binding Hamiltonian is incomplete in its description of systems that store energy in the magnetic field. The metal oligomers under investigation in this paper are examples of systems where magnetic effects can be important. To properly understand their magnetic

eigenmode structure we will to use the unique magnetic plasmon mode of the 1-mer to construct a coarse-grained magnetic tight-binding Hamiltonian.

The magnetic moment of the 1-mer unit cell's ground state may be well described as a magnetic dipole when the size of the unit cell is small in comparison to the wavelength of an interrogating photon of energy $\hbar\omega$. Even when this is not true, the dipole moment of a multipolar distribution of charge and current often describes the physics qualitatively correctly. Neglecting damping, the magnetic dipole moment $\mathbf{m}$ associated with a collection of n electric dipoles $\mathbf{p}_i$ arranged in a closed loop with current density $\mathbf{J}(\mathbf{x},t) = \sum_i \dot{\mathbf{p}}_i(t)\delta(\mathbf{x}-\mathbf{R}_i)$ is

$$\mathbf{m}(\mathbf{R}=\mathbf{0},t) = \frac{1}{2c}\int \mathbf{x}\times\mathbf{J}(\mathbf{x},t)d^3x = \frac{n\omega_M pR}{2c}\cos(\omega_M t)\,\hat{\mathbf{e}}_z, \tag{4.6}$$

where $\mathbf{R}=\mathbf{0}$ is the location of the center of the unit cell, $\hbar\omega_M = \hbar\omega_{\mathrm{sp}}\sqrt{(1-7g)/2}$ is the ground state energy eigenvalue of 4.5, and $|\mathbf{R}_i| \equiv R$ and $|\mathbf{p}_i| \equiv p$ for $1 \leq i \leq n$. This magnetic dipole oscillates periodically in time at frequency ω_M and is characterized by the magnetic polarizability

$$\boldsymbol{\alpha}_M(\omega) = \boldsymbol{\alpha}_{\mathrm{msp}}\frac{\omega_M^2}{\omega(\omega+i\gamma_M)-\omega_M^2}, \tag{4.7}$$

where $|\boldsymbol{\alpha}_{\mathrm{msp}}| \equiv \alpha_{\mathrm{msp}} = n\alpha_{\mathrm{sp}}/2$ and has a component only in the zz-direction. In this way, by excising all higher order eigenmodes from the eigenspectrum, the 1-mer unit cell is

coarse-grained by $\mathbf{m}$.

In an analogy to the procedure leading to 4.3, a tight-binding Hamiltonian for the unit cell can be defined that dictates the behavior of the single magnetic dipole $\mathbf{m}$ in a magnetic field $\mathbf{B}$. For a collection of N unit cells such as the 2-mer and 6-mer structures displayed in 4.2, the effective magnetic dipole localized within each ring unit will hybridize with those on neighboring units through mutual magnetic dipole-magnetic dipole interactions of the form $-\mathbf{m}_i(t)\mathbf{\Lambda}^0_{ij}\mathbf{m}_j(t)$, where $\mathbf{m}_i(\omega) \equiv \mathbf{m}(\mathbf{X}_i, \omega) = \boldsymbol{\alpha}_M(\omega) \cdot \mathbf{B}(\mathbf{X}_i, \omega)$. Restricting to nearest neighbors leads to the following dimensionless coarse-grained Hamiltonian for the N-mer

$$\frac{H_M}{\hbar\omega_M} = \frac{1}{2}\sum_i [\pi_i^2 + q_i^2] - \frac{g_M}{2}\sum_{ij}{}' q_i q_j \tag{4.8}$$

in an analogy to 4.5, where the magnetic and electric coupling constants are connected by $g_M = g/n$ and where the prime on the sum denotes nearest neighbors. The symmetry of the system makes g_M the same for all i, j. Here $q_i(t) = \sqrt{m_{\mathrm{msp}}\omega_{\mathrm{msp}}/\hbar}|\mathbf{m}_i(t)|/(-e)$ and $\pi_i(t) = m_{\mathrm{msp}}(|\dot{\mathbf{m}}_i(t)|/(-e))/\sqrt{\hbar m_{\mathrm{msp}}\omega_{\mathrm{msp}}}$ are the generalized dimensionless coordinates and momenta of a fictitious magnetic plasmon oscillator of mass $m_{\mathrm{msp}} = e^2/\alpha_{\mathrm{msp}}\omega^2_{\mathrm{msp}}$.

This is the magnetic plasmon equivalent of the Hückel Hamiltonian used in the description of the molecular orbitals of aromatic molecules. As the p_z atomic orbitals of an aromatic molecule hybridize into π molecular orbitals of varying nodal structure, so too do the magnetic dipole moments on each unit cell hybridize into collective magnetic plasmons that can

be classified as ferromagnetic or antiferromagnetic in character. Like the Hückel Hamiltonian, which contains the coupling constants α and β expressing the strengths of the on-site and nearest neighbor interactions and which may be computed by accounting for the microscopic Coulombic interactions between electrons in the atomic orbitals, H_M contains coupling parameters that can be relayed back to the underlying microscopic physics of the electric dipole plasmons on each nanoparticle in the N-mer assembly. Once α_{sp} is known for a single particle then all magnetic properties contained within H_M can be determined for a given assembly.

Diagonalization of the coarse-grained magnetic Hamiltonian H_M in 4.8 leads to an eigenspectrum comprising the hybridized magnetic dipole moments of an arbitrary planar N-mer. Because they are good approximations to the closed-loop hybridized magnetic eigenmodes of H, we do not display the eigenmodes of H_M but instead use their corresponding eigenenergies to properly reorder the magnetic eigenmodes of H. 4.4 and 4.5 display the hybridized plasmon resonances of the 2-mer and 6-mer composed of the same basic 1-mer unit cell described in 4.2. The eigenmodes are computed from H in 4.5 and placed in order of their eigenenergies except for the closed-loop magnetic plasmons, which are reordered according to the corresponding eigenenergies of H_M. The 2-mer has only two hybridized magnetic plasmons; the ground state ($\nu = 1$) is ferromagnetic with the magnetic moments in each unit cell pointing in the same direction, while the opposite is true for the antiferromagnetic excited state ($\nu = 2$). The 6-mer possesses an even richer set of hybridized magnetic eigenmodes. The ground state and highest lying excited state ($\nu = 1$ and 7) are ferromagnets and bookend the magnetic part of the spectrum, while the five states in between ($\nu = 2 - 6$) are antiferromagnets of increasing nodal order. Effectively, we see a progression of modes that

go from having a single well-defined magnetic moment at the center of mass of the N-mer to a fully antiferromagnetic character. The lowest mode being that with a single magnetic moment representing in-phase polarization currents in all unit cells and the highest energy antiferromagnetic mode being that with maximally out-of-phase polarization currents. The ferromagnetic ground state ($\nu = 1$) possesses a finite magnetic moment as does the first ferromagnetic excited state ($\nu = 7$), while all antiferromagnetic modes have none. Because of this, the former modes are expected to have a signature in the system's CL response in addition to those modes supporting net electric dipole moments.

The analogy between this magnetic tight-binding model and Hückel theory is especially apparent in the eigenmodes of the 6-mer, with each 1-mer unit cell corresponding to a single carbon atom. However, there is one notable exception. Benzene has only six carbon atoms and six π molecular orbitals [195]. But the 6-mer has *seven* magnetic plasmon eigenmodes. Unlike in chemistry the central ring of the 6-mer behaves as a seventh unit cell (or as a seventh carbon atom). Because of this unique feature, the ferromagnetic modes 1 and 7 exist and have different energies. In fact there is no molecular analog to the $\nu = 7$ mode of the 6-mer. Interestingly, modes $1 - 6$ have the same degeneracy pattern as that of the Hückel description of benzene [195]. Full-wave electrodynamics simulation will also show this degeneracy pattern for all magnetic modes of the N-mer, although the magnitude of their splitting is quite small. The consequences of these facts will be discussed in the following.

4.4 Full-wave electrodynamics simulation and discussion

We now investigate the behavior of these systems with full-wave e-DDA numerical electrodynamics simulations. The previous formalism has predicted a rich and diverse set of oligomer eigenmodes, but it is not clear *a priori* how well they approximate the solutions of Maxwell's equations. Nor is it clear what the necessary excitation conditions are to drive each mode. It is the purpose of this investigation to resolve these open questions by considering both optical and electron-beam driving sources. The eigenmode polarizations dictated by the tight-binding model are of critical importance in this analysis as they will inform our choices of excitation source parameters such as the position of the electron beam relative to the target, thereby allowing us to drive specific modes of interest.

Rather than spheres we choose to employ nanodisks arranged on the corners of the hexagonal unit cell in 4.2. None of the physics described previously is affected by this change. Each nanodisk is composed of gold [101], has a 200 nm diameter, is 15 nm thick, and is separated by 225 nm (center to center) from the next adjacent particle in the lattice. For reference, the electric dipole plasmon of each individual nanodisk is located at 1.45 eV. All calculations employ a 100 keV electron beam to interrogate the system. Other nanoparticle shapes, sizes, separation distances, and material compositions that do not significantly differ from these parameters will only shift the collective plasmon resonances of the N-mer to other parts of the electromagnetic spectrum from the near UV through the visible to the near IR.

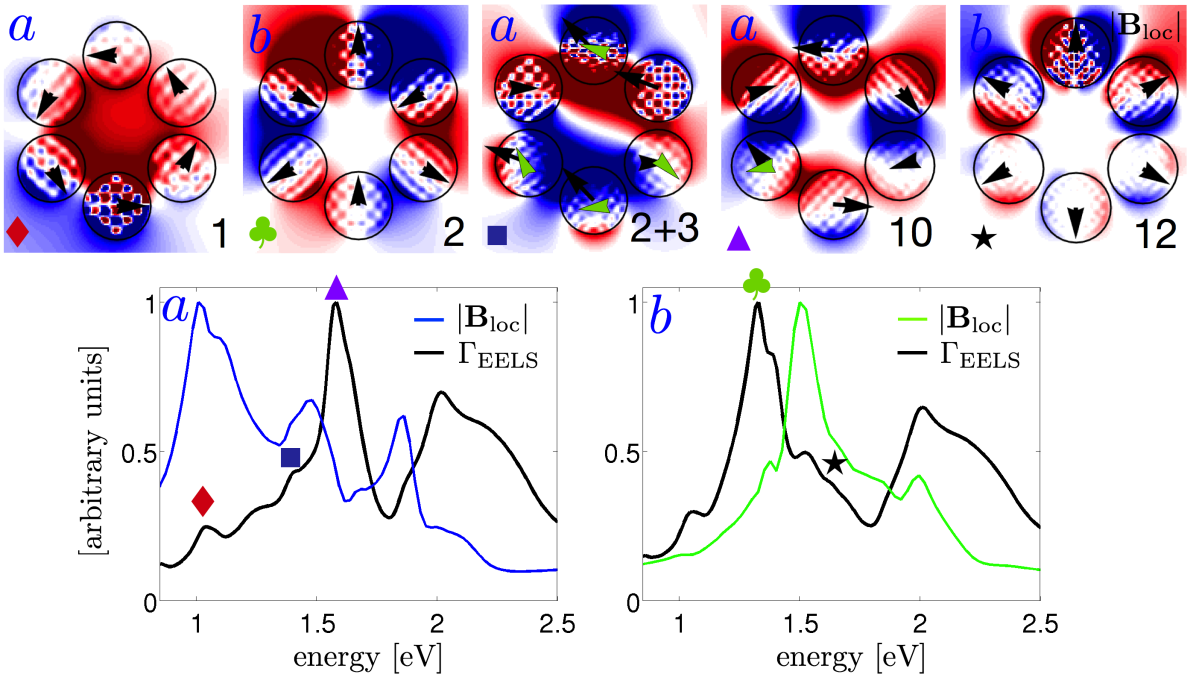

Figure 4.6: Normalized EEL probability Γ_{EELS} (black) and signed local magnetic field magnitude $|\mathbf{B}_{\mathrm{loc}}|$ (blue/green) spectra (lower panels) of the 1-mer unit cell composed of 200 nm diameter by 15 nm thick gold nanodisks separated by 225 nm from center to adjacent center. The electron beam is positioned at the aloof locations a and b denoted in the left panel of 4.2. All panels are computed from full-wave numerical electrodynamics simulations within the e-DDA. The spectrum of $|\mathbf{B}_{\mathrm{loc}}|$ is evaluated by integrating the locally induced magnetic field magnitude inside of the ring; red (blue) represents a north (south) oriented magnetic dipole, while white represents the absence of a magnetic moment. The upper panels display the spatial behavior of all of the energetically unique collective magnetic eigenmodes of the 1-mer that are excited at beam positions a and b. The corresponding electric tight-binding eigenmode, labeled by ν, is enumerated within each of the upper panels. The corresponding eigenmodes are overlaid as black arrows, with green arrows showing the deviation between model and simulation. Of particular importance is the ground state eigenmode (upper left panel), where the electric dipole moments (black arrows) on each disk conspire to generate a magnetic field localized within the ring (♦). Such an eigenmode is referred to as a magnetic plasmon resonance [64, 138]. Also shown is a primitive antiferromagnet (♣), a giant electric dipole (■), and a pair of high-lying excited states (▲ and ★), one of radial breathing character (★). Modes of quadrupolar character also exist in the spectrum above $\sim$ 1.7 eV (not explicitly shown), which are beyond the approximations built in to the presented tight-binding model.

We first examine the 1-mer unit cell. 4.6 displays the computed EEL probability Γ_{EELS} and local magnetic field magnitude $|\mathbf{B}_{\mathrm{loc}}|$ spectra of the 1-mer at the aloof beam positions a and b shown in 4.2. The electron-induced $|\mathbf{B}_{\mathrm{loc}}|$ is computed by integrating the locally induced magnetic field magnitude inside the ring. The spectral location of the closed-loop magnetic plasmon eigenmode can easily be gleaned by comparing the two spectra at position a. The upper panels show the spatial behavior of the $|\mathbf{B}_{\mathrm{loc}}|$ associated with five of the collective plasmon eigenmodes of the 1-mer, all of which are predicted from and are enumerated in accordance with the tight-binding eigenstates labeled by ν. The ground state of the 1-mer is a closed-loop magnetic plasmon resonance (♦). Beyond that lies a primitive antiferromagnetic plasmon (♣), a giant electric dipole plasmon (■), and two high-lying states, one of which has the character of a radial breathing mode (★). These states, which are all accessible by the STEM electron beam, represent the complete set of energetically unique magnetic eigenmodes of the 1-mer. Other collective eigenmodes of quadrupolar (or higher multipolar) character might also appear in an experiment, but are not part of the presented tight-binding model. It is of course possible to extend the model to include such higher order multipolar effects.

When two unit cells are brought together into a 2-mer the eigenmodes intrinsic to each rehybridize into an even richer set of eigenmodes spanning the dimer. 4.7 displays the computed EEL probability Γ_{EELS} and local magnetic field magnitude $|\mathbf{B}_{\mathrm{loc}}|$ spectra (lower panel) of the 2-mer at the aloof beam positions a and b shown in 4.2. The electron-induced $|\mathbf{B}_{\mathrm{loc}}|$ is computed by integrating the locally induced magnetic field magnitude within the closest ring unit adjacent to the electron beam. The upper panels show the spatial behavior of the

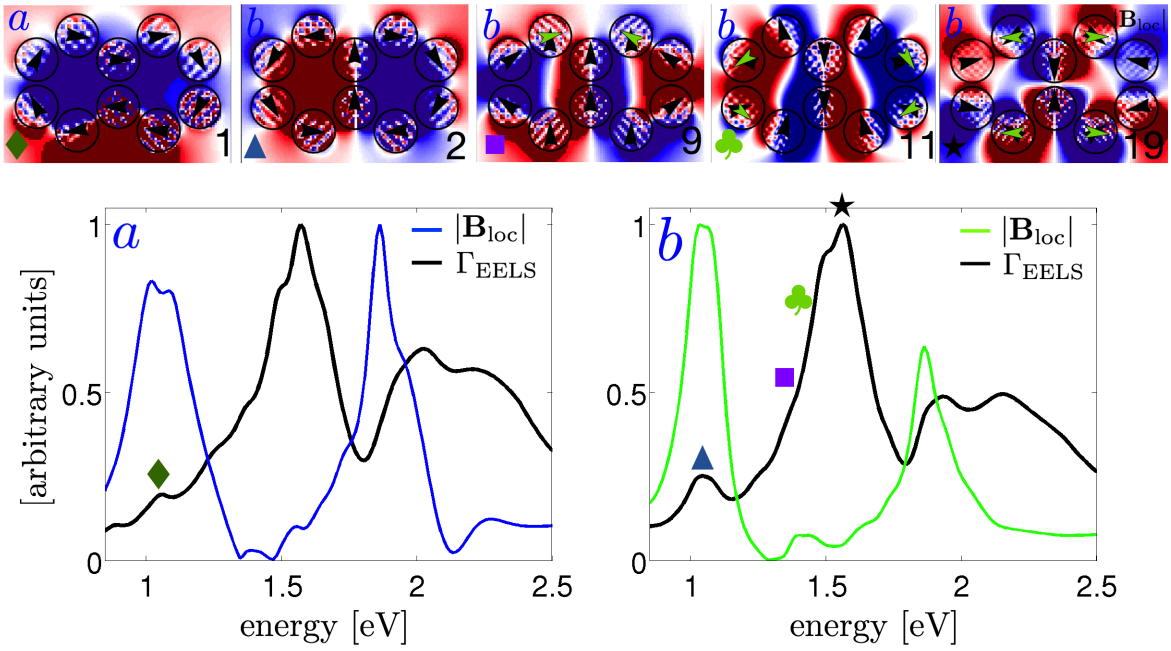

Figure 4.7: Normalized EEL probability Γ_{EELS} (black) and signed local magnetic field magnitude $|\mathbf{B}_{\mathrm{loc}}|$ (blue/green) spectra (lower panel) of the 2-mer computed within the e-DDA. The electron beam is positioned at the aloof locations a and b denoted in the middle panel of 4.2. The upper panels display the spatial behavior of a few of the 2-mer's collective eigenmodes that are excited at beam positions a and b. The corresponding tight-binding eigenmode is enumerated within each of the upper panels. Of particular importance is the ferromagnetic ground state (♦), where the magnetic moments in each unit cell point in the same direction. The first excited state is a closed-loop antiferromagnetic plasmon (▲), where the magnetic moments in each unit cell point in opposite directions. A giant electric dipole (■) and a radial breathing mode (★) also appear in the spectrum above both closed-loop magnetic plasmon modes.

$|\mathbf{B}_{\mathrm{loc}}|$ associated with five of the collective plasmon eigenmodes of the 2-mer, all of which are predicted from and are enumerated in accordance with the tight-binding eigenstates labeled by ν. The ground state of the 2-mer is a closed-loop magnetic plasmon resonance that is characterized by a colinear arrangement of the magnetic moments in each unit cell (♦). The first excited state, which is nearly degenerate with the previous, is also a closed-loop magnetic plasmon resonance, but has the magnetic moments in each unit cell pointing in opposite directions (▲). Together, they are the lowest energy ferromagnetic and antiferro-

magnetic plasmons of the 2-mer. Three other excited states of interest are identified, one of giant electric dipole character (♣) and the highest lying being an excited antiferromagnetic plasmon (★).

The hybridization patterns that occur in moving from the 1-mer to the 2-mer carry over to the 3-mer, 4-mer, and 5-mer (not shown) in a straightforward manner, independent of how the basic 1-mer unit cells within each are linked, i.e., either linearly or cyclically. Of particular note is the multipolar progression of magnetic plasmon resonances as the addition of another 1-mer introduces the possibility for another node in the magnetic plasmon density. However, a strikingly new behavior appears in the case where six 1-mers are arranged cyclically to form the 6-mer displayed in 4.2. In this geometry the 6-mer is a rescaled version of the 1-mer, where each nanoparticle of the 1-mer is replaced by the 1-mer unit cell itself. The two structures share the same point group. This means that the 1-mer and 6-mer partially share a similar collection of eigenmodes, but on different length scales. For example, the ferromagnetic ground state ($\nu = 1$) of the 1-mer and 6-mer are equivalent. The primitive antiferromagnetic first excited state ($\nu = 2$) of the 1-mer is equivalent to the maximally nodal antiferromagnetic excited state ($\nu = 6$) of the 6-mer. The two primitive giant electric dipoles ($\nu = 3, 4$) of the 1-mer are equivalent to the giant electric dipoles hybridized across the 6-mer ($\nu = 8, 9$). The radial breathing mode ($\nu = 12$) of the 1-mer is equivalent to the giant radial breathing mode of the 6-mer ($\nu = 26$; see 4.8), etc.

4.8 displays the computed EEL probability Γ_{EELS} and local magnetic field magnitude $|\mathbf{B}_{\mathrm{loc}}|$ spectra (lower panel) of the 6-mer at the aloof beam positions a, b, c, and d shown in 4.2.

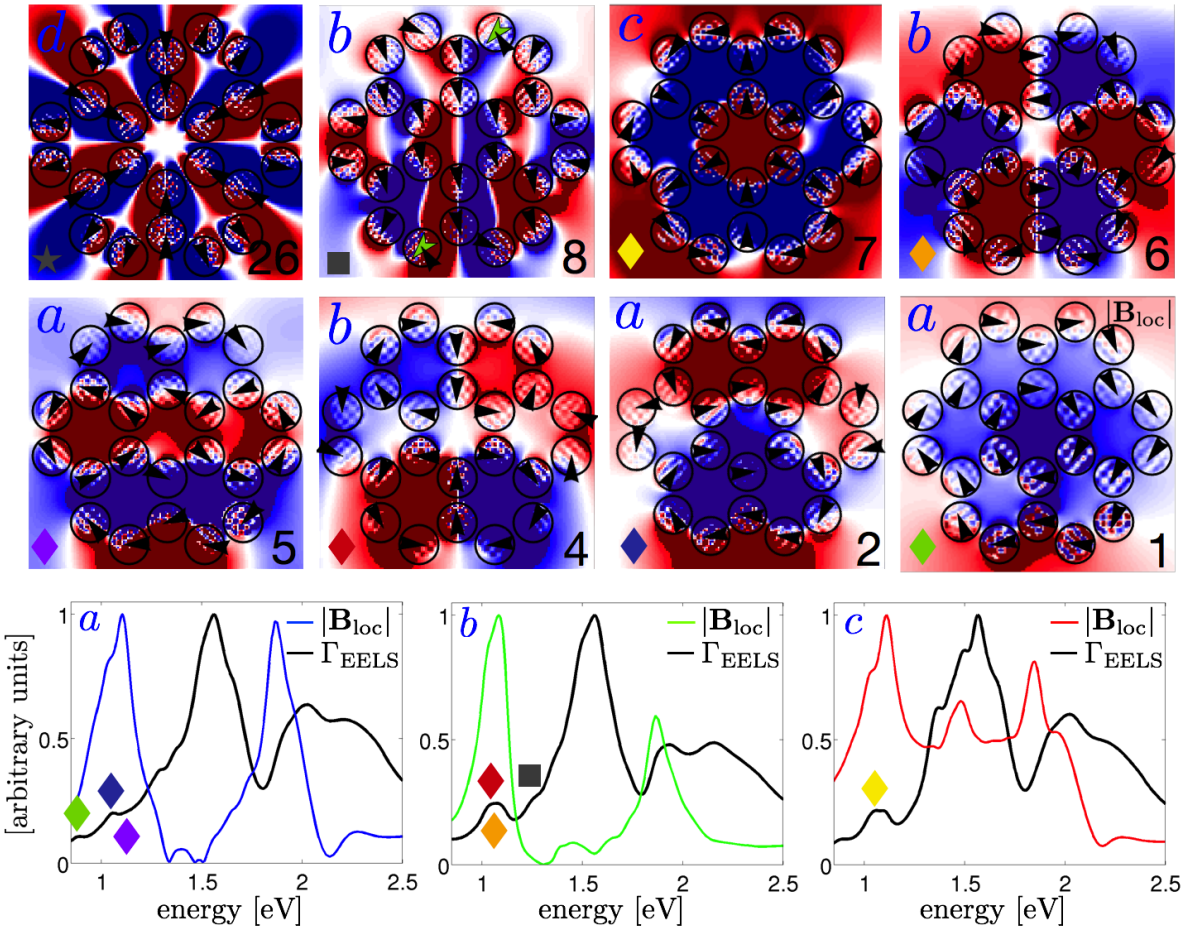

Figure 4.8: Normalized EEL probability Γ_{EELS} (black) and signed local magnetic field magnitude $|\mathbf{B}_{\mathrm{loc}}|$ (blue/green/red) spectra (lower panel) of the 6-mer computed within the *e*-DDA. The electron beam is positioned at the aloof locations *a*, *b*, *c*, and *d* denoted in the right panel of 4.2. The upper panels display the spatial behavior of a few of the 6-mer's collective eigenmodes that are excited at beam positions *a*, *b*, *c*, and *d*. The corresponding tight-binding eigenmode is enumerated within each of the upper panels. Of particular importance is the ferromagnetic ground state (blue, ♦), where the magnetic moments in all unit cells point in the same direction. The maximally nodal antiferromagnetic plasmon excited state (orange, ♦), where magnetic moments in each unit cell alternate in direction, is the highest lying magnetic plasmon of closed-loop character in the spectrum. Others of varying nodal order in both radial and angular directions appear in between these two modes. Also a giant dipole (■) appears in the spectrum above all closed-loop magnetic plasmon modes. The large peak in the EEL function near 1.5 eV is due, in part, to the excitation of the giant radial breathing mode of the 6-mer (★). For this reason we do not display the EEL spectrum at beam position *d*.

The electron-induced $|\mathbf{B}_{\mathrm{loc}}|$ is computed by averaging the local magnetic field induced inside of the closest 1-mer ring unit to the electron beam. The upper panels show the spatial behavior of the $|\mathbf{B}_{\mathrm{loc}}|$ associated with eight of the collective plasmon eigenmodes of the 6-mer, all of which are predicted from and are enumerated in accordance with the tight-binding eigenstates labeled by ν. The ground state of the 6-mer is a giant closed-loop ferromagnetic plasmon resonance that is characterized by a colinear arrangement of the magnetic moments in all six unit cells (green, ♦). It is important to point out that the central open ring within the 6-mer acts as an effective seventh unit cell and is involved in defining the magnetic moment of the ground state. In fact this central ring also participates in the $\nu = 7$ ferromagnetic eigenmode (yellow, ♦), which has one radial node separating it from the ground state, making it the first ferromagnetic excited state. This is contrast to the aromatic benzene molecule where all six of the π molecular orbitals are nearly zero in magnitude in the empty space within the six-membered carbon ring. In addition to these ferromagnetic plasmon modes the electron beam is also able to access all of the multipolar magnetic plasmon resonances of arbitrary nodal order in the angular direction ($\nu = 2, 4, 5, 6$). These modes are all of antiferromagnetic character since they have no net magnetic moment. For completeness we also show one of the giant electric dipoles (■) as well as a giant radial breathing mode (★). The latter appears most clearly at beam position d at 1.485 eV; however, since this resonance can also be seen at positions a, b, and c we do not show the EEL spectrum at position d. What we see developing here is that each class of hybridized magnetic and electric plasmon resonance of the N-mer (i.e., the antiferromagnet, ferromagnet, giant electric dipole, and radial electric breathing modes) has a ground state as well as a family of excited states of increasing nodal order.

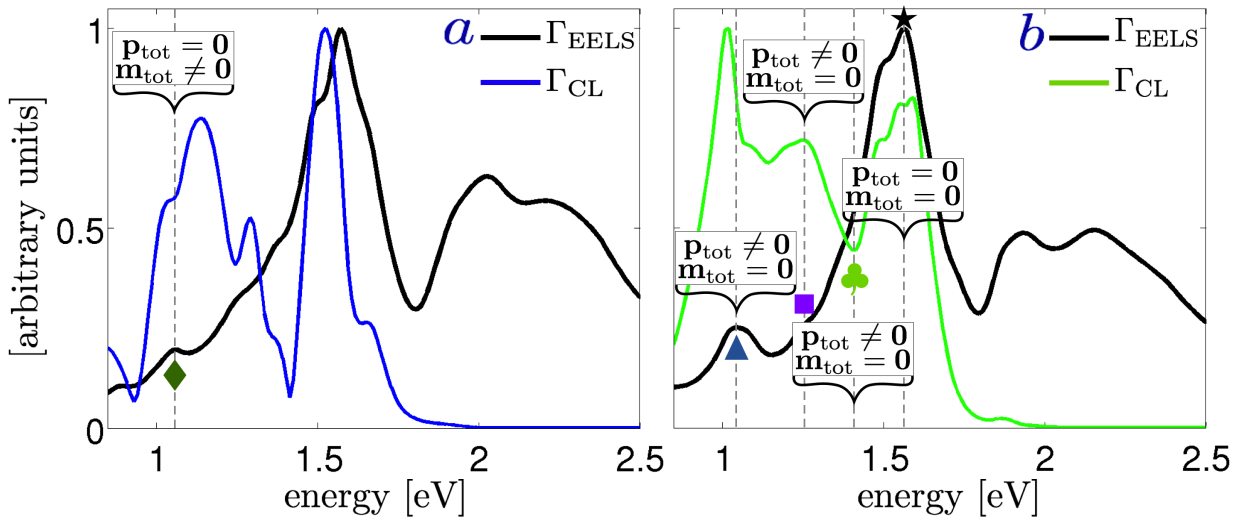

Figure 4.9: Normalized CL (blue/green) and EELS (black) responses of the same 2-mer system described previously in 4.7, computed *via* the *e*-DDA. The electron beam is positioned at the aloof locations *a* and *b* denoted in the middle panel of 4.2. All panels are computed from full-wave numerical electrodynamics simulations within the *e*-DDA. Because the CL spectrum encodes resonances of either net electric dipole $\mathbf{p}_{\mathrm{tot}}$ or net magnetic dipole $\mathbf{m}_{\mathrm{tot}}$ character (or neither) it is expected that the ferromagnetic ground state of the 2-mer (♦) will be visible in CL due to its finite magnetic dipole moment. The same is true for the antiferromagnetic excited state (▲) due its finite electric dipole moment. However, with $\mathbf{p}_{\mathrm{tot}} = \mathbf{m}_{\mathrm{tot}} = \mathbf{0}$ it is surprising to find the radial breathing mode (★) in the CL spectrum. This is due to the fact that the spatial localization of the electron beam excitation biases the system so that in the presence of loss a finite dipole moment arises even when the eigenmode itself has none. This is why eigenmodes of even formally zero electric and magnetic dipolar character can have a CL response. For comparison, the net moments $\mathbf{p}_{\mathrm{tot}}$ and $\mathbf{m}_{\mathrm{tot}}$ of the tight-binding eigenmodes themselves are overlaid upon the five resonances of interest.

Lastly, we discuss the differences between the STEM electron beam and the plane wave as an excitation source. In addition to this, we examine the signatures of the N-mer's various collective eigenmodes in cathodoluminescence spectroscopy. We have demonstrated that a subset of the full eigenspectrum of the N-mer can be excited in the STEM and detected in EELS by raster scanning to the appropriate beam position; other eigenmodes, which are not shown, are accessible at other locations. However, due to the polarization structure and

delocalized nature of the plane wave in contrast to the localized evanescent electric field of the electron, the plane wave is incapable of accessing the entire eigenspectrum. When the plane wave's electric field is oriented in the plane of the N-mer, only those collective plasmon resonances of net electric dipolar character parallel to the polarization axis can be excited. Examples of this are the giant electric dipoles described previously. Alternatively, when the plane wave's magnetic field is oriented normal to the plane of the N-mer, a ring current is set up whose associated magnetic field acts to oppose the applied field in accordance with Lenz's law. This is precisely how the ground state magnetic plasmon of a single ring nanosystem was excited in Ref. [141]. But this means that the magnetically polarized plane wave can excite only those magnetic plasmons of ferromagnetic character, because the associated antiferromagnetic plasmons have no net magnetic moment and, therefore, are incapable of screening the applied magnetic field.

The CL response of the N-mer elucidates its collective magnetic and electric character further by indicating the net or total magnetic and electric dipole character of each eigenmode. An interesting consequence of the electron probe is that even plasmon eigenmodes that have no net electric dipole moment under plane wave excitation can have a finite electric dipole character in electron spectroscopy due to the spatial localization of the electron beam when placed away from the target's center of symmetry. As a result, both ferromagnetic and antiferromagnetic plasmons can be detected in CL as well as EEL spectroscopies, though with weaker oscillator strength. 4.9 compares the CL and EELS responses of the 2-mer, to illustrate the different information contained in each spectrum for the simplest nontrivial N-mer system. It is clear that both closed-loop magnetic modes (♦, ▲) of the 2-mer appear

in the CL spectra, the ferromagnetic mode by having a finite magnetic dipole moment (♦) and the antiferromagnetic mode (▲) by having a finite electric dipole moment. Other non-magnetic modes with a net electric dipole moment (■, ♣) have CL responses as well. Interestingly, the $\nu = 19$ eigenmode (★) has no net electric or magnetic dipole, yet a strong response appears in the CL simulations at this loss energy due to the bias induced by the deep subwavelength localization of the electron beam. It is unclear if the small dip near 1.55 eV is the result of the lack of an electromagnetic dipole moment for mode 19, or if it is the result of other nearby mode structure dominating the response. In general, for these N-mer systems, the CL spectrum closely tracks the EELS spectrum in the region where the surface plasmon resonance of each nanodisk is well described by an electric dipole. At higher energies the responses of the nanodisks begin to take on a quadrupolar character and the CL response drops to zero. Since the electric polarization of each nanodisk has no net dipole moment at these energies, the bias introduced by the position of the electron beam does not affect the CL spectrum.

4.5 Conclusion

Recent experimental advances in probing the magneto-optical properties of cyclic assemblies of plasmon-supporting metal nanoparticles linked into extended oligomers have provided impetus for a corresponding rigorous theoretical understanding of their rich structure and energetics. In this paper we present a first-principles theoretical description of the hybridization of the fundamental electric plasmons of each nanoparticle in the assembly into a family of delocalized oligomer plasmons based upon a combination of microscopic elec-

tric and macroscopic magnetic tight-binding models. Diagonalization of the corresponding Hamiltonian reveals a variety of hybridized surface plasmon resonances spanning the entire system, such as closed-loop magnetic plasmons of both ferromagnetic and antiferromagnetic character of varying multipolar order, giant electric dipole plasmons, and even plasmons that behave as giant radial breathing modes. The eigenmode spectrum is investigated in detail for three particular cyclic oligomers, the 1-mer, 2-mer, and 6-mer, and comparison is made to full-wave numerical simulations of their electron-driven responses. It is found that the tight-binding formalism is in excellent agreement with the simulated EELS and, further, that all of the aforementioned modes can be systematically probed by the STEM electron beam and detected in EELS. Comparison is made to plane wave excitation as well as to the CL response of the system. The work presented in this paper provides a rigorous and complete way to think about the collective electronic resonances of general oligomer systems of arbitrary morphology and material composition, advancing the design of future metamaterials with unprecedented magneto-optical properties.

4.6 Methods

4.6.1 Electron energy loss and cathodoluminescence simulations in e-DDA

The coupled-dipole [43] or DDA [47] approach is routinely used to study the response of metal nanoparticles subjected to optical-frequency radiation [98]. In our previous work we developed and numerically implemented the e-DDA [60, 100] as a generalization of this

approximation, incorporating the electron beam of a STEM in place of a plane-polarized electric field source as is common to the DDA. In the e-DDA the target is discretized into a finite collection of polarizable point dipoles $\mathbf{P}_j$, $1 \leq j \leq N$, each driven by the evanescent electric field

$$\mathbf{E}_{\text{electron}}(\mathbf{x},\omega) = \frac{2e\omega}{v^2\epsilon\gamma} e^{i\omega z/v}\Big[\frac{i}{\gamma}K_0\Big(\frac{\omega b}{v\gamma}\Big)\hat{\mathbf{v}} - K_1\Big(\frac{\omega b}{v\gamma}\Big)\hat{\mathbf{b}}\Big] \tag{4.9}$$

of a passing swift electron as well as by the fully retarded electric-dipole field $\sum_{j\neq i}^{N} \mathbf{\Lambda}_{ij}\mathbf{P}_j$ generated by all other points; here $\mathbf{\Lambda}_{ij} = e^{ikr_{ij}}\{(1/r_{ij}^3 - ik/r_{ij}^2)[3\hat{\mathbf{n}}_{ij}\hat{\mathbf{n}}_{ij} - \mathbf{1}_{ij}] - k^2\hat{\mathbf{n}}_{ij} \times (\hat{\mathbf{n}}_{ij}\times)/r_{ij}\}$ is the standard dipole tensor that relays the electric field generated by a dipole at one point in space $\mathbf{x}_i$ to another $\mathbf{x}_j$ a distance $r_{ij}\hat{\mathbf{n}}_{ij} = |\mathbf{x}_i - \mathbf{x}_j|\hat{\mathbf{n}}_{ij}$ away. In this manner, the electron-induced responses of the system can be computed once each dipole is brought into self consistency with all others at a certain value of the electron's loss energy, $\hbar\omega$. This is accomplished through the iterative solution of the following equation,

$$\sum_{j=1}^{N}[\boldsymbol{\alpha}_{ii}^{-1}(\omega)\delta_{ij} - (1-\delta_{ij})\mathbf{\Lambda}_{ij}]\cdot\mathbf{P}_j(\omega) = \mathbf{E}_{\text{electron}}(\mathbf{x}_i,\omega), \tag{4.10}$$

and depends upon the frequency-dependent linear polarizability $\boldsymbol{\alpha}_{ij}(\omega) \equiv \boldsymbol{\alpha}_{ii}(\epsilon(\omega))\delta_{ij}$ of the target point i. The polarizability is related to the dielectric function through the lattice dispersion relation [99]. The electric field of the electron [38] in 4.9 depends upon the modified Bessel functions of the second kind K_0 and K_1, the Lorentz contraction factor $\gamma = 1/\sqrt{1-\epsilon(v/c)^2}$, and the dielectric function ϵ of the background medium, which is taken

to be vacuum in all presented calculations. The incident velocity $\mathbf{v} = v\hat{\mathbf{v}}$ of the electron is determined by its incident kinetic energy $m\gamma c^2 - mc^2$, and is oriented along the z axis. We choose the phase $e^{i\omega z/v} = 1$ at the z-height of the mass centroid of the target, which defines the plane of the impact parameter $\mathbf{b} = b\hat{\mathbf{b}}$, with $\mathbf{x} = (\mathbf{b}, z)$ that is perpendicular to the electron beam and that contains this point.

All target structures investigated via *e*-DDA simulations are excited by a 100 keV electron beam directed normal to plane of the N-mer; the corresponding velocity of the electrons in the beam is $0.55c$. Only aloof trajectories through vacuum are considered in the simulations and the electron beam never placed within one dipole spacing from the target, which is discretized at a dipole spacing of 5 nm; other values were tested to ensure that all spectra are converged at this value. Dielectric data from Johnson and Christy [101] is used for gold.

The most recent version of the *e*-DDA code [100] computes CL spectra and spatial maps in addition to EEL properties. The electron-induced response, $\mathbf{P}_j$, of the target is solved at each spatial position of the electron beam according to 4.10 as in the previous version of our code. However, for CL, at each spatial position of the beam and at each value of the loss energy, the induced electric field $\mathbf{E}_{\text{ind}}$ is computed according to

$$\mathbf{E}_{\text{ind}}(\mathbf{x}, \omega) = \sum_{j=1}^{N} \mathbf{\Lambda}(\mathbf{x}, \mathbf{x}_j) \cdot \mathbf{P}_j(\omega) \tag{4.11}$$

at various points $\mathbf{x}$ in the far-field. For the *e*-DDA-based CL calculations performed in this

article, $\mathbf{E}_{\text{ind}}$ is computed on an angular grid of points spanning the surface of distant sphere of radius 5 μm, with 75 points in θ and 75 points in ϕ. In this way, either the differential CL response $d\Gamma_{\text{CL}}/d\Omega$ or, by quadratured solid-angle integration, the total CL response Γ_{CL} may be computed.

4.7 Author contributions

[#]C. Cherqui and N. W. Bigelow contributed equally to this work.

4.8 Notes

The authors declare no competing financial interest.

4.9 Acknowledgements

This work was supported by the National Science Foundation's CAREER program under award number CHE-1253775 and through XSEDE resources under award number PHY-130045 (D.J.M.). The authors wish to thank Steven Quillin and Niket Thakkar from the University of Washington as well as Prof. John F. Stanton from the University of Texas at Austin for fruitful discussions.

Chapter 5

Signatures of Fano Interferences in the Electron Energy Loss Spectroscopy and Cathodoluminescence of Symmetry-Broken Nanorod Dimers

This work has previously been published in the following article:

N. W. Bigelow, A. Vaschillo, J. P. Camden, and D. J. Masiello.

ACS Nano **7**, 4511 (2013)

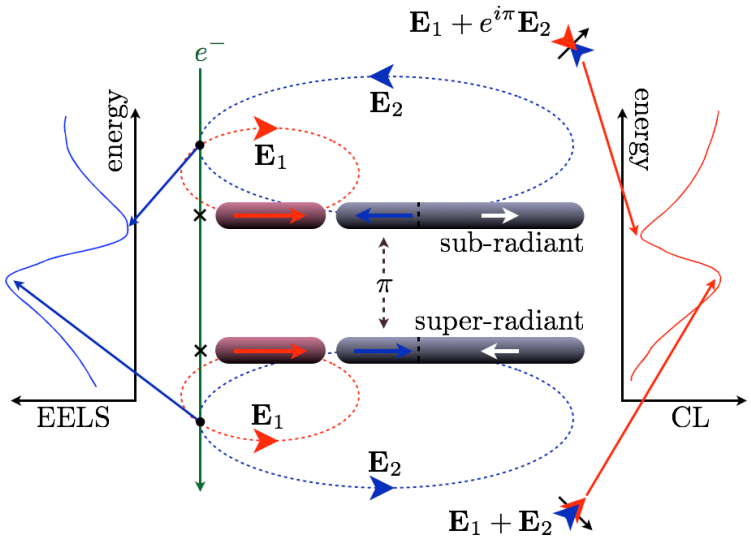

Figure 5.1: Abstract figure.

5.1 Abstract

Through numerical simulation, we predict the existence of the Fano interference effect in the electron energy-loss spectroscopy (EELS) and cathodoluminescence (CL) of symmetry-broken nanorod dimers that are heterogeneous in material composition and asymmetric in length. The differing selection rules of the electron probe in comparison to the photon of a plane wave allow for the simultaneous excitation of both optically bright and dark plasmons of each monomer unit, suggesting that Fano resonances will not arise in EELS and CL. Yet, interferences are manifested in the dimer's scattered near- and far-fields and are evident in EELS and CL due to the rapid π-phase offset in the polarizations between super-radiant and sub-radiant hybridized plasmon modes of the dimer as a function of the energy loss suffered by the impinging electron. Depending upon the location of the electron beam, we demonstrate the conditions under which Fano interferences will be present in both optical and electron spectroscopies (EELS and CL) as well as a new class of Fano interferences that

are uniquely electron-driven and are absent in the optical response. Among other things, the knowledge gained from this work bears impact upon the design of some of the world's most sensitive sensors, which are currently based upon Fano resonances.

5.2 Introduction

Interference is ubiquitous in nature. It can be heard in the discord of out-of-tune musical instruments, seen in the skipping of a rock on a still pond, and evidenced as electrons are subjected to the famous double slit. In 1961, Ugo Fano explained the asymmetric line shapes observed in the spectrum of helium vapor under electron impact as being due to the interference between the scattering amplitudes for the incident electron to scatter directly and to scatter *via* autoionization [68]. A similar asymmetric line shape is observed in the optical scattering spectra of metal nanostructures when a bright plasmon mode is resonantly coupled to a dark plasmon [51, 71, 141, 196, 197]. From the excited bright mode, energy is transferred nonradiatively to the dark mode and back to the bright, with a π-phase offset. Both excitations superimpose and destructively interfere on the bright mode, which radiates a signal into the far-field that is characterized by an asymmetric Fano line shape.

Electron spectroscopies like electron energy-loss spectroscopy (EELS) and cathodoluminescence (CL) are rapidly emerging as important tools in the characterization of plasmon resonances due to their sub-Ångstrom spatial resolution [11, 90, 198]. EELS has been used to investigate the plasmonic properties of a wide variety of nanostructures, including cubes [85], spheres [80, 81], prisms [55, 199], split-ring resonators [200], rods [60, 83, 129, 201],

and complex star-like structures [201]. Nanoparticle aggregates have also been explored with EELS, including nanodisk multimers [71], dolmen-like structures [51], sphere trimers [141], asymmetric sphere dimers that are homogeneous in composition [81], cube dimers [89], planar triangular dimers and trimers [94], and nanorod dimers [60, 202, 203]. Over the past few years a number of experimental and theoretical efforts have exploited EELS and CL to better understand how nanoparticles interact, broadcast energy to the far-field, and store energy in the near-field [11, 204–206]. The signatures of electromagnetic hot spots and the relationship between the local density of states and EEL probability is now well understood [60, 62, 89, 97]. Yet, in light of this wealth of knowledge, it is still unclear if and under what conditions Fano interferences will appear in EELS and CL, and what the optical response will be in these situations. Since plasmon modes that are optically dark may be bright under electron excitation, it seems that Fano interferences will be absent in electron spectroscopies. To date, all nanostructures that display Fano resonances in their optical spectra reported in the literature have not shown them in EEL or CL spectroscopies at the same energies [51, 71]. Advances in the energetic sensitivity of EELS will play an important factor in finding electron-induced Fano-like interference features, as they can be spectrally sharp and difficult to observe in the laboratory [37, 207, 208]. It is the purpose of this article to guide experiment in this pursuit by predicting the electron-induced optical frequency responses of metal nanorod dimers *via* numerical simulation.

Both EEL and CL spectroscopies are initiated by a collimated stream of swift electrons, often originating from a scanning transmission electron microscope (STEM), impinging upon a target. Most electrons are elastically scattered. However, inelastic scattering events occasion-

ally occur as electrons suffer kinetic energy losses in exchange for the creation of elementary and/or collective excitations in the target [11]. For noble metal nanostructures, it is the latter type of response that is important, corresponding to surface plasmon resonances that are usually excited at optical frequencies.

Due to the differing selection rules between the electron probe, which acts as a nano-localized source of broadband electromagnetic radiation, and a far-field source of monochromatic light like a plane wave, both optically bright and dark plasmon modes of the target may be excited by the electron. Only those modes with a net dipole moment are capable of out-coupling their energy to the far-field and are identifiable in CL spectra. Yet both bright and dark modes may contribute to the EEL spectrum. The EEL signal

$$\Gamma_{\mathrm{EELS}}(\hbar\omega) = \frac{e}{\pi\hbar^2\omega}\int dt \mathrm{Re}\{e^{-i\omega t}\mathbf{v}\cdot\mathbf{E}_{\mathrm{ind}}(\mathbf{r}(t),\omega)\} \tag{5.1}$$

is determined from the work done on the impinging electron, located at $\mathbf{r}(t)$, by its induced electric field, $\mathbf{E}_{\mathrm{ind}}$. Γ_{EELS} represents the probability for the electron to lose kinetic energy to the target per unit of energy loss suffered by the passing electron. When the STEM is scanned in the vicinity of the target, it is mainly the near-field components of $\mathbf{E}_{\mathrm{ind}}$ that contribute to Γ_{EELS}. While the total CL signal

$$\Gamma_{\mathrm{CL}}(\hbar\omega) = \frac{cr_S^2}{4\pi^2\hbar^2\omega}\int d\Omega |\mathbf{E}_{\mathrm{ind}}(\mathbf{x}_S,\omega)|^2 \tag{5.2}$$

is determined from integrating the radiative energy flux carried by the far-field components of the induced electric field, $\mathbf{E}_{\mathrm{ind}}(\mathbf{x},\omega) \sim \mathbf{f}(\Omega)e^{ikr}/r$, over the surface of a distant flux screen of radius $r_S = |\mathbf{x}_S|$, with $kr_S \gg 1$ [11]. It represents the number of photons emitted in all directions at the energy $\hbar\omega$ per incoming electron. Both of these expressions are parametrized by the path of the electron, described by $\mathbf{r}(t)$. In this way, EELS is characterized by a near-field probe and near-field observation, while CL is characterized by a near-field probe and far-field observation. This is in contrast to optical spectroscopy, where both the excitation source and observation are in the far-field. It is also important to note that aggregates of nanoparticles may support hybridized plasmon modes that are super- or sub-radiant in character. Neither mode is dark and both may store electromagnetic energy in the near-field as well as carry electromagnetic energy to the far-field. These particular properties will be important in the following in understanding interference effects in optical and electron spectroscopies.

In this paper, we explore the consequences of Fano interferences in electron and optical spectroscopies between multipolar plasmonic excitations in symmetry-broken nanorods that are heterogeneous in material composition and asymmetric in length. These interferences arise from the phase offsets between the electric dipolar (bright) plasmon of a Pd rod with the electric quadrupolar (dark) plasmon of a nearby Ag rod. Both of these plasmonic responses are excited by the electron beam and may hybridize into super- and sub-radiant plasmons that store and radiate electromagnetic energy in the near- and far-field. The relative size of each monomer unit is tuned so that these Pd and Ag plasmon resonances overlap spectrally and, depending upon the position of the electron beam, their interference can be read out in

the near-field *via* EELS and in the far-field *via* CL. In addition, we identify the conditions where both the far-field optical and CL scattering evidence Fano interferences as well those conditions where interferences are absent in the optical response but are present in the CL. The understanding gained from this particular system guides us in predicting if and how interference features will arise in the electron and optical spectroscopies of more general systems. This will be of significant importance particularly in the development of high-sensitivity plasmon-based sensors, where Fano resonances currently underlie some of the world's best [28–30].

5.3 Results and discussion

5.3.1 Fano interferences in electron energy-loss spectroscopy

To examine the signatures of Fano interferences in EELS and CL, we perform numerical simulations on a nanorod dimer using our recently implemented electron-driven discrete-dipole approximation (e-DDA) [60]. The e-DDA is a generalization of the DDA concept [43, 47] to include the electron source of a STEM instead of a plane wave. In this article, the e-DDA is further extended to compute CL. For simplicity in presentation, a description of the theory and numerical implementation of the e-DDA is deferred to the Methods section.

Symmetry breaking

We begin by engineering a metal nanostructure that supports Fano resonances in both optical and electron spectroscopies. High aspect ratio rods make an ideal test bed for these studies because they support a multipolar progression of alternating, longitudinally polarized bright

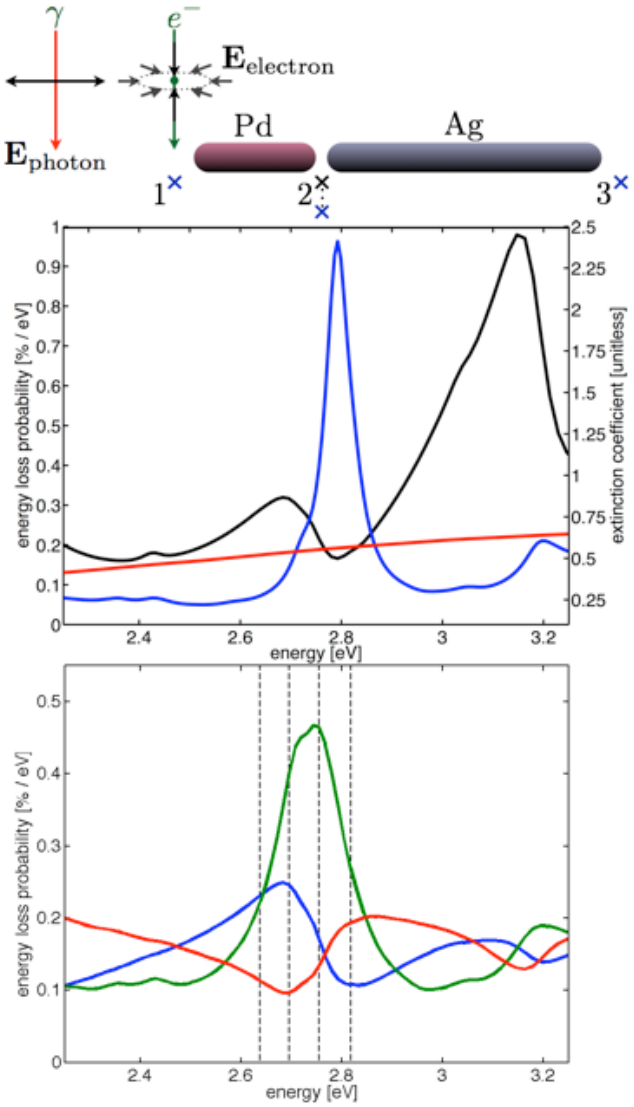

Figure 5.2: Optical and electronic responses of a symmetry-broken Pd-Ag nanodimer. Upper panel: a depiction of the dimer system is displayed together with the locations of three positions of the electron beam used to interrogate the system; positions 1 and 3 are computed 1 nm off of the respective rod's tip and have an impact parameter $b_y = 1$ nm off of the rod's surface (11 nm from the rod's center); position 2 is centered in the junction and has an impact parameter that ranges between 1 and 30 nm off of the rod's surface ($b_y = 11$ to 40 nm from the junction center) in addition to the junction center ($b_y = 0$ nm). Middle panel: the optical spectrum of the mixed-metal dimer is presented (black) as are the EEL spectra of the Ag (blue) and Pd (red) monomers excited at their ends. A pronounced Fano interference "dip" is apparent near 2.80 eV in the optical spectrum. Lower panel: the EEL spectra corresponding to each of the three positions in the upper panel are presented. Position 1 is displayed in blue, position 2 (computed at $b_y = 30$ nm) is displayed in red, and position 3 is displayed in green; the EEL probability at position 2 is multiplied by 5 to aid in visualization. Fano interference features are clearly visible in the EEL spectra taken from positions 1 and 2. While no interference is observed in the EEL spectrum at position 3.

and dark plasmon modes that can be spectrally tuned by altering the rod's composition and length. Asymmetric nanorod dimers offer the possibility for an optically dark plasmon on one monomer unit to spectrally overlap an optically bright mode on the other. In addition, the symmetry of such a heterodimer is lowered in comparison to the corresponding monomer in such a way that the two modes may couple. More precisely, before adding a second particle, the odd-parity (bright) and even-parity (dark) modes of the rod monomer do not interact because they belong to different irreducible representations of the $C_{\infty v}$ point group (neglecting the presence of the electron probe). However, after breaking the symmetry by the addition of a second particle, both even- and odd-parity plasmons transform according to the same irreducible representation of the C_s group and, therefore, can interact. Further, the spatial symmetry-breaking induced by the placement of the electron beam itself is enough to allow odd- and even-parity plasmons on a single rod monomer to interact, but tuning the spectral positions of these modes so that they overlap is challenging.

5.2 presents the optical and electron spectra of a symmetry-broken Pd-Ag nanorod dimer as well as the spectra of their corresponding monomers. We choose these metals because the Pd dipole is quite lossy in the optical regime and makes an ideal candidate for the requisite *broad* and *bright* mode, while the Ag quadrupole is *narrow* and *dark*. Other choices of metals that have similar properties may also serve as ideal candidates. As depicted in the top panel, the left rod is composed of Pd and has a length of a 50 nm, while the right rod is composed of Ag and has a length of 100 nm; they both have a 10 nm radius, are colinearly arranged, and are separated by a gap of 1 nm. The lengths of each monomer unit have been adjusted so that the spectrally narrow and optically dark electric quadrupole ($n = 2$) and optically

bright electric hexapole ($n = 3$) plasmon of the Ag rod (blue curve) overlap the broadband optically bright electric dipole ($n = 1$) plasmon of the Pd rod (red curve) as displayed in the middle panel.

On the basis of these symmetry properties, we expect to find a Fano interference feature in the optical spectrum of the dimer in the vicinity of the Pd dipole-Ag quadrupole overlap, due to the near-field energy exchange between bright and dark modes and the subsequent interference originating from their relative phase offset. Indeed this is true, as exemplified by the black curve in the middle panel. A pronounced Fano "dip" in the extinction spectrum is visible near 2.80 eV, where the Ag quadrupole (blue curve) and Pd dipole (red curve) plasmons interfere. Interestingly, no such pronounced feature occurs if both rods are of the same material composition, due to the poor spectral overlap between super- and sub-radiant plasmons. This may not be true in general, but is true if both rods are Pd or both are Ag.

Electron-driven Fano resonances

The question now remains of what the EEL response will be when the STEM is rastered across different points surrounding the target. The lower panel of 5.2 presents the EEL spectra corresponding to the three different spatial points indicated in the upper panel. In all calculations, an aloof 0.10 MeV electron beam is used to perturb the system. Interestingly, we see that three qualitatively different responses are predicted.

The blue curve is the EEL spectrum resulting from an electron beam placed at position 1. Comparison with the optical spectrum in the middle panel (black curve) shows that both ex-

hibit a similar Fano line shape and associated dip near 2.80 eV. However, the mechanism for this interference in EELS is somewhat different from that occuring in optical spectroscopy. First, both the bright Pd dipole plasmon and dark Ag quadrupole plasmon are simultaneously co-excited to some extent by the electron beam. For loss energies between ~ 2.45 and 2.65 eV, the passing electron is able to efficiently pump energy through the Pd dipole into the super-radiant hybridized plasmon mode of the dimer (displayed in the caption figure). While for loss energies exceeding ~ 2.70 eV, the sub-radiant hybridized plasmon mode (displayed in the caption figure) is more energetically favorable yet is difficult to excite with the electron beam positioned at point 1. This is because the polarization of the electron's evanescent electric field (see 3.1 below) pins the orientation of the Pd dipole and forces the polarization of the Ag quadrupole to flip its phase by π at loss energies greater than ~ 2.70 eV. For these reasons, there is a higher EEL probability below the Fano resonance frequency (~ 2.75 eV) than above. It is worth noting that an Alzar model [69] describing the nanorod dimer as a system of coupled springs driven out of phase also reproduces these Fano interferences.

A strikingly different EEL spectrum results when the electron beam is positioned at point 2 (red curve). There, the sub-radiant hybridized plasmon mode is more efficiently pumped, which leads to an inverted Fano line shape that is optically inaccessible. At loss energies above ~ 2.70 eV, the sub-radiant mode is resonant and, indeed, the EEL probability is larger there. For loss energies below ~ 2.70 eV the super-radiant mode is more energetically favorable but is difficult to excite with the electron beam near the junction. This is because the polarization of the electron's evanescent electric field pins the antibonding arrangement of polarizations in the vicinity of the junction and either the Pd dipole or Ag quadrupole must

flip the phase of its polarization by π to accommodate the super-radiant configuration. The probability for the passing electron to lose energy into this arrangement is, consequently, smaller.

When the electron beam is rastered to position 3 (green curve), no interference is observed in EELS. This is because the electron beam is perfectly positioned to drive the Ag quadrupole with high probability. At loss energies below $\sim$ 2.75 eV the quadrupole funnels energy into the super-radiant plasmon mode, while for loss energies greater than $\sim$ 2.75 eV the quadrupole funnels energy into the sub-radiant plasmon mode. At this position the electron beam only pins the polarization of the Ag quadrupole, leaving the distant Pd dipole flexible to flip its phase by π between super- and sub-radiant orientations. However, the electric near-field induced by this π-phase offset of the Pd rod provides only a small perturbation to the near-field of the Ag quadrupole acting back upon the electron at position 3. Therefore, almost no interference signature is manifested in the EEL spectrum at this position of the electron beam.

At positions 1 and 2, there is a corresponding interference in the electric near-field generated by the superposition of oscillating bright and dark plasmonic modes. 5.3 displays the spectrum of the unit normalized induced electric-field magnitude (green curves) evaluated at positions 1 and 2 of the electron beam, together with the corresponding EEL spectrum (red curves) at each position. Pronounced destructive and constructive interference dips and peaks in the field magnitude are clearly visible at the loss energies where the electron-induced Fano resonances occur. These spectral features impact the EEL probability as governed by

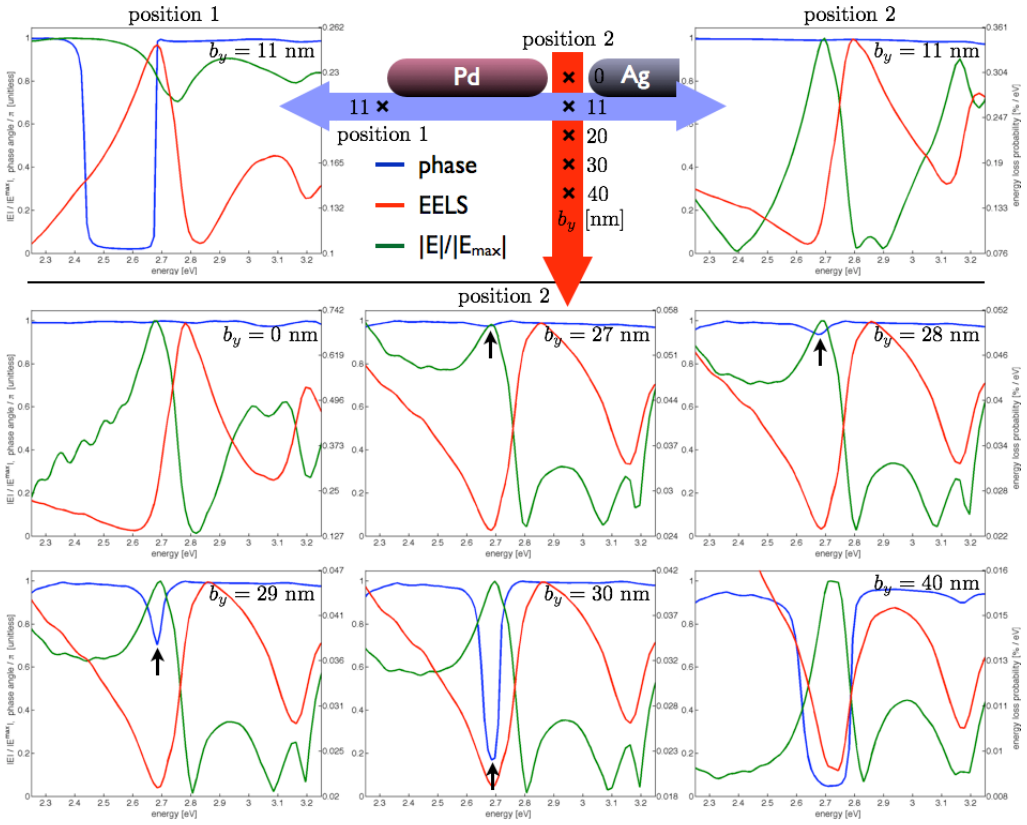

Figure 5.3: EEL spectrum (red) and magnitude (green) and phase (blue) of the scattered electric near-field evaluated at positions 1 and 2 where electron-induced Fano interferences occur. The electric field magnitude is normalized so that its maximum takes a value of 1 in each panel. Upper left panel: at position 1, the electron beam is oriented to pump the super-radiant plasmon mode of the dimer through the Pd dipole between ~ 2.45 and 2.65 eV. However, as the loss energy approaches 2.75 eV, the sub-radiant plasmon becomes resonant and the phase of the polarization of the Ag quadrupole flips from 0 to π, resulting in a destructive interference of the induced electric field at position 1 and a corresponding Fano resonance near 2.75 eV. Upper right panel: at position 2, when the electron beam is placed at $b_y = 11$ nm there is no Fano resonance. This is due to the fact that the electron beam is locally pinning the sub-radiant plasmon, which maintains a relative phase offset of π for all loss energies. Lower panels: nonetheless, a Fano resonance can be activated at position 2 by rastering the electron beam to larger impact parameters, b_y, away from the junction within the impact plane. As b_y increases from 0 to 40 nm a pronounced relative phase offset rapidly grows between monomer units (black arrows). At these positions, the electron beam is oriented to pump a locally antibonding arrangement of the plasmon polarization in the vicinity of the junction, which is consistent with the sub-radiant plasmon configuration. The corresponding electric field induced by this local configuration is destructive. However, as the loss energy is lowered to ~ 2.70 eV, the super-radiant plasmon mode becomes resonant and the Pd dipole flips its phase by π to accommodate the resonant configuration. This forces the relative plasmon phase delocalized across the dimer to fall to 0 near ~ 2.70 eV, and leads to a constructive interference of the associated induced electric field and an associated Fano resonance. Position 3 is not investigated since no significant interference in the EEL spectrum is observed at impact parameters, b_y, near that point.

the loss function in 5.1, opening up effective transparency and opacity windows of minimized and maximized EEL probability.

In the upper left panel of 5.3 corresponding to position 1, the electric field minimum near 2.75 eV is due to the polarization flip of the Ag rod's quadrupole plasmon. Because the superposition of induced electric fields at position 1 is constructive before the polarization flip, it becomes destructive afterward. This is the scenario portrayed in the caption figure. In the upper right panel corresponding to position 2 with an impact parameter $b_y = 11$ nm, the electron beam pins the locally antibonding arrangement of polarizations, with a correspondingly destructively interfering induced electric field in the junction. This is the energetically favorable plasmon configuration at loss energies greater than ~ 2.80 eV. At lower loss energies, where the super-radiant mode is resonant, either the Pd dipole or Ag quadrupole must flip its phase to accommodate the new configuration and the superposition of induced electric fields becomes constructive in character.

To further elucidate the underlying plasmonic motion responsible for these interference effects, we additionally plot in 5.3 the relative phase ϕ (blue curves) of the electron-induced electric field evaluated at the position of the impinging electron. 5.1 dictates that the EEL signal is determined from the work done by the electron's induced electric field acting back upon the electron. However, in the case of the nanorod dimer the electron "sees" the superposition of electric fields scattered from both the Pd and Ag rods as $\mathbf{E} = \mathbf{E}_{\mathrm{Pd}} + e^{i\phi}\mathbf{E}_{\mathrm{Ag}}$, with magnitude

$$|\mathbf{E}(\mathbf{x}_j)| = \sqrt{|\mathbf{E}_{\mathrm{Pd}}(\mathbf{x}_j)|^2 + |\mathbf{E}_{\mathrm{Ag}}(\mathbf{x}_j)|^2 + 2|\mathbf{E}_{\mathrm{Pd}}(\mathbf{x}_j)||\mathbf{E}_{\mathrm{Ag}}(\mathbf{x}_j)|\cos\phi}, \tag{5.3}$$

with j = position 1, 2.The dependence of ϕ upon the loss energy indicates how the polarization of each monomer unit contributes to the total polarization of the super- or sub-radiant plasmon delocalized across the dimer. When the two monomers are out of phase by π, then they participate in the sub-radiant hybridization. While they compose the super-radiant hybridization when they are in phase.

At position 1 (upper left panel) a pronounced phase shift (blue curve) occurs rapidly near 2.70 eV as the plasmonic motion transforms between super- and sub-radiant configurations. Corresponding to this π phase shift of the Ag quadrupole is a Fano resonance in the EEL spectrum (red curve). Interestingly, even though there is an asymmetric EEL line shape at position 2 at an impact parameter of $b_y = 11$ nm, there is no Fano resonance. This can determined by examining the plasmon's relative phase, which remains near π for all loss energies. The rigidity of this phase is due to the fact that the swift electron passing near to the junction mainly feels the strong local polarization of the junction, which is pinned in an antibonding configuration. Plasmon polarization components that are distant from the junction have little effect upon the phase of the field in the junction. However, as the electron beam is rastered out of the junction to larger impact parameters a variety of unusual Fano interference features can be initiated.

The lower six panels of 5.3 display the birth and evolution of a Fano resonance in EELS at position 2 as a function of impact parameter $b_y = 0 - 40$ nm. In particular, between $b_y = 27$ and 30 nm, the plasmon's phase drops rapidly from π down to 0 near 2.70 eV. This is due to the fact that in addition to the locally pinned antibonding arrangement of the plasmon polarization in the vicinity of the junction, there is a more distant polarization component of the Pd monomer that flips its phase to accommodate the super-radiant configuration that is resonant at ~ 2.70 eV. When the beam is close to the junction the electric field scattered from this component is small in comparison to that generated by the locally antibonding plasmon configuration. However, at larger impact parameters, it becomes more important and is responsible for the rapid phase change as well as the corresponding constructive interference of the scattered electric field and resulting Fano interference. Such an electron-driven Fano resonance is inverted with respect to that occurring at position 1 and is absent in optical spectroscopy because it stems from an antibonding plasmon configuration that is optically inaccessible.

5.3.2 Fano resonances in cathodoluminescence spectroscopy

We now turn to the question of what, if any, will be the signatures of Fano interferences in CL and will they be observable in situations where there is no corresponding optically-driven Fano resonance. In order for there to be a CL response, 5.2 dictates that there must be an electron-induced radiative emission of energy carried to the far-field. This means that only plasmon modes that have a net dipole moment will be visible in CL spectra. However,

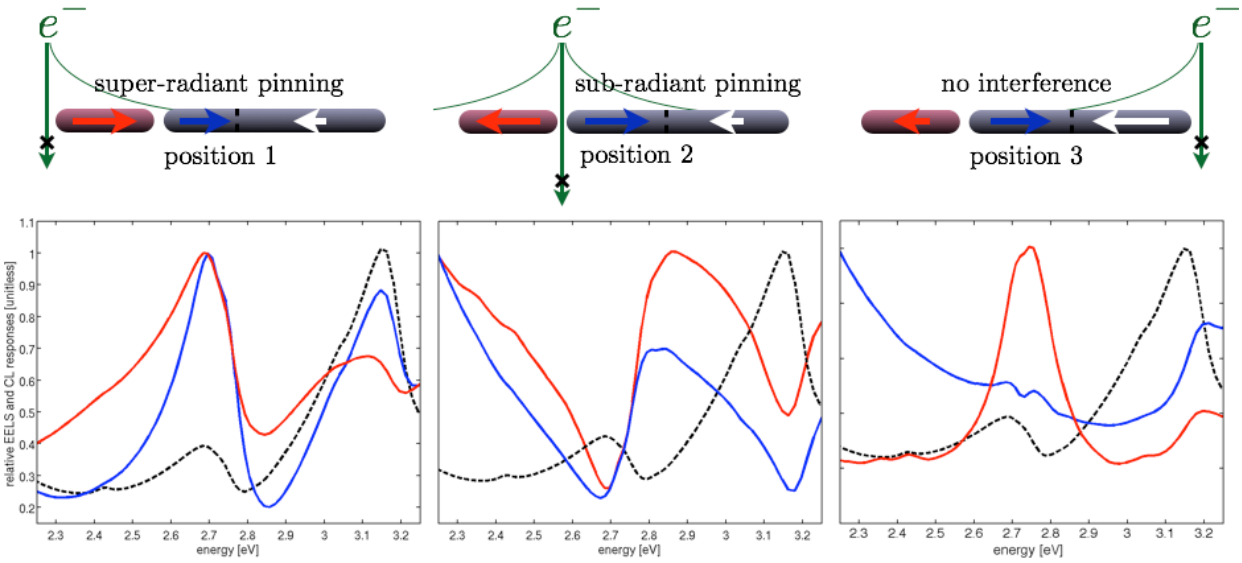

Figure 5.4: CL (blue) and EEL (red) spectra taken from positions 1, 2, and 3 as well as the optical extinction spectrum (dashed black) of the Pd-Ag nanorod dimer. Each curve is normalized so that its maximum takes a value of 1 in each panel. Left panel: At position 1, all three spectroscopies display Fano interferences and encode qualitatively the same information in their spectra. Middle panel: Strikingly different spectra are observed at position 2 at $b_y = 30$ nm, due to the location of the electron beam near the junction. At this position, an antibonding (optically dark) plasmon is responsible for establishing the Fano interference. This new Fano feature is manifested in both EELS and CL, but has no optical analog. Right panel: Due to the distant location of position 3, only the Ag particle is appreciably excited and any phase reorientation of the Pd dipole acts only as a perturbation to the induced electric field of the Ag plasmon. Therefore, no significant interference effect is present in either of the electron spectroscopies.

in the case of the Pd-Ag nanorod dimer studied herein, both of the previously discussed electron-driven Fano interferences involve the excitation of super- and sub-radiant plasmon modes. Both of these hybridized excitations have a net dipole moment and can broadcast electromagnetic energy into the far-field. This means that, in principle, it should be possible for asymmetric Fano line shapes to be observed in CL.

5.4 displays the CL (blue curves) and EEL (red curves) spectra of the symmetry-broken Pd-Ag nanorod dimer displayed in 5.2, corresponding to the positions 1-3 of the electron

beam. Each panel also displays the optical scattering spectrum (black dashed curves) of the same dimer for comparison. Since all three spectra have different units, we have chosen for simplicity to rescale each curve so that its maximum value has a magnitude of 1.

In the left panel of 5.4 corresponding to position 1, the first Fano resonance peak near 2.70 eV is common to all three spectroscopies. It arises from the emission of radiation from the Pd dipole-Ag quadrupole super-radiant plasmon powered by the Pd dipole. All three spectra are qualitatively similar and they encode basically the same information.

This is no longer true when the electron beam is moved to position 2 at the impact parameter $b_y = 30$ nm, as seen in the middle panel of 5.4. There the electron spectroscopies are both capable of exciting the Pd dipole-Ag quadrupole sub-radiant mode with high probability *via* the Ag quadrupole plasmon. Neither of these hybridized plasmons of the dimer (induced by EEL or CL probes) are optically dark, and both may store electromagnetic energy in the near-field and liberate energy to the far-field in the form of radiation. This is why the EEL and CL responses look so similar. Further, this provides a surprising example of an electron-driven Fano interference that is observable in the far-field (through CL) but has no optical signature. To our knowledge this is the first prediction of a new class of Fano resonance that is accessible by the differing selection rules of the electron beam, and that can be selectively excited based on the beam's position.

Lastly, in the right panel of 5.4 corresponding to position 3, there is no significant interference effect in either of the electron spectroscopies. Just as in the case of EELS at position

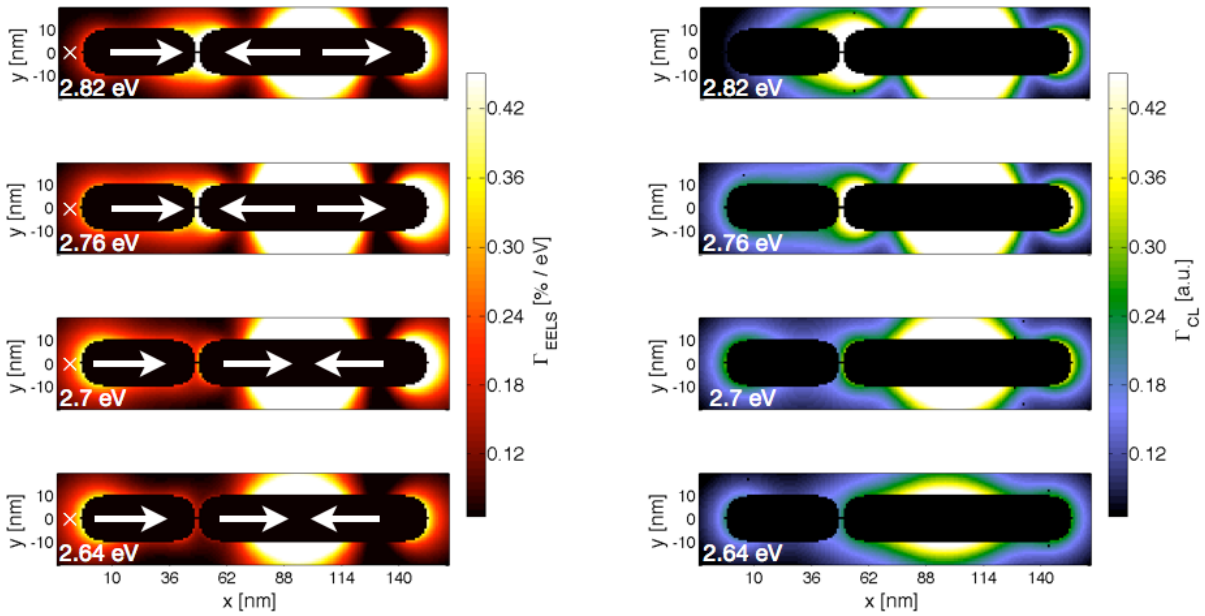

Figure 5.5: EEL probability maps (left column) and CL maps (right column) of the Pd-Ag nanorod dimer computed at the four loss energies indicated by the vertical black dashed lines in 5.2. Regions of high EEL probability correspond to nodes in the plasmon's polarization [60]. The latter is indicated by overlaid white arrows, with a relative phase dictated by the electron beam source located at the × position. The re-orientation of the direction of the underlying monomer plasmons composing the hybridized dimer plasmon as it transitions from super-radiant to sub-radiant character is visible in both the EEL and CL maps.

3, the polarizations of the Ag quadrupole and at lower loss energies the Ag dipole plasmons are pinned by the electron beam, and the induced field generated by either orientation of the distant Pd dipole acts only as a perturbation in both the near- and far-fields. However, since the Ag dipole plasmon scatters a radiation field that is relatively much stronger than those scattered by the super- and sub-radiant (Pd dipole-Ag quadrupole) plasmon modes of the dimer, the latter two plasmon modes appear as small spectral features on the shoulder of the Ag dipole resonance in CL. This differs from the EEL response where the energetically distant Ag dipole does not play as significant of a role in the near-field.

5.4 displayed the spectral correlation between EEL and CL responses across two Fano res-

onances of the Pd-Ag nanorod at three specific spatial electron beam positions. In 5.5, we now present the corresponding spatial correlations between aloof EELS and aloof CL at four specific energies, 2.64, 2.70, 2.76, 2.82 eV, indicated by the vertical black dashed lines in the lower panel of 5.2. The reorientation of the relative direction (or relative phase shift of π) of the underlying monomer plasmons comprising the hybridized dimer plasmon as it transitions from super-radiant to sub-radiant character is clearly visible across this limited spectral range. A set of averaged plasmon polarization vectors (white arrows) are overlaid on the EEL maps corresponding to an electron beam placed at the $\times$ to aid in visualization. Such a phase flip of the plasmon's polarization is distinguished by the increased EEL probability in the dimer junction [60] at higher energies, and is echoed in the CL intensity. This demonstrates that for this system, the two electron-driven spectroscopies are correlated both spatially and spectrally for certain positions of the exciting electron beam.

5.4 Conclusion

Through numerical simulation, we have predicted the signatures of Fano interferences in the EELS and CL of symmetry-broken nanorod dimers that are heterogeneous in material composition and asymmetric in length. The mechanism underlying this electron-driven interference effect is different from that occurring in the optical case: we have discovered that the electron beam of a STEM, depending upon its position, may pin the local orientation of a nanostructure's induced polarization. As a consequence, it is the polarizations of the more distant components that are forced to flip their phase by π to accommodate the hybridized (global) plasmon configuration that is resonant at a given value of the EEL. This polarization

phase flip generates a corresponding interference in the induced electric near- and far-fields that can show up in EELS, CL, and sometimes in optical spectroscopy as Fano interferences. On the basis of these ideas, we have further predicted a new class of Fano resonances that are uniquely electron-driven and are absent in the optical response.

5.5 Methods

5.5.1 Electron energy loss and cathodoluminescence simulations

The coupled-dipole [43] or DDA [47] approach is routinely used to study the response of metal nanoparticles subjected to optical frequency radiation [98]. In our previous work, we developed and numerically implemented the *e*-DDA [60, 100] as a generalization of this approximation, incorporating the electron beam of a STEM in place of a plane-polarized electric field source as is common to the DDA. In the *e*-DDA, the target is discretized into a finite collection of polarizable point dipoles $\mathbf{P}_j$, $1 \leq j \leq N$, each driven by the evanescent electric field

$$\mathbf{E}_{\text{electron}}(\mathbf{x},\omega) = \frac{2e\omega}{v^2\epsilon\gamma} e^{i\omega z/v}\Big[\frac{i}{\gamma}K_0\Big(\frac{\omega b}{v\gamma}\Big)\hat{\mathbf{v}} - K_1\Big(\frac{\omega b}{v\gamma}\Big)\hat{\mathbf{b}}\Big] \tag{5.4}$$

of a passing swift electron as well as by the fully retarded electric dipole field $\sum_{j\neq i}^{N}\mathbf{\Lambda}_{ij}\mathbf{P}_j$ generated by all other points; here $\mathbf{\Lambda}_{ij} = e^{ikr_{ij}}\{(1/r_{ij}^3 - ik/r_{ij}^2)[3\hat{\mathbf{n}}_{ij}\hat{\mathbf{n}}_{ij} - \mathbf{1}_{ij}] - k^2\hat{\mathbf{n}}_{ij}\times(\hat{\mathbf{n}}_{ij}\times)/r_{ij}\}$ is the standard dipole tensor that relays the electric field generated by a dipole at one point in space $\mathbf{x}_i$ to another $\mathbf{x}_j$ a distance $r_{ij}\hat{\mathbf{n}}_{ij} = |\mathbf{x}_i - \mathbf{x}_j|\hat{\mathbf{n}}_{ij}$ away. In this manner,

the electron-induced responses of the system can be computed once each dipole is brought into self-consistency with all others at a certain value of the electron's loss energy, $\hbar\omega$. This is accomplished through the iterative solution of the following equation,

$$\sum_{j=1}^{N}[\boldsymbol{\alpha}_{ii}^{-1}(\omega)\delta_{ij} - (1-\delta_{ij})\mathbf{\Lambda_{ij}}]\mathbf{P}_j(\omega) = \mathbf{E}_{\text{electron}}(\mathbf{x}_i,\omega), \tag{5.5}$$

and depends upon the frequency-dependent linear polarizability $\boldsymbol{\alpha}_{ij}(\omega) \equiv \boldsymbol{\alpha}_{ii}(\epsilon(\omega))\delta_{ij}$ of the target point i. The polarizability is related to the dielectric function through the lattice dispersion relation [99], and includes the effects of radiation reaction [47]. The electric field of the electron [38] in 5.4 depends upon the modified Bessel functions of the second kind K_0 and K_1, the Lorentz contraction factor $\gamma = 1/\sqrt{1-\epsilon(v/c)^2}$, and the dielectric function ϵ of the background medium, which is taken to be vacuum in all calculations. The incident velocity $\mathbf{v} = v\hat{\mathbf{v}}$ of the electron is determined by its incident kinetic energy $m\gamma c^2 - mc^2$, and is oriented along the z axis ($\hat{\mathbf{z}} \parallel \hat{\mathbf{v}}$). We choose the phase $e^{i\omega z/v} = 1$ at the z-height of the mass centroid of the target, which defines the plane of the impact parameter $\mathbf{b} = b\hat{\mathbf{b}}$, with $\mathbf{x} = (\mathbf{b}, z)$ that is perpendicular to the electron beam and that contains this point.

Other approaches to simulating EELS rely on different numerical methods of varying efficiency. The e-DDA benefits from the requirement that only the target need be discretized. The source field of the electron as well as the scattered fields of each target dipole are all known analytically. Finite-element-based methods, such as the COMSOL implementation [94], require both the target and surrounding medium to be discretized into elements, with

all fields and associated boundary conditions represented numerically on the grid. Both approaches should result in the same observable quantities as long as all relevant convergence criteria are met.

All target structures investigated *via* *e*-DDA simulations are excited by a 0.10 MeV electron beam directed normal to the longitudinal axis of the rod; the corresponding velocity of the electrons in the beam is 0.55 c. Only aloof trajectories through vacuum are considered in the simulations and the two-dimensional grid of impact parameters $\mathbf{b}$ for the electron beam is chosen to have a 1 nm spacing. Dielectric data from Johnson and Christy [101] is used for Ag and from the SOPRA database [209] for Pd. An interdipole spacing of 1 nm is used for the target; other dipole spacings were tested to ensure that all spectra are converged at this value.

The most recent version of the *e*-DDA code [100] computes CL spectra and spatial maps in addition to EEL properties. The electron-induced response, $\mathbf{P}_j$, of the target is solved at each spatial position of the electron beam according to 5.5 as in the previous version of our code. However, for CL, at each spatial position of the beam and at each value of the loss energy, the induced electric field $\mathbf{E}_{\text{ind}}$ is computed according to

$$\mathbf{E}_{\text{ind}}(\mathbf{x},\omega) = \sum_{j=1}^{N} \mathbf{\Lambda}(\mathbf{x},\mathbf{x}_j)\mathbf{P}_j(\omega) \tag{5.6}$$

at various points $\mathbf{x}$ in the far-field. For the *e*-DDA based CL calculations performed in this article, $\mathbf{E}_{\text{ind}}$ is computed on an angular grid of points spanning the surface of distant sphere

of radius 5 μm, with 75 points in θ and 75 points in ϕ. In this way, either the differential CL response $d\Gamma_{\mathrm{CL}}/d\Omega$ or, by quadratured solid-angle integration, the total CL response Γ_{CL} may be computed.

5.6 Conflict of interest

The authors declare no competing financial interest.

5.7 Acknowledgements

This work was supported by the University of Washington, the University of Tennessee, the UT/ORNL Joint Institute for Advanced Materials, and the U.S. Department of Energy, Office of Basic Energy Sciences under award number DE-SC0004792 (J.P.C.), and by the National Science Foundation's CAREER program under award number CHE-1253775 (D.J.M.).

Chapter 6

Resonance-Rayleigh Scattering and Electron Energy Loss Spectroscopy of Silver Nanocubes

This work has previously been published in the following article:

V. Iberi, N. W. Bigelow, N. Mirsaleh-Kohan, S. Griffin, P. D. Simmons, B. S. Guiton, D. J. Masiello, and J. P. Camden.

Journal of Physical Chemistry C **118**, 10254 (2014)

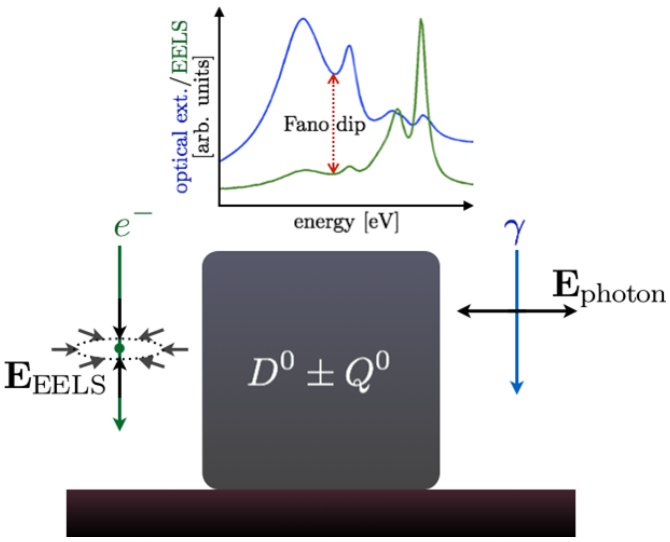

Figure 6.1: Abstract figure.

6.1 Abstract

The Fano interference phenomenon between localized surface plasmon resonances (LSPRs) of individual silver nanocubes is investigated using dark-field optical microscopy and electron energy-loss spectroscopy (EELS) in a scanning transmission electron microscope (STEM). By computing the polarization induced by the electron beam, we show that the hybridized modes responsible for this Fano interference are the same as those present in the resonance-Rayleigh scattering spectrum of an individual nanocube on a substrate.

6.2 Introduction

Metal nanoparticles support collective excitations of their conduction electrons, which are known as localized surface plasmon resonances (LSPRs) [210]. LSPRs can be probed by both far- and near-field excitation sources, including laser light and swift electrons from a scanning transmission electron microscope (STEM) [11, 33]. The field of plasmonics has

experienced rapid growth in the past decade, driven in large part by the ability of metallic nanostructures to manipulate light at subwavelength scales and the high degree of tunability of the LSPRs by modifying the size, shape, and the surrounding dielectric environment of the nanoparticle [98]. When light is concentrated using LSPRs, there is an enhancement in the electric field near the nanoparticle surface, which can be used in various surface-enhanced spectroscopies, chemical catalysis, and other applications [105, 116, 211, 212]. Localized surface plasmon resonances are also utilized routinely in other areas including the detection of single molecules [18–21], optical waveguides [213–216], photonic circuits [217–219], nonlinear spectroscopy [220–225], and solar energy harvesting [12–17], among others.

The recent increase in the diverse applications of LSPRs warrants a fundamental understanding of the optical response of nanostructures based on their geometries and interactions with a local environment, particularly at the single nanoparticle level [226, 227]. Numerous studies on noble metal nanoparticles have correlated optical resonance-Rayleigh scattering with particle structure and continuum electrodynamics simulations [228–236]. These reports emphasized the strong dependence of the LSPRs on nanoparticle geometry; however, direct measurements of the near-field optical response of nanostructures were lacking. Similarly, the effect of a surrounding dielectric environment on LSPRs has been investigated with spectral shifts in the LSPRs due to changes in the refractive index of the substrate being reported [73, 230, 237–239]. STEM with electron energy-loss spectroscopy (EELS) offers a method of probing the near-field response and local dielectric environment of metal nanoparticles with subnanometer spatial resolution [11, 90, 198]. The emergence of STEM with EELS [11, 77, 240–242] or energy-filtered TEM (EFTEM) [37, 243], as an unprecedented tool for directly

mapping plasmon modes in metal nanostructures with subnanometer resolution, has fostered a deeper understanding of the near- and far-field effects in plasmonic systems.

More recent studies have reported the manifestation of Fano resonances in plasmonic nanostructures when excited by light [73, 244–246]. This phenomenon occurs as a result of the coupling and interference between optically bright and dark modes due to symmetry breaking [28, 73]. The energetically narrow spectral features found in Fano resonances make them attractive in areas such as refractive index [196] and molecular sensing [246], particularly due to the absence of radiative damping in the subradiant modes. While most Fano interference studies have involved optical techniques such as dark-field optical microscopy, the observation of this phenomenon in STEM/EELS is still lacking and not well understood. To date, only cathodoluminescence (CL) spectroscopy, in which a focused electron beam is used as an excitation source, has been used to investigate Fano resonance signatures in certain plasmonic systems [71, 247]. It has been shown that under electron beam excitation Fano interferences were not observed in these systems. More recently, however, Masiello and co-workers have predicted the signatures of electron-driven Fano resonances in CL and EELS in symmetry-broken nanorod dimers that are heterogeneous in material composition and asymmetric in length [67].

In this article, we apply a combination of dark-field optical microscopy and STEM/EELS [82, 89] to the investigation of the LSPR properties in individual silver nanocubes. Single nanocubes have been chosen in this study due to their already well-characterized plasmonic and optical Fano resonances [73, 229, 230, 247–250]. Our observations are supported with fully

three-dimensional continuum electrodynamics simulations using plane wave and electron beam excitations. Our simulations and experiments indicate that Fano interferences are present within the nanocube-substrate configuration and can be excited with EELS.

6.3 Methods

6.3.1 Dark-field optical scattering experiment.

Samples were prepared using a method described previously [82]. Briefly, a 3 μL aliquot of silver nanoparticle colloids was drop-coated onto a copper TEM grid coated with 10-20 nm of amorphous carbon (SPI supplies # 3520C-CF). Resonance-Rayleigh scattering measurements were performed on a series of individual particles using an inverted microscope (Nikon, Ti-U) equipped with a dark-field condenser (Nikon, NA = 0.95-0.80). The excitation source was unpolarized light from a tungsten-halogen lamp. Scattered light from an individual nanoparticle was collected with a 100 $\times$ objective (Nikon, 0.7 $<$ NA $<$ 1.4, oil immersion) and coupled into a dispersive imaging spectrometer (Acton Research, f = 0.3 m) using a f = 5.0 cm lens. Light was detected on a liquid nitrogen-cooled back-illuminated charge coupled detector (CCD) (Princeton Instruments, PIXIS 100). The dark-field scattering spectrum of each individual nanocube was obtained using a 150 grooves/mm grating with a 500 nm blaze. A wide-field image of the silver nanoparticles on the TEM grid was also recorded to serve as a map for subsequent location in the STEM. This method enabled correlated optical and STEM measurements from the same nanostructures [251]

6.3.2 STEM/EELS experiment.

STEM/EELS experiments were performed on a Carl Zeiss LIBRA 200MC field emission transmission electron microscope equipped with a monochromator and operating at 200 kV. The electron source was a Schottky emitter, and the monochromator was integrated in the field emission gun to form an omega-type imaging element. This special design of the monochromator eliminated second order chromatic aberrations and also made it suitable for STEM/EELS under the operating conditions. The nanocubes of interest were found by comparing the optical maps to the pattern of particles imaged in the STEM at very low magnification. After correctly identifying each nanocube with an optically-measured LSPR spectrum, a high resolution high angle annular dark field (HAADF) image was recorded. EEL spectra were obtained at each pixel over the entire region of interest with a dispersion of 0.05 eV per channel and a dwell time of 0.05 s per pixel. The pixel size density used for collecting each spectrum image (SI) resulted in a total acquisition time of 12 min per SI. The energy resolution for each SI, determined by the full width at half-maximum (fwhm) of the zero loss peak (ZLP), was 0.19 eV. Experimental STEM/EELS data from each nanocube were analyzed using DigitalMicrograph imaging software by Gatan Inc. Briefly, a pixel of interest from the SI of the nanocube was selected and the corresponding full energy loss spectrum was obtained. The ZLP of the EEL spectrum was fit to a Gaussian and Lorentzian and centered at 0 eV, with each EEL spectrum normalized to the ZLP before subtraction. The deconvoluted EEL spectrum was truncated to a region (2.0-4.0 eV) corresponding to the measured Rayleigh scattering spectra of the nanocubes in order to fully compare the resonances from both excitation sources. The Automated eXpert Spectral Image Analysis

(AXSIA) program developed by Keenan and co-workers [134] was used in order to extract and interpret the plasmon modes which overlap spectrally and spatially. Furthermore, the application of multivariate statistical analysis (MVSA) to the experimental EELS data ensured the reduction of nonuniform noise in the spectrum image while the principal component analysis (PCA) in Automated eXpert Spectral Image Analysis (AXSIA) produced the plasmon modes and corresponding spectra [82].

6.3.3 Simulations.

The coupled-dipole approximation [43] or discrete-dipole approximation (DDA) [47] approach has been routinely used to study the response of metal nanoparticles subjected to electromagnetic radiation [98]. In this paper, plane wave spectra and the associated scattered electric fields and target polarizations are computed via the DDA [47]. Electron energy loss spectra (EELS), the resulting scattered electric fields, and target polarizations are generated through the recently developed electron-driven discrete-dipole approximation (e-DDA) [60, 100]. The structure of the computed cubes is adjusted within the experimental measurement error to best fit the computed far-field scattering spectrum to the experimental results. The corner radii are within the variation of the observed radii for the cube being modeled, and the height of the cube, while not observed directly, is within the observed deviation from cubic of other synthesized cubes in the same batch. The two lowest energy plasmonic modes of the cube on a substrate are hybrid modes constructed from linear combinations of dipole ($\mathbf{D}^0$) and quadrupole ($\mathbf{Q}^0$) modes of the cube in vacuum [73]. In order to determine the phase and

relative magnitude of either the fundamental or hybridized modes, the target polarizations, $\mathbf{P}(\omega)$, are computed and then projected onto the appropriate eigenvectors associated with each mode

$$c_a(\omega) = \langle \hat{\mathbf{n}}_a | \mathbf{P}(\omega) \rangle \tag{6.1}$$

$$\mathbf{a} = \mathbf{D}^0,\ \mathbf{Q}^0,\ \mathbf{D}^0 \pm \mathbf{Q}^0 \tag{6.2}$$

where c is the projection amplitude. For plane wave excitation, the primitive dipolar normal vector ($\hat{\mathbf{n}}_{\mathbf{D}^0}$) points in the opposite direction of the polarization of the driving electric field. The plane wave-driven primitive quadrupolar normal vector ($\hat{\mathbf{n}}_{\mathbf{Q}^0}$)points parallel to the polarization of the driving electric field in the upper half of the cube and antiparallel in the bottom half. For electron-beam excitation, the primitive dipolar normal vector points radially outward from the line path of the electron. The EELS primitive quadrupolar normal vector points radially outward from the line path of the electron in the upper half of the cube and radially inward in the lower half. All normal vectors are idealized abstractions of the modes they represent, and projections onto them are therefore qualitative, but not quantitative. The polarization of the substrate is not explicitly treated by this mode projection analysis, but its effects are implicitly accounted for in all calculations. The hybridized normal vectors for both optical and electron-driven cases follow in a manner consistent with the primitive normal vectors, with the exception of the cube on a substrate calculations, in which the separation between the $\mathbf{D}^0 \pm \mathbf{Q}^0$ polarization vectors is moved from 0.5 to 0.65

times the cube height to better reflect the asymmetry of that cube system. Projections onto the cube on a substrate also use a basis in which $0.7\mathbf{D}^0 + \mathbf{Q}^0$ and $\mathbf{D}^0 - 0.7\mathbf{Q}^0$ better reflect the incomplete coupling between the $\mathbf{D}^0$ and $\mathbf{Q}^0$ modes in the modeled system.

6.4 Results and discussion

6.4.1 Correlated studies of individual silver nanocubes.

The plasmonic properties of silver nanocubes are characterized using dark-field optical microscopy and STEM/EELS (see Methods section) although the discussion here will be limited to a single nanocube. Structural parameters for each cube such as edge lengths and radius of curvature have been obtained from the HAADF images in a STEM. 6.2 shows the overlaid experimental (red trace) and theoretical (black trace) spectra obtained using plane wave and electron beam excitations, from the exact same nanocube whose corresponding HAADF image is shown in the inset. The experimental and theoretical optical scattering spectra (left panel) highlight the characteristic optical response of a silver nanocube on a substrate under plane wave excitation and are in excellent agreement with each other and with previous studies [229, 230, 248]. In the optical scattering spectra, the peak at ∼2.3 eV is attributed to the hybridized bonding mode, $\mathbf{D}^0 + \mathbf{Q}^0$, between the primitive dipolar ($\mathbf{D}^0$) and quadrupolar ($\mathbf{Q}^0$) modes of the cube in vacuum while the peak at ∼2.8 eV corresponds to the hybridized antibonding mode, $\mathbf{D}^0 - \mathbf{Q}^0$. Hybridization between the $\mathbf{D}^0$ and $\mathbf{Q}^0$ modes occurs in the presence of a substrate, as evidenced by the dip at ∼2.7 eV in the optical scattering spectra, which lowers the symmetry of the plasmonic system and can be inter-

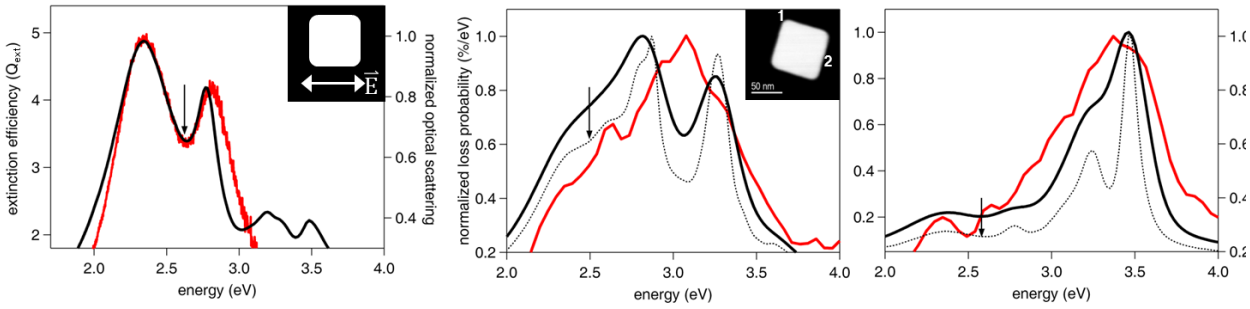

Figure 6.2: Comparison of the experimental (red trace) and computed (black trace) spectra obtained using plane wave light and electron beam excitation for a single silver nanocube (HAADF image in inset). Left panel: resonance-Rayleigh scattering spectrum of a silver nanocube (schematic diagram indicating the polarization of the incident electric field in inset). Middle and right panels: electron energy loss (EEL) spectrum obtained from the corner (position 1) and edge (position 2) of the same nanocube. Solid black trace in the EEL spectra was obtained by convolving each point in the computed EEL spectra (dotted black trace) with a Gaussian function with a full width at half-maximum of 0.19 eV. Black arrows in the three panels indicate the position at which the $\mathbf{D}^0 + \mathbf{Q}^0 \rightarrow \mathbf{D}^0 - \mathbf{Q}^0$ Fano interference occurs in the simulations.

preted as a substrate-induced Fano resonance [73]. Moreover, the splitting and relative peak intensities in the optical scattering spectrum are known to be strong functions of the spacing between the cube and the substrate [248]. The higher energy modes (3.2 and 3.5 eV) present in the theoretical scattering spectrum are beyond the energy range of our spectrometer and hence are not observed experimentally.

In 6.2, the experimental EEL spectra (red trace, middle and right panel) are extracted from two different positions (1 and 2 in HAADF image inset) on the nanocube although the STEM/EELS procedure involved raster-scanning the electron beam over the entire nanocube. This was done in order to investigate the spectral dependence of the plasmon resonance on the position of the electron beam. The EEL probability spectra computed at the two

beam positions are indicated by the dotted black trace. In order to best compare to the STEM/EELS experiment, each point in the computed EEL spectra was convoluted with a Gaussian function with a full width at half-maximum (fwhm) of 0.19 eV, corresponding to the energy resolution of the ZLP in the STEM/EELS experiment (solid black trace). While the computed and experimental EEL spectra at the corner and edge of the cube are in good agreement, the absence of the large dip in the experimental EEL spectrum at position 1 at ∼3.1 eV may be due to an overlap between plasmon modes which is evident by the shoulder at ∼3.2 eV in the experimental EEL spectrum.

Utilizing a correlated approach in the study of the LSPR properties of silver nanocubes facilitates the investigation of Fano interferences with STEM/EELS since the optical scattering spectrum provides information on where this interference is likely to occur. In the resonance-Rayleigh scattering spectrum, the dip at 2.6 eV indicated by a black arrow is due to a Fano interference corresponding to the local minimum at ∼2.5 eV in the experimental EEL spectrum at positions 1 and 2. Even without any sophisticated post STEM/EELS experimental data processing, the ability to resolve such a feature highlights the significance of obtaining EEL spectra at high energy resolution [208, 252]. In the computed EEL spectra, a similar feature at 2.6 eV (indicated by black arrow) is present at both electron probe positions; however, this feature is more pronounced when the probe is at position 2. This suggests that the efficiency of the coupling between the $\mathbf{D}^0$ and $\mathbf{Q}^0$ modes depends on the position of the probe and will be discussed subsequently.

6.4.2 investigation of Fano interference in STEM/EELS.

In 2005, Schatz and co-workers examined [230] the behavior of the quadrupole peak on the shoulder of the cubes dipole plasmon resonance as a function of its separation distance from the substrate. The cube was large enough for the quasistatic approximation to fail. The substrate and vacuum localization of the resulting hybridized plasmon resonances were adiabatically connected to the cubes fundamental modes away from the substrate. In 2011, Nordlander and co-workers [73] interpreted the two lowest lying peaks in the spectrum of a small cube on a substrate (within the quasistatic limit) as the hybridized modes, $\mathbf{D}^0 \pm \mathbf{Q}^0$, with the dip between them being attributed to a Fano resonance. Because of the smallness of the cube, the quadrupole plasmon was only excited through its substrate-mediated hybridization with the dipole plasmon.

The large and rounded cubes appearing in our study drive us to investigate a parameter space that is between both of these previous works. More specifically, we investigate the plasmon physics occurring within a cube that is large enough to support a dipole and quadrupole plasmon even in vacuum when driven by light. In this case the phase retardation causes significant excitation of the vacuum cubes quadrupole plasmon. This leads to an optical spectrum that is qualitatively indistinguishable from the optical spectrum of a cube on a substrate. However, the former lacks the hybridization and accompanying Fano interference of the latter. Here we examine how to differentiate between these two similar-looking spectra in case where the quasistatic approximation breaks down.

We can understand the Fano effect in the cube on a substrate by attaching a phase, $\phi(\omega)$, to the $\mathbf{Q}^0$ mode relative to the $\mathbf{D}^0$ mode as a function of excitation energy so that we may write the contribution from the two fundamental modes as a function of energy as

$$\mathbf{P} = \mathbf{D}^0 + \mathbf{Q}^0 e^{i\phi(\omega)} \tag{6.3}$$

where $\mathbf{P}$ is the overall target polarization and $\mathbf{D}^0$ and $\mathbf{Q}^0$ are the full vector-valued representations of the modes they represent. The Fano resonance occurs when ϕ crosses $\pi/2$, where the hybridization switches from a bonding to an antibonding arrangement.

6.3 shows the optical extinction spectra for both a perfect cube (side length = 80 nm, corner and edge radius of curvature = 10 nm) in vacuum (first column) and the imperfect (symmetry-broken) cube on a substrate (second column) used to model the experimental data. For the perfect cube in vacuum, both the dipole and quadrupole are excited by far-field radiation and are seen in the extinction spectrum. As the symmetry of the cube is broken along the wave vector of light, by either the presence of the substrate or deformation (e.g., through asymmetric corner and edge rounding) or a combination of both, the dipole and quadrupole modes hybridize to form $\mathbf{D}^0 \pm \mathbf{Q}^0$ modes, which give an extinction spectrum that looks qualitatively like that of the perfect cube in vacuum. In order to distinguish between the two spectra, we recognize that the primitive $\mathbf{D}^0$ and $\mathbf{Q}^0$ plasmon modes form an orthogonal eigenbasis for the perfect cube in vacuum, while the hybridized $\mathbf{D}^0 \pm \mathbf{Q}^0$ modes form an orthogonal eigenbasis for the cube on a substrate. Just as the hybridized plasmons

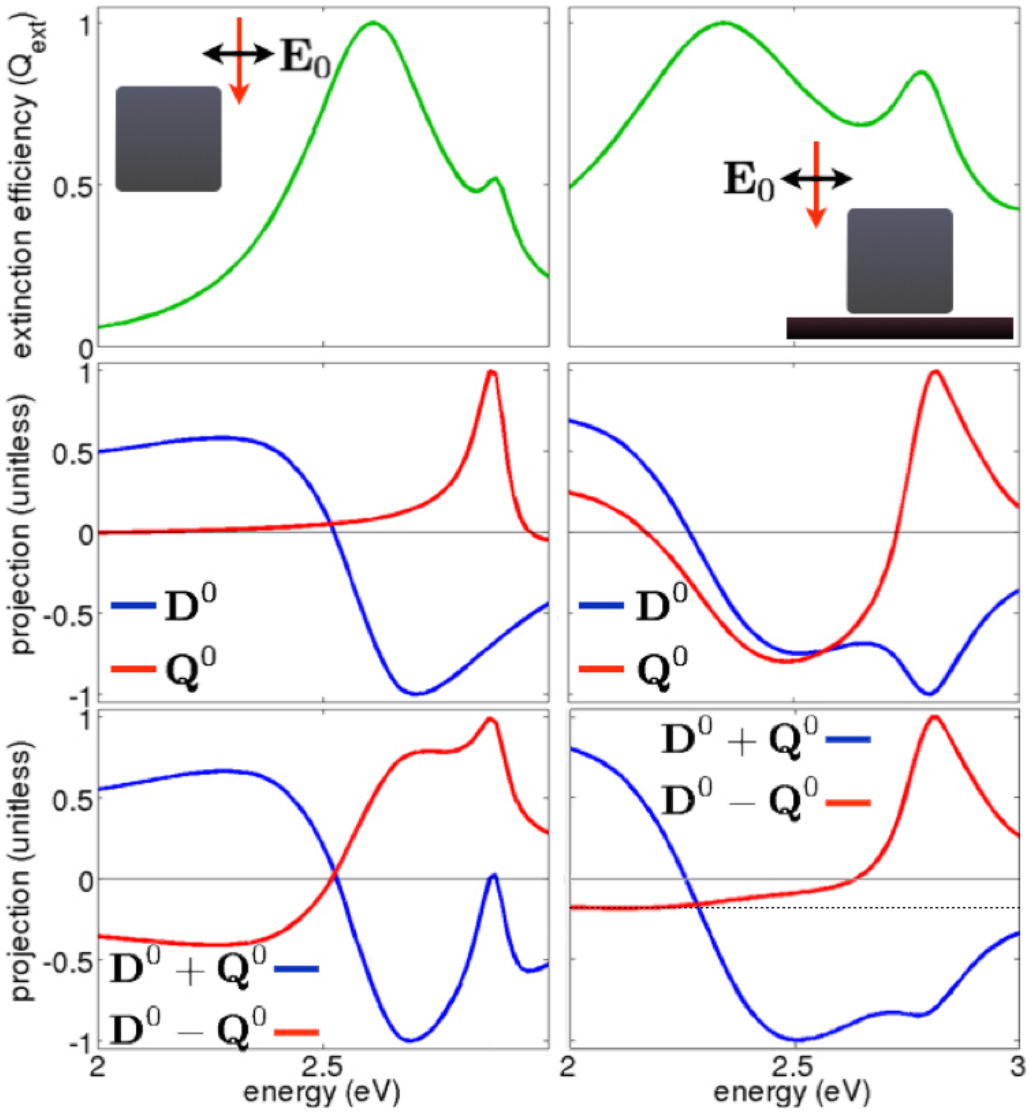

Figure 6.3: Optical extinction spectra and polarization phase plots corresponding to the optical excitation of a large cube both in vacuum (left) and on a substrate (right) in the non-quasistatic limit. The left column presents data for a perfect cube, while the right column presents data for the same cube (with asymmetrically rounded corners and edges) used in this paper to model experiment. The optical spectra (top panels) of both look qualitatively the same and without performing a phase analysis it is unclear if the dip between the spectral peaks is due to a Fano interference or simply the damped oscillations of two uncoupled resonances. The appropriate basis must be chosen before the underlying physics is apparent. For the cube in vacuum (left column) the relative phase flips by π in the $\mathbf{D}^0$, $\mathbf{Q}^0$ basis (left middle panel) in the spectral region between the peaks. While for the cube on a substrate (right column) the relative phase flips by π in the $\mathbf{D}^0 \pm \mathbf{Q}^0$ basis (right lower panel) in the spectral region between the peaks. Since the $\mathbf{D}^0 \pm \mathbf{Q}^0$ basis is not well-defined in the absence of the substrate, it is the latter phase signature that is consistent with the Fano interference mechanism. The dotted line in the bottom right panel highlights the small departure from the zero polarization line for the $\mathbf{D}^0 - \mathbf{Q}^0$ projection, which is attributable to the use of idealized normal vectors and incomplete hybridization between the fundamental modes in vacuum. See text for details.

are constructed from fundamental plasmons, the opposite is also true:

$$\frac{1}{2}[(\mathbf{D}^0 + \mathbf{Q}^0) + (\mathbf{D}^0 - \mathbf{Q}^0)] = \mathbf{D}^0 \tag{6.4}$$

$$\frac{1}{2}[(\mathbf{D}^0 + \mathbf{Q}^0) - (\mathbf{D}^0 - \mathbf{Q}^0)] = \mathbf{Q}^0 \tag{6.5}$$

To distinguish whether the extinction spectrum is the result of two uncoupled primitive plasmon modes or a hybrid system displaying a Fano interference, in 6.3 we project the polarizations arising from the optical excitation of both the cube in vacuum and the symmetry-broken cube on a substrate onto both basis sets. If the appropriate basis to describe the spectrum is the fundamental basis, then the modes will appear as two uncoupled oscillators with a relative phase flip by π between $\mathbf{D}^0$ and $\mathbf{Q}^0$ modes occurring between the dipole and quadrupole peaks. If not, then the relative phase will change by π between the two hybridized (and equally uncoupled) $\mathbf{D}^0 + \mathbf{Q}^0$ and $\mathbf{D}^0 - \mathbf{Q}^0$ oscillators between the superradiant $(\mathbf{D}^0 + \mathbf{Q}^0)$ and subradiant $(\mathbf{D}^0 - \mathbf{Q}^0)$ peaks. These are the natural bases to interpret and identify the physics underlying each spectrum. Even though both spectra look qualitatively the same, the physics underlying the dip between the two lowest lying peaks is different. When viewed in the wrong basis, the projection coefficients are more complicated to interpret but are completely consistent with the transformations between them. The middle (bottom) row of panels in 6.3 projects the energy-dependent cube polarizations onto the $\mathbf{D}^0$, $\mathbf{Q}^0$ $(\mathbf{D}^0 \pm \mathbf{Q}^0)$ basis. For the cube in vacuum, the $\mathbf{D}^0$, $\mathbf{Q}^0$ basis describes the physics as two uncoupled oscillators. The primitive dipole projection (blue) is in phase with the driving

field at frequencies below the dipole resonance and then flips by π above the resonance. The primitive quadrupole projection (red) remains in phase with the driving field up to the spectral location of the quadrupole resonance, where it flips its phase by π. The differing relative phase in polarization between these two low-lying peaks is the reason for the spectral dip between them. For the cube on a substrate, the pattern is the opposite. In the spectral range between the two lowest lying peaks the relative phase changes by π only in the hybridized $\mathbf{D}^0 \pm \mathbf{Q}^0$ basis. This basis would not be well-defined in the absence of the substrate, even though both $\mathbf{D}^0$ and $\mathbf{Q}^0$ plasmon modes separately exist in this non-quasistatic limit. It is the phase flip by π of the cubes polarization in this hybridized basis that is the signature of a Fano interference, whether induced by light or by an electron beam source.

Coupling between a bright and dark mode is essential for the observation of Fano resonances. With a STEM electron beam, the selection rules governing the excitation of LSPRs enable the excitation of both bright and dark modes and might hinder the direct observation of this interference. However, the strong spatial dependence of the evanescent electric field of the passing electron suggests the possibility of an interference between a mode excited close to the electron beam and another mode excited outside its influence [67]. While the substrate-mediated interaction between the $\mathbf{D}^0$ and $\mathbf{Q}^0$ modes under plane wave excitation has been shown to be a Fano resonance [73], no experimental work has of yet shown whether such a resonance will exist under electron-beam excitation.

To extract relative phase data from the computed polarizations, we have projected the simulated data onto the primitive dipole and quadrupole model normal vectors (see Methods).

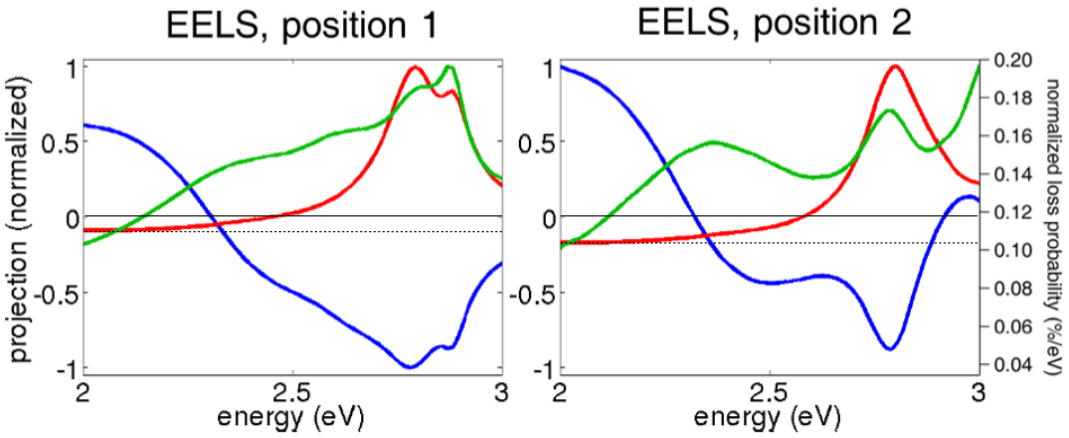

Figure 6.4: Investigation of Fano interferences using the projection coefficients $c_{\mathbf{D}^0+\mathbf{Q}^0}(\omega)$ (blue trace) and $c_{\mathbf{D}^0-\mathbf{Q}^0}(\omega)$ (red trace) of the $\mathbf{D}^0+\mathbf{Q}^0$ and $\mathbf{D}^0-\mathbf{Q}^0$ modes under electron-beam excitation. The Fano interference occurs where the relative phase crosses $\phi = \pi/2$ at 2.7 eV, where the amplitude of the $\mathbf{D}^0 - \mathbf{Q}^0$ hybrid mode grows considerably. The computed optical scattering spectrum has been used to correlate the position where the Fano interference occurs (2.7 eV). Left and right panels: projection coefficients with computed EEL spectra obtained at the corner and edge of the nanocube, respectively. Slight deviations from zero for $c_{\mathbf{D}^0-\mathbf{Q}^0}(\omega)$ at low energies in both plots and positive deviation for $c_{\mathbf{D}^0+\mathbf{Q}^0}(\omega)$ for position 2 at high energies are due to $\hat{\mathbf{n}}_{\mathbf{D}^0+\mathbf{Q}^0}$ and $\hat{\mathbf{n}}_{\mathbf{D}^0-\mathbf{Q}^0}$ being idealized and thus nonquantitative in addition to the incomplete hybridization of the $\mathbf{D}^0$ and $\mathbf{Q}^0$ modes (see text for details). Dotted horizontal lines in both panels show the deviation below the zero line of the $\hat{\mathbf{n}}_{\mathbf{D}^0-\mathbf{Q}^0}$ projection.

6.4 shows the projection coefficients $c_{\mathbf{D}^0+\mathbf{Q}^0}(\omega)$ and $c_{\mathbf{D}^0-\mathbf{Q}^0}(\omega)$, for the $\mathbf{D}^0 \pm \mathbf{Q}^0$ modes as a function of excitation energy for both plane wave and electron beam excitations. The blue and red traces in all three cases correspond to $c_{\mathbf{D}^0+\mathbf{Q}^0}(\omega)$ and $c_{\mathbf{D}^0-\mathbf{Q}^0}(\omega)$, respectively. The green trace corresponds to the computed EEL spectra and has been included for comparison. Under plane wave excitation (6.3), $\mathbf{D}^0 \pm \mathbf{Q}^0$ behaves as nearly uncoupled oscillators, and a phase shift to large positive values of $c_{\mathbf{D}^0-\mathbf{Q}^0}(\omega)$ occurs around 2.7 eV. In 6.4, a similar phase line shape is observed and a corresponding phase shift away from 0 is seen in $c_{\mathbf{D}^0-\mathbf{Q}^0}(\omega)$, indicating the presence of a Fano interference in the EEL spectra as well. Similarly, a corresponding relative phase shift occurs in STEM/EELS close to 2.7 eV, again suggesting a Fano resonance. These results are in excellent agreement with the computed substrate- and vacuum-localized scattered electric fields computed just lower and higher in loss energy from the phase flip (6.6). However, the phase shift is less pronounced in both edge and corner EEL spectra, indicating that the Fano interference, while present, will be much more subtle in the EEL spectrum than in the plane wave spectrum. We believe this to be due to the electron beams capability to excite both the quadrupole and the dipole, though at different oscillator strengths depending on the location of the electron beam. By driving both the $\mathbf{D}^0$ and $\mathbf{Q}^0$ modes with the incident electric field to an extent, the phase shift in EELS is reduced compared to plane wave excitation and the Fano effect becomes smaller. It is also worth noting that a Fano effect is enhanced in cubes without rounded corners [73].

6.4.3 Plasmon and EEL probability maps of silver nanocubes.

6.5 presents the experimental and computed EEL probability maps of the same nanocube. The experimental spectrum images (left panel) and normalized loading spectra (middle panel) were extracted using the MVSA and AXSIA program [134]. This method has been used previously in the extraction and interpretation of plasmon modes with high spectral and spatial overlap [82, 89]. The extracted eigenmodes at 2.2, 2.7, and 3.1 eV exhibit a similar spatial profile in which the intensity is localized at the corners of the cube while the eigenmode at 3.5 eV has an edge-localized spatial profile. The EEL probability maps (right panel) were computed for energies corresponding to the peaks in the theoretical EEL spectra (6.2, middle and right panels) for comparison. Knowledge of the spectral positions of the superradiant (2.3 eV) and subradiant (2.8 eV) hybridized plasmon modes obtained from the optical scattering spectrum in 6.2 enabled us to directly correlate the energies that correspond to the same plasmon eigenmodes in 6.5 (2.2 and 2.7 eV). However, discerning the three-dimensional profile of the hybridized plasmon modes, which have identical spatial profiles when projected onto the plane perpendicular to the motion of the electron beam, was done only by computational means since our STEM/EELS experiment only gathers two-dimensional loss probability information (6.5). A recent report by Nicoletti et al. has demonstrated the ability to obtain three-dimensional plasmon maps in silver nanocubes with electron tomography [253].

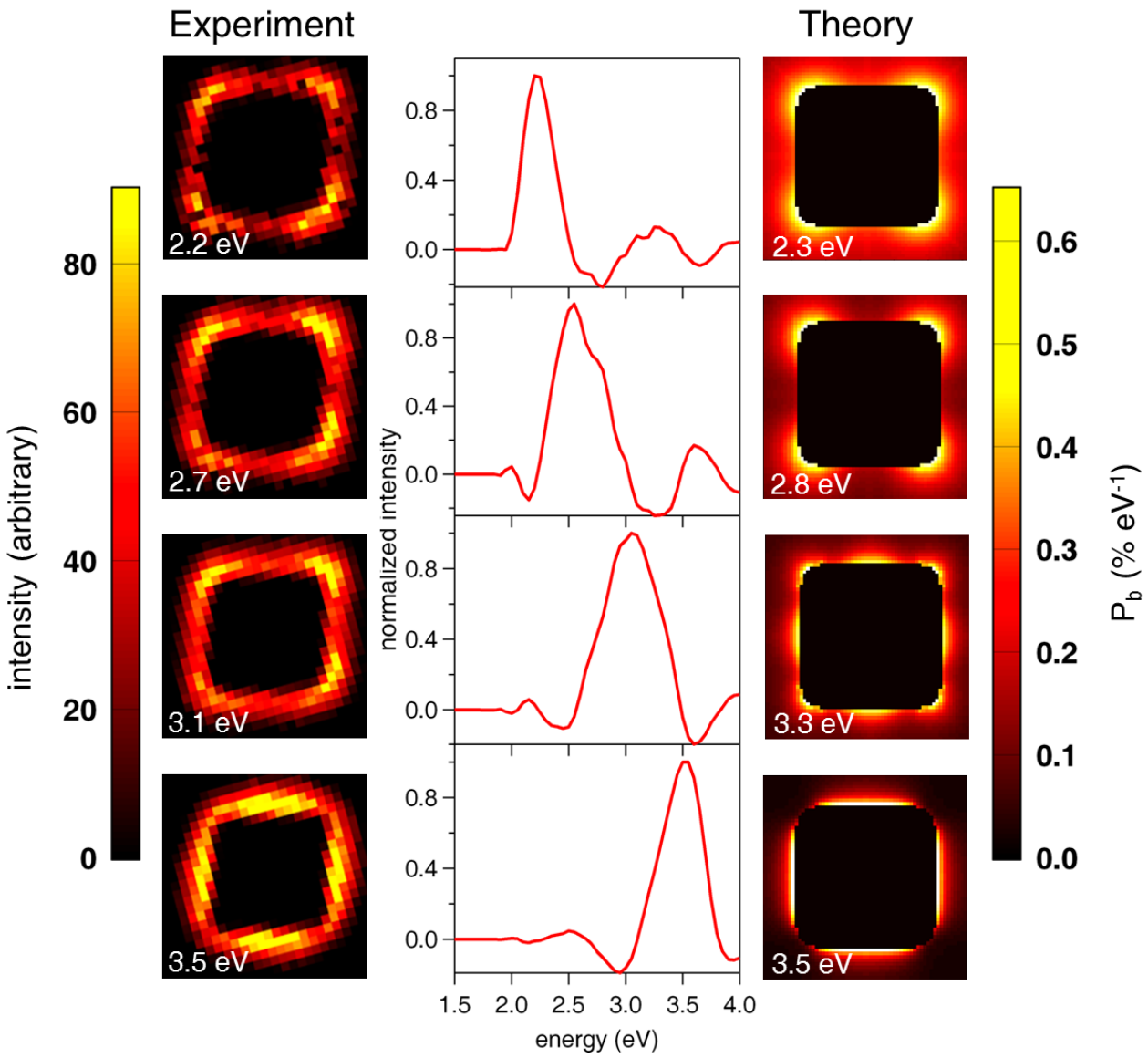

Figure 6.5: Top-down plasmon maps and computed EEL probability maps of a silver nanocube. Left panel: experimental EEL spectrum image components derived using MVSA and AXSIA. Middle panel: corresponding loading spectra for each spectrum image component, interpreted as the energy of each plasmon mode. Right panel: computed EEL probability maps indicating spatial regions on the nanocube where there is high electron energy loss probability.

6.4.4 Identification of vacuum- and substrate-localized hybridized modes.

6.6 shows the computed scattered electric fields of the two lowest-energy modes, in which the vacuum and substrate localizations of the electric fields are investigated for both plane wave and EELS for two different electron-beam positions. Under plane wave excitation, the substrate-localized electric near-field (6.6, left panel, top) arises from the hybridized plasmon mode formed from the constructive superposition of the primitive dipolar ($\mathbf{D}^0$) and quadrupolar ($\mathbf{Q}^0$) plasmon modes, $\mathbf{D}^0+\mathbf{Q}^0$. On the otherhand, the vacuum-localized electric near-field (6.6, right panel, top) corresponds to the hybridized mode that originates from the destructive superposition of the primitive modes, $\mathbf{D}^0 - \mathbf{Q}^0$ [73].

In the electron-beam excitation scenario (6.6, middle and bottom rows), the field maps show two spatial profiles that correspond to the $\mathbf{D}^0 + \mathbf{Q}^0$ and $\mathbf{D}^0 - \mathbf{Q}^0$ hybridized modes at 2.34 and 2.8 eV obtained under plane wave excitation. For the $\mathbf{D}^0 + \mathbf{Q}^0$ mode, the spatial profiles of the scattered near-electric fields show a highly localized intensity at the cube-substrate interface for the two electron-beam positions. While the intensity is localized at the interface, there are small differences in spatial profile of this hybridized mode as the electron beam is moved from the corner to the edge of the cube. This is due to the induced polarizations in the target from the electron beam giving rise to the scattered fields that depend on the position of the electron probe relative to the target. Similarly, the $\mathbf{D}^0 - \mathbf{Q}^0$ hybridized mode shows a highly localized intensity at the top of the cube for both excitation sources. The significant correspondence between these plane wave and EELS hybridized plasmon modes

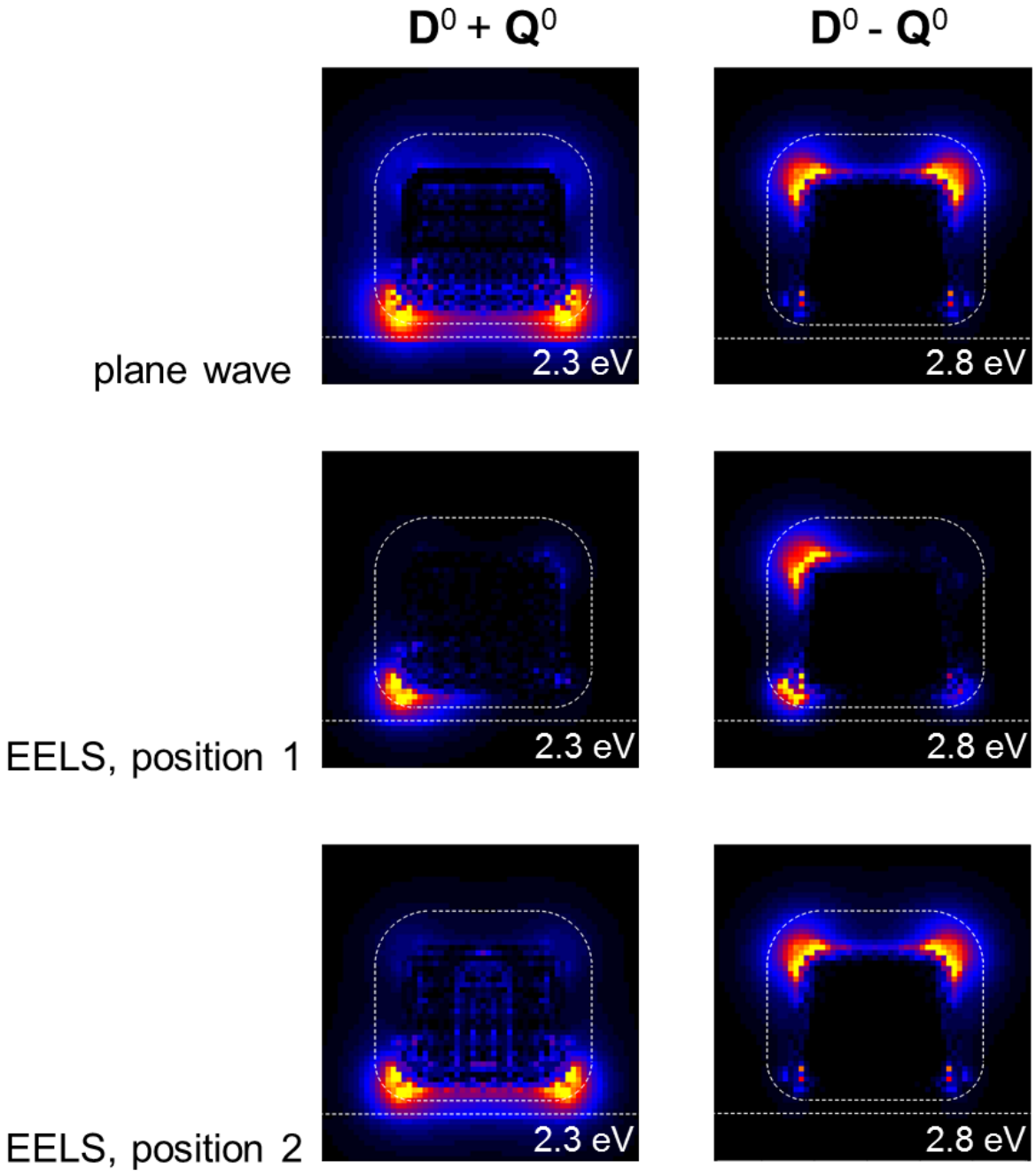

Figure 6.6: Scattered near-electric fields of hybridized plasmon modes in a silver nanocube on a substrate (dashed line). Left panel: substrate-localized plasmon mode for plane wave (top) and electron-beam excitations (middle and bottom), corresponding to the constructive interference of the hybridized primitive dipolar ($\mathbf{D}^0$) and quadrupolar ($\mathbf{Q}^0$) plasmon modes. Right panel: vacuum-localized plasmon modes corresponding to the destructive interference of the $\mathbf{D}^0$ and $\mathbf{Q}^0$ plasmon modes. The plane in which the electric field is evaluated lies outside the cube by 1 nm, parallel to the front face of the cube, perpendicular to the substrate.

suggests that a Fano interference that has the exact same mechanism as that of a plane wave is induced by the electron beam.

6.4.5 Changes in local dielectric environment.

A recent EELS study of silver nanocubes by Mazzucco et al. suggested highly local effects on the LSPR [85]; however, a comparison of the experimental optical scattering spectra for the nanocubes was lacking despite the known strong dependence of the optical spectra on the local dielectric environment. The change in the optical LSPRs after STEM/EELS, recently highlighted in a perspective article [254], suggests that the dielectric environment has been drastically altered by the electron beam. Furthermore, the stretching of the LSPRs differs from previous studies on silver nanocubes which reported red-shifts of both peaks in the LSPRs as the refractive index of the substrate was increased [73, 230]. These effects suggest a possible reason for the weak observation of the Fano interferences in this study.

6.5 Conclusion

Through a correlated approach we have predicted and observed for the first time the subtle Fano interference in silver nanocubes with STEM/EELS. The presence of a substrate mediates the hybridization of the primitive dipolar and quadrupolar modes present in the silver nanocube in both optical and STEM/EELS experiments. By computing the polarization phase-flip from a relative phase of 0 to $\pi/2$ induced by the electric field of the electron probe, we have shown that the hybridized modes responsible for this interference are the same as those present in optical spectroscopy. Furthermore, we have highlighted the drastic

changes that occur in the optical LSPRs of silver nanocubes after exposure to the electron beam. As efforts to understand the detailed connection between optically driven and EELS-derived plasmons in complex nanostructures continue, a correlated approach, along with sophisticated data analysis and simulations, will be essential.

6.6 Acknowledgements

This work was supported by University of Tennessee (UT) Office of Research, College of Arts and Sciences, and Department of Chemistry, the UT/ORNL Joint Institute for Advanced Materials, and the U.S. Department of Energy, Office of Basic Energy Sciences, under Award DE-SC0010536 and the U.S. National Science Foundation under Award CHE-1150687 (V.I., S.G., J.P.C.); the University of Washington and the U.S. National Science Foundation under Awards CHE-1253775 and PHY-130045 (N.W.B., D.J.M.); and the Eugene P. Wigner Fellowship program of Oak Ridge National Laboratory and the U.S. Department of Energy, Office of Basic Energy Sciences (BSG). V.I., N.M.K., and S.G. thank Gerd Duscher for facilitating the STEM/EELS experiments.

Chapter 7

Electron Tomography and its Importance to Quantitative Modeling of Experiment

N. W. Bigelow, T. L. Sooter, K. Munechika, D. S. Ginger, and D. J. Masiello.

This work is currently in progress.

7.1 Introduction

Computational electrodynamics is among the most powerful tools employed in the study of plasmonics [60, 67]. The application of theory to challenging problems in plasmonics has lead to considerable insight through its ability to quickly produce good approximations of physical properties that are presently difficult or impossible to directly measure on the length scales of

the plasmon [11]. However, despite the resounding success of computational electrodynamics in modeling plasmons, significant challenges to simulation remain. A major problem lies in accurately reproducing a real target *in silico*, as idealizations of the target as a simple solid may omit important structural details and typical electron micrographs of the target are only from a single vantage, effectively hiding one dimension of the target from the theorist. Attempting to reconstruct a target from a single electron micrograph taken from above can be likened to trying to deduce what a skyscraper looks like using only a photograph of its roof. Electron tomography, a method by which a target is reconstructed in 3-d from a series of electron micrographs taken at different angles, has the capability to significantly alleviate much of this problem, though the method is not without its own set of challenges. Accurate reproduction of the target requires the images from which the tomogram is built to show all relevant details from several angles, which is difficult near a substrate or in the junction between two particles. Once a tomogram has been obtained, the boundary between different media must be determined, any gaps in the boundary must be filled, and the resulting target must be discretized such that it can be used in an electrodynamics code.

In this work, we detail a new implementation of electron tomography which mitigates the difficulties inherent to the method by extrapolating over any gaps in the data before finding the boundaries between different media and finally producing a shape file that is usable with the DDSCAT [47] and our own *e*-DDA [60, 67]. We then use a reconstructed nanoparticle multimer generated by the electron tomography code to compare both the target itself and a number of computed properties of the target including far-field excitation and extinction, electron energy-loss spectroscopy, and electric hot spot volume to those of a target generated

in the usual manner using idealized solid approximated from a single electron micrograph of the same aggregate.

7.2 Methods

Tomography, from the Greek *τόμος* meaning "slice", is a method by which $n+1$ dimensional data can be built up from n dimensional data taken from various angles rotated about an axis of reconstruction [56]. To reconstruct a target with electron tomography, a series of electron micrographs are taken of the same structure from different viewing angles rotating about a single axis. A second series of images known as sinograms are built up in which one axis is a single row of electron tomography beam locations perpendicular to the axis of rotation and the other axis is the angle of rotation. Each row of electron tomography data can be thought of as a series of integrals of the electron loss intensity rastered over a plane perpendicular to the axis of rotation, effectively exchanging the beam location (x, y) for a set of rotated coordinates (a, b) *via*

$$(x, y) = (a\sin\alpha + b\cos\alpha, -a\cos\alpha + b\sin\alpha), \tag{7.1}$$

where α is the angle of rotation and the absorbance at any point can be written in terms of the new rotated variable set. By appropriately integrating over all angles, the sinogram can be converted into a "slice" of the target perpendicular to the axis of rotation and the stacked slices from the other rows and their corresponding sinograms form a three-dimensional re-

construction of the target.

In order to make a shape file usable by an electrodynamics code, the edges of the structure must be determined. This is a non-trivial problem, as unlike x-ray imaging, the absorbance of the electron beam passing through the target is not necessarily proportional to the thickness of the target [255] and some parts of the target may be occluded by others at some angles. To detect the edges, we employ a Canny edge detection algorithm [256] followed by interpolation over any occluded parts of a shape using a cubic spline. The Canny edge detection begins by despeckling the image with a slight Gaussian blur followed by the application of a gradient operator to the image. Once the gradient of the image has been found, any pixels are suppressed if they are not greater than their nearest neighbors. The remaining maxima are subsequently filtered by a hysteresis threshold; beginning at a point with a gradient above a high threshold, the edge is followed until the gradient maxima line magnitude falls below a low threshold. Hysteresis thresholding eliminates any maxima contours that do not have a high intensity at some point, but the code will still follow a faint section of an edge after a starting point is identified. The gradient points toward the direction of greater electron absorbance, which delineates the interior of the target from the exterior and allows the code to distinguish which points are inside the target from those that are not.

After edge detection, a cubic spline is used to interpolate over any gaps in the edge and any areas where one particle occludes another. First, a starting point is found by searching the outline for cusps, indicative of the point at which two particles overlap. Once a cusp is found, two cubic splines are fit, one to each side of the cusp, to fill in the missing sections of

the edge. Then any edge that does not form a closed loop is identified and the points nearest the gap(s) are use to interpolate across it, closing the loop. Once the edges are completed, the interior of the target as defined by the gradient is given a value of 1, while the exterior is given a value of 0 to generate a binary image. Sinograms can then be produced from the resulting binary images and the target is then reconstructed as described above. After target reconstruction, the number of shape points, or voxels, is reduced if necessary to produce a set of Cartesian points that can be passed into computational electrodynamics code as a target.

7.3 Results and discussion

7.3.1 Comparison of two targets generated by tomography and top-down idealization

7.1 overlays the target generated by assuming all particles are spheres on a common substrate with radii and locations based on a single electron micrograph taken from above, henceforth known as the "top-down spherical reconstruction", over the full tomographic reconstruction produced by the code described in this work. Immediately, several trends appear: first, the overall shape and arrangement of the two targets are similar, though, second, there are marked differences in the fine-scale structure and overall volume of the two targets. The top-down spherical reconstruction is a full 11% smaller than the tomographic reconstruction in volume. Scaling the surface area of the tomographic reconstruction by volume and then

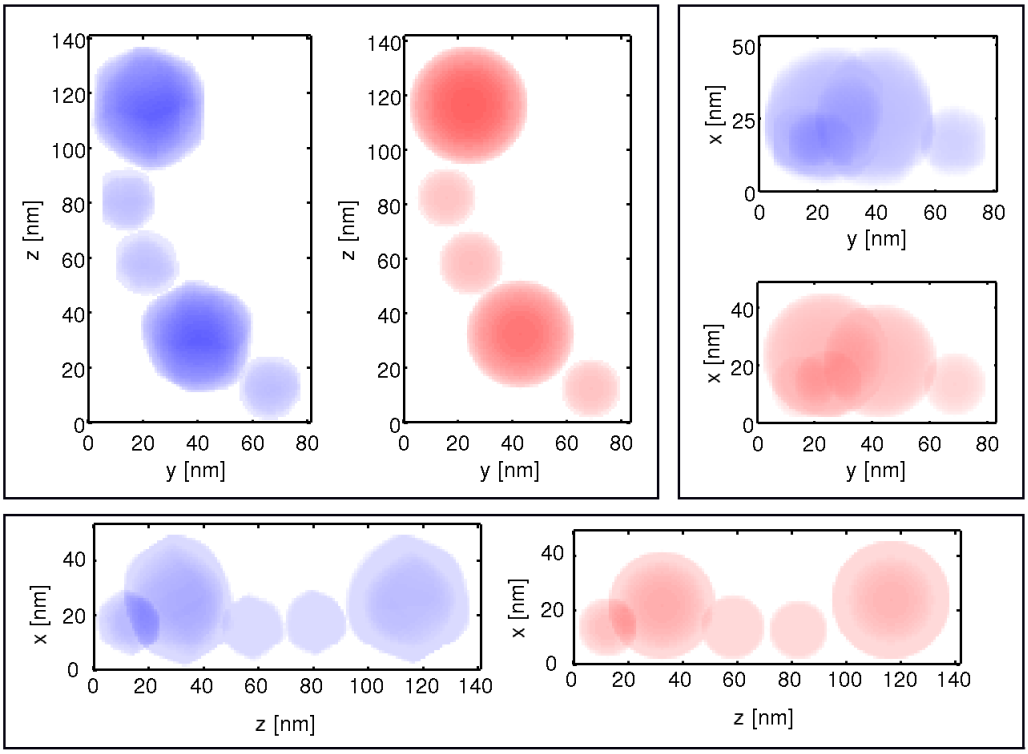

Figure 7.1: A comparison of the tomographic (blue) and top-down spherical (red) reconstructions of an aggregate of silver nanoparticles from above relative to the substrate (upper left) and from two orthogonal views from the side (upper right and lower panels). Color intensity correlates in direct proportion to target thickness in the direction perpendicular to each plot. The overall form of both targets are similar, but marked deviations from spherical are seen in the tomographic reconstruction in all three viewing angles. The top-down spherical reconstruction was made only using a single electron micrograph from the same angle as the upper left panel, and therefore shows considerable deviation from the tomographic reconstruction in the direction perpendicular to the substrate (x), as shown in the left and bottom panels.

dividing by the surface area of the guess reconstruction *via*

$$\phi = \frac{A_{tomo} V_{guess}}{A_{guess} V_{tomo}} = \frac{A_{tomo} \sum_{j=1}^{N} r_j^3}{3 V_{tomo} \sum_{k=1}^{N} r_k^2}, \tag{7.2}$$

yields ϕ, the ratio of the surface area of the target to the target composed of perfect spheres of the same volume, where the A's are the surface areas and the v's are the volumes and

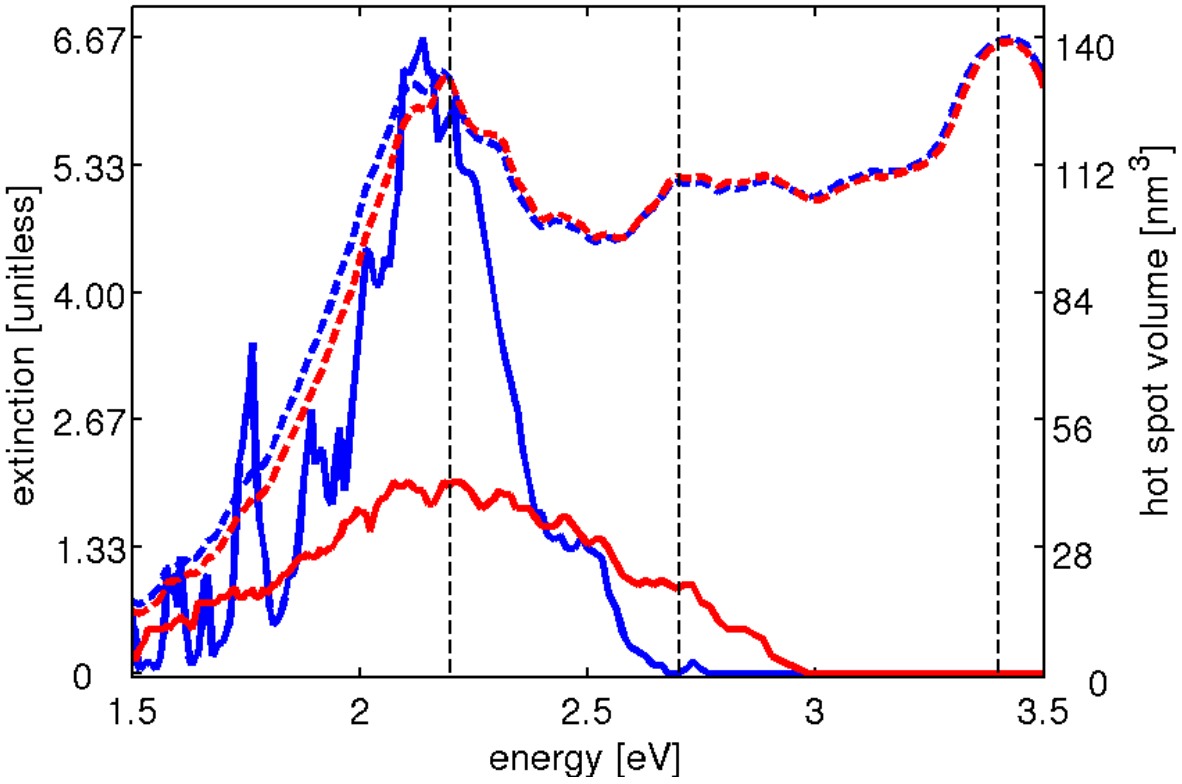

Figure 7.2: Comparison of the plane wave extinction (dashed lines) and electric hot spot volume (solid lines, $|\mathbf{E}_{sca}| \geq 100 \times |\mathbf{E}_{inc}|$) spectra from a spherical top-down reconstruction (red) and a tomographic reconstruction (blue) of the same nanosphere aggregate, as shown in 7.1. The extinction spectra show significant similarity in contrast to the considerable difference between the hot spot volume spectra. The dashed vertical black lines mark the energies where the scattered near-fields and LPMs are plotted in 7.4 and 7.3.

$r_{j,k}$ are the average distances from the centers of mass to the edges of each particle in the top-down electron micrograph of the target ($1 \leq j, k \leq N$). ϕ is a convenient way to quantitate tomographic reconstruction's deviation from spherical. For example, if the target were of cubes of equivalent volume, ϕ would be $\sqrt[3]{6\pi} \approx 1.24$. For the tomographic reconstruction in this work, ϕ is not yet prepared, though such a measure will undoubtedly be useful to a researcher seeking to quantitate the difference between two target reconstruction methods.

7.3.2 Comparison of the electromagnetic properties of the two targets

The far-field extinction spectra (dotted lines, 7.2) for the two reconstruction methods are very similar, particularly in the blue, with a maximum of 16% difference between the two spectra over the plotted range. A slight red shift and increase in intensity for the tomographic reconstruction is seen below 2 eV, as would be expected for the tomographic reconstruction's slightly larger volume. The solid lines in 7.2 are the volume of space surrounding the target where the magnitude of the scattered electric fields are one hundred times or more than the magnitude of the incident electric field ($|\mathbf{E}_{sca}| \geq 100 \times |\mathbf{E}_{inc}|$). In contrast to the far-field extinction spectra, the hot spot volume spectra are very different at energies of interest, with a maximum of 289% difference. The hot spot volume of the spherical reconstruction is larger above 2.4 eV, but the hot spot volume of the tomographic reconstruction is nearly three times larger around 2.2 eV, which is the location of the dipole mode as identified in the left panel 7.3, and demonstrates how sensitive the hot spot volume is to small changes in the target geometry. Surface roughness may induce the lightning rod effect [257, 258], where the electric field is enhanced at the point of a sharp feature. If that surface roughness brings the surface closer to another particle, then the effect will be magnified further by increased coupling. Thus, if there is considerable surface roughness in the tomographic reconstruction that is not captured by the idealized top-down reconstruction, it is reasonable to expect the maximum electric hot spot volume to be enhanced in the tomographic reconstruction and for the top-down reconstruction to underestimate the hot spot volume relative to experiment. While in this case the maximum hot spot volume is much larger for the

tomographic reconstruction, it is possible to imagine a deviation from the ideal that would instead reduce the hot spot volume, such as a flattening of the spheres near the junction, increasing the interparticle gap. It is left to the judgement of the computationalist whether a particular shape will lend itself to an increase or a decrease in hot spot volume over the ideal.

7.3 presents the electron energy loss probability maps (LPMs) for an area extending 4 nm outside the targets, which were generated by both reconstruction methods. Loss energies are at three peaks spanning the optical extinction spectrum at 3.4 eV, 2.7 eV, and 2.2 eV.

The LPM at 2.2 eV (right column) shows a collective dipolar loss pattern in the tomographic reconstruction, with high loss probability at the far ends of the structure and low loss probability inside, indicating a consistent polarization direction across all spheres, as is expected for the lowest energy eigenmode. Interestingly, the top-down reconstruction also has its lowest eigenmode at 2.2 eV, but this structure shows a significant dipolar loss pattern only across two of the five spheres with little participation by the others. The lowest energy eigenmode also corresponds to the largest hot spot volume for both reconstructions. In the bonding or collective dipolar mode the polarizations of all the spheres are largely colinear, and this head-to-tail arrangement of the polarizations leads to high electric field capacitive bonding in the junctions. That only two spheres participate strongly in this mode for the top-down reconstruction and all five spheres participate for the tomographic reconstruction is likely in part why the maximum hot spot volume is much smaller for the top-down reconstruction. Further, the high loss probability spans across the two large spheres in the tomographic reconstruction, with the small sphere on the end only providing a small exten-

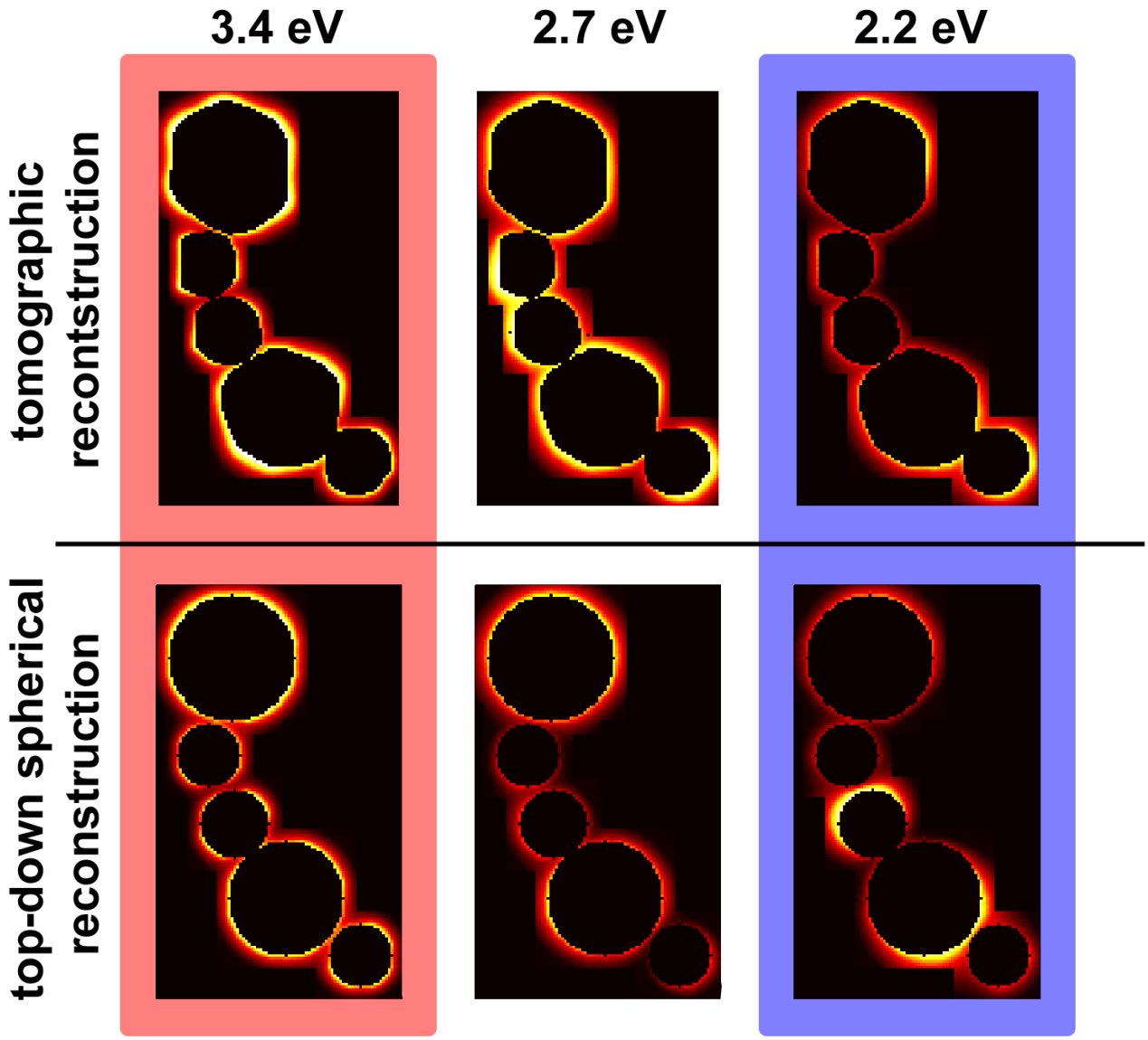

Figure 7.3: Electron energy loss maps for both tomographic (top) and top-down (bottom) reconstructions of a nanosphere aggregate, at 2.2 eV (right), 2.7 eV (middle), and 3.4 eV (left). At 3.4 eV the loss probability is dominated by a dipolar excitation of the large spheres transverse to the long axis of the aggregate, while at 2.2 eV the loss probability map shows the collective dipole (bonding) mode of the aggregate. 2.7 eV shows a collective quadrupolar mode, with the node in the polarization coming between the two central smaller spheres in the tomographic reconstruction, as evidenced by the high loss probability in that junction. This effect is less clear in the top-down spherical reconstruction due to the overlap of other modes.

sion of the main loss probability, illustrating the degree of control the larger spheres exercise over the eigenmodes of the aggregate. At the highest loss energy plotted, the loss probability is dominated by a dipolar excitation of the individual spheres transverse to the long axis of the aggregate, which can be compared to the transverse modes of the single rod [60]. The loss probability of the middle energy, 2.7 eV, shows what is likely a collective quadrupolar mode, with the node in the polarization coming between the two central smaller spheres in the tomographic reconstruction and between the lower large sphere and the inner small sphere in the top-down reconstruction, as evidenced by the high loss probability in that junction, though the latter is less obvious and likely overlaps with higher order modes to a greater extent.

Notably, while there are marked differences between the loss probability maps of each target, particularly near the surfaces of the targets, the overall structure of the far-field loss spectrum is the same, implying that similar eigenmodes are excited at each energy, but that their structure differs noticeably on the nanoscale. Examining the scattered electric fields around the targets at the same energy in 7.4 further supports this assertion.

7.4 shows the scattered electric field magnitude relative to the incident field magnitude ($|\mathbf{E}_{sca}|/|\mathbf{E}_{inc}|$) for both reconstructions at the same energies as the loss probability maps (2.2 eV, 2.7 eV, and 3.4 eV) excited by far-field light. The intensity of the color represents the magnitude of the scattered electric field, scaled to an appropriate maximum for each loss energy (20×, 10×, and 5×, respectively). The plots largely confirm the interpretation of the loss probability maps and hot spot volume spectra above. High scattered fields are

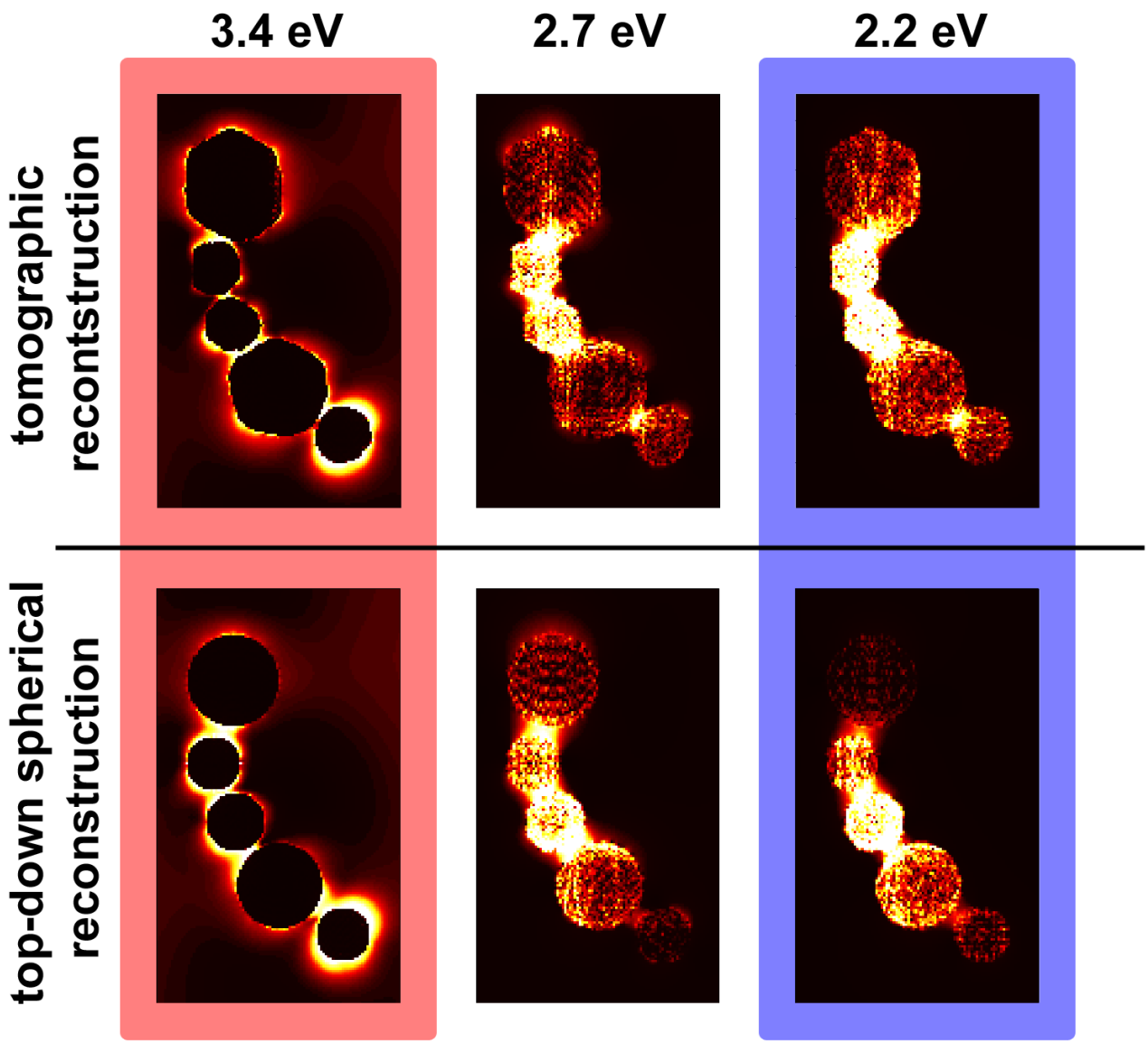

Figure 7.4: The scattered electric field magnitudes for both reconstructions of the nanoparticle aggregate relative to the incident field ($|\mathbf{E}_{sca}|/|\mathbf{E}_{inc}|$) as excited by a plane wave normal to the plane of the plot. Darker colors represent lower electric field magnitude, and brighter higher magnitude. Tomographic reconstructions are on the top row, and top-down spherical reconstructions are on the bottom. Excitation energies are 2.2 eV (right column), 2.7 eV (middle), and 3.4 eV (left). The color range for each energy is scaled independently. For 2.2 eV, the color maximum is 20 times the incident field, for 2.7 eV the maximum is 10 times, and for 3.4 eV the maximum is 5 times the incident field magnitude. The scattered fields at 3.4 eV show transverse single-sphere dipolar modes with some higher order structure visible in the large spheres. The two reconstructions' field magnitudes show the greatest degree of similarity at 2.7 eV, though the location of the maximum field differs. At 2.2 eV, the tomographic reconstruction shows very high field magnitude in the junctions between the two large spheres, but the top-down spherical reconstruction shows very high field magnitude only in a single junction between one of the large spheres and a small sphere.

seen transverse to the long axis of the aggregate at 3.4 eV, as expected. Some higher nodal structure is visible on the larger spheres at this energy due to overlap with higher order (quadrupole, hexapole, etc.) modes at this energy. At 2.7 eV, we now see hot spot volume heavily localized to the junctions between the spheres, indicating the presence of longitudinal modes at this energy. The scattered fields at 2.7 eV show the greatest degree of similarity between the two reconstructions of the three plotted energies, with only slight differences in the relative magnitudes observed. By 2.2 eV the collective dipolar mode is active, as shown in the left panel of 7.4 and of 7.3. The tomographic reconstruction shows the highest fields in the three junctions between the two large spheres, which corresponds well with the high loss probability at the ends of the same spheres. The top-down spherical reconstruction shows the highest loss probability between the lower large sphere and its neighboring internal small sphere, with the scattered fields in the other junctions being noticeably smaller. This again correlates well with the loss probability being highest at the ends of the spheres between which the scattered field assumes the greatest magnitude. Even when excited by a far-field probe such as plane wave light, the near-field effects differ between the two reconstructions.

7.4 Conclusion

Electron tomography offers an attractive method to bring computational electrodynamics on real targets into the realm of quantitation. This work has shown that near-field effects, either through the near-field probe of the electron beam or scattered near-fields after interaction with a far-field source such as plane wave light, are highly sensitive to small deviations from ideal in the target. Purely far-field effects are less sensitive to such changes and idealized

reconstructions of real targets still work well in modeling these effects. Tomography may also be applied directly to EELS. Recently, energy filtering has been applied to the electron micrograph slices to generate three dimensional reconstructions of the loss probability per unit length for metal cubes [253], showing the utility of tomography applied to experimental EEL data as well. While considerable work remains to be done as the application of tomography to the numerical study of nanoparticles remains in its infancy, there is no doubt that tomographic methods will revolutionize the field of computational electrodynamics.

Chapter 8

Conclusion

The aim of this work has been to expand the understanding of plasmonics, particularly as it applies to interference phenomena and and EELS. To accomplish this, the thesis is divided into four sections, each expanding the body of knowledge of plasmonics. First, using EELS to detect electric hot spots living near plasmons is shown to be possible. Prior work had intimated that EELS is "completely blind to the hot spot" [62], but this work shows it is possible to indirectly infer the existence of a hot spot anyway. This prediction is then experimentally confirmed, dramatically expanding EELS' capabilities as an investigative tool for plasmonics.

Second, this work explores magnetic hot spots generated through the collusion of multiple plasmons to create oscillating ring currents. The rich collection of multiple magnetic plasmons of alternating magnetic and ferromagnetic order living on a single nanoparticle aggregate is shown for the first time. This work significantly expands the field of magnetoplasmonics and opens it to the construction of much more complex magnetically-active structures.

Third, the interference phenomena known as the Fano resonance is shown to be accessible by EELS for the first time in this work. Fano resonances have been described as the best sensors of the dielectric environment yet known, which when combined with the spatial resolution of EELS opens up a dramatic new way to measure local dielectric functions with unprecedented spatial and energetic resolution. In searching for Fano resonances in EELS, an entirely new class of Fano resonance in which an optically dark mode is preferentially driven is found living only in EELS. Experimental confirmation of the Fano resonance in EELS is then shown, having been found in the year following their prediction.

Last, the use of electron tomography to produce three-dimensional models of nanometer-scale plasmon-supporting targets is explored. It is found that for some properties, such as the far-field scattering spectrum, the traditional guess and tomographic reconstruction methods are in good agreement for the studied aggregates, though for other properties such as the hot spot volume the two reconstruction methods lead to markedly different results. This work urges care on the part of the theoretician in interpreting numerical results modeling real plasmonic systems, and helps bring previously qualitative results into the quatitative.

Chapter 9

Appendix

9.1 Appendix A

evale.f90 for the *e*-DDA

This subroutine calculates the incident electric field from an electron moving in a constant motion parallel to the x-axis in frequency space, which forms the right hand side of the coupled dipole approximation linear equation

$$\sum_{j=1}^{N}[\boldsymbol{\alpha}_{ii}^{-1}(\omega)\delta_{ij} - (1-\delta_{ij})\boldsymbol{\Lambda}_{\mathbf{ij}}] \cdot \mathbf{P}_j(\omega) = \mathbf{E}_{\text{electron}}(\mathbf{x}_i, \omega), \tag{9.1}$$

as found in the *e*-DDA [60]. This code is designed to work with the addition of the Bessel function subroutines outlined in Numerical Recipes [52]: besseli0, besseli1, besselk0, and besselk1, corresponding to their respective Bessel functions. This code is designed to be dropped in to DDSCAT 7.1 [47] with minimal modification to the other subroutines. Inputs

and outputs must be modified in getfml.f90 and ddscat.f90 to reflect those found in the header of this code. Slight modifications to this code may be necessary to insert it into later versions of DDSCAT.

New variables added to the input/output deck are:

AEFFA: effective radius of the target, an internal variable already in DDSCAT 7.1.

WAVEA: equivalent wavelength of the $\mathbf{E}_{inc}$, an internal variable already in DDSCAT 7.1.

MXRAD: number of effective radii, an internal variable already in DDSCAT 7.1.

MXWAV: number of equivalent wavelengths, an internal variable already in DDSCAT 7.1.

Center: the impact parameter of the electron beam, in dipole spacings.

c: the speed of light, in cm/s.

velocity: the speed of the electron, in cm/s.

e_charge: the charge of the electron in Coulombs.

DielectricConst: the background dielectric constant.

```
!*********************Nicholas Bigelow and Alex Vaschillo 2012*******************
!Incorporated code that models a fast electron's interaction with a group of dipoles
!as in "Optical Excitations in electron microscopy", Rev. Mod. Phys. v. 82 p. 213
!equations (4) and (5)

    SUBROUTINE EVALE(CXE00,AKD,DX,X0,IXYZ0,MXNAT,MXN3,NAT,NAT0,NX,NY,NZ,CXE,AEFFA, &
                     WAVEA,MXRAD,MXWAV,Center,c,velocity,e_charge,DielectricConst)
      !Arguments AEFFA and after added by NWB 3/8/12
      USE DDPRECISION,ONLY : WP
      IMPLICIT NONE

!*** Arguments:
      INTEGER :: MXN3, MXNAT, NAT, NAT0, NX, NY, NZ, MXRAD, MXWAV
      !MXRAD, MXWAV added by NWB 3/8/12
      INTEGER :: IXYZ0(NAT0,3)
```

```
      REAL(WP) :: AKD(3), DX(3), X0(3), AEFFA(MXRAD), WAVEA(MXWAV), Center(3)
         !AEFFA and after added by NWB 3/8/12

! Note: CXE should be dimensioned to CXE(NAT,3) in this routine
!       so that first 3*NAT elements of CXE are employed.
!       XYZ0 should be dimensioned to
      COMPLEX(WP) :: CXE(NAT,3), CXE00(3)

!***  Local variables:
      COMPLEX(WP) :: CXFAC, CXI
      REAL(WP) :: X, X1, X2, CenterX0(3)
      INTEGER :: IA, IX, IY, IZ, M, JJ

!*** Variables added by Nicholas Bigelow and Alex Vaschillo:
      REAL(WP) :: c, e_charge, EFieldConstant, omega, gamma, k_mag, DS, PI, &
                  BesselArg, DielectricConst, velocity
      REAL, DIMENSION(:), ALLOCATABLE :: R
      REAL(WP) :: Radius !This serves the exact same purpose as the array R() but
      !is used in a different scope (only in the else statement, see below)
      REAL(WP) :: besselk0, besselk1 !Values of Bessel functions K0 and K1
      REAL(WP) :: besseli1, besseli0 !Values of Bessel functions I0 and I0,
      !necessary for K0 and K1 routines
      INTEGER :: i !For indexing do loops

!*** Intrinsic functions and constants:
      INTRINSIC EXP, REAL
      INTRINSIC ATAN2, DCOS, DSIN, AIMAG
      PI = 4._WP*ATAN(1._WP)          !pi

!*** Define center in internal coordinates
      CenterX0(1) = Center(1) - X0(1) !Center of e-beam in relative coordinates
      CenterX0(2) = Center(2) - X0(2)
      CenterX0(3) = Center(3) - X0(3)

!**********************************************************************
! subroutine EVALE
! Given:   CXE00(1-3)=Incident E field at origin (complex) at t=0
!          AKD(1-3)=(kx,ky,kz)*d for incident wave (d=effective
!                    lattice spacing)
!          DX(1-3)=(dx/d,dy/d,dz/d) for lattice (dx,dy,dz=lattice
!                   spacings in x,y,z directions, d=(dx*dy*dz)**(1/3)
!          X0(1-3)=(x,y,z)location/(d*DX(1-3)) in TF of lattice site
!                  with IX=0,IY=0,IZ=0
!          IXYZ0(1-NAT0,3)=[x-x0(1)]/dx, [y-x0(2)]/dy, [z-x0(3)]/dz
!                  for each of NAT0 physical dipoles
```

```
!          MXNAT,MXN3=dimensioning information
!          NAT0=number of dipoles in physical target
!          NAT=number of locations at which to calculate CXE
! Returns: CXE(1-NAT,3)=incident E field at NAT locations at t=0
! Copyright (C) 1993,1997,2007,2012 N.W. Bigelow, A. Vaschillo,
! B.T. Draine, and P.J. Flatau
! This code is covered by the GNU General Public License.
!***********************************************************************

      CXI=(0._WP,1._WP)

!Evaluate electric field vector at each dipole location.
!If NAT=NAT0, then evaluate E only at occupied sites.
!If NAT>NAT0, then evaluate E at all sites.

!*** Allocate memory to arrays
      ALLOCATE( R(NAT) )

!*** Compute dipole spacing in meters
      DS = 1E-6_WP * AEFFA(1) * (4._WP * PI / (3._WP * NAT0) )**(1._WP/3._WP)

!*** Compute omega
      omega = 2._WP * PI * c / (WAVEA(1) * 1E-6_WP) !Conversion from microns to meters

!*** Calculate EFieldConstant - the constant that g(r) is multiplied by
      gamma = (1._WP - DielectricConst * (velocity / c) ** 2._WP) ** (-0.5_WP)
      EFieldConstant = 2._WP * e_charge * omega / (velocity ** 2._WP * gamma &
                       * DielectricConst)

      PRINT *, 'Relative coordinates of beam:', Center
      PRINT *, 'Electron speed:', velocity

      IF (NAT == NAT0) THEN
         !*** Calculate radius and prevent divide by zero errors
         DO i = 1, NAT0
            R(i) = (IXYZ0(i, 3) - CenterX0(3)) ** 2._WP + &
                   (IXYZ0(i, 2) - CenterX0(2)) ** 2._WP
            R(i) = SQRT(R(i)) * DS
            IF (R(i) .EQ. 0._WP) THEN
               !If the radius is zero, set to a small, but finite distance
               R(i) = 0.01_WP * DS
               PRINT *, 'WARNING: RADIUS = 0! Re-set to 0.01*DS!'
               PRINT *, 'IX, IY, IZ:', IX, IY, IZ
            END IF
         END DO
```

```
   !*** Calculate g(r)
   DO i = 1, NAT0
      BesselArg = omega * R(i) / (velocity * gamma)
      !The argument of the Bessel functions
      CXE(i, 3) = EXP(CXI * omega * DS * (IXYZ0(i, 1) - CenterX0(1)) / velocity)
      !This is the prefactor that each component of CXE is multiplied by

      !*** Calculate electric field components at point i
      CXE(i, 1) = EFieldConstant * CXE(i, 3) * (CXI * besselk0(BesselArg) &
                  / gamma)
      CXE(i, 2) = EFieldConstant * CXE(i, 3) * (-1._WP * besselk1(BesselArg)) * &
                  DSIN(ATAN2((DBLE(IXYZ0(i, 2)) - CenterX0(2)) , &
                  (DBLE(IXYZ0(i, 3)) - CenterX0(3))))
      CXE(i, 3) = EFieldConstant * CXE(i, 3) * (-1._WP * besselk1(BesselArg)) * &
                  DCOS(ATAN2((DBLE(IXYZ0(i, 2)) - CenterX0(2)) , &
                  (DBLE(IXYZ0(i, 3)) - CenterX0(3))))
   END DO
ELSE
   IA=0 !Index that labels each unique point at which the field is calculated
   DO IZ=1,NZ
      DO IY=1,NY
         DO IX=1,NX

            IA = IA + 1 !Advance IA

            !*** Calculate Radius and prevent divide by zero errors
            Radius = (IZ - CenterX0(3)) ** 2._WP + &
                     (IY - CenterX0(2)) ** 2._WP
            Radius = SQRT(Radius) * DS
            IF (Radius .EQ. 0._WP) THEN
            !If the radius is zero, set to a small, but finite distance
               Radius = 0.01_WP * DS
               PRINT *, 'WARNING: RADIUS = 0! Re-set to 0.01*DS!'
               PRINT *, 'IX, IY, IZ:', IX, IY, IZ
            END IF

            !*** Calculate g(r)
            BesselArg = omega * Radius / (velocity * gamma)
            !The argument of the Bessel functions
            CXE(IA, 3) = EXP(CXI * omega * DS * &
                                  (DBLE(IX) - CenterX0(1)) / velocity)
            !This is the prefactor that each component of CXE is multiplied by

            !*** Calculate electric field components at point IA
```

```
                  CXE(IA, 1) = EFieldConstant * CXE(IA, 3) * &
                                    (CXI * besselk0(BesselArg) / gamma)
                  CXE(IA, 2) = EFieldConstant * CXE(IA, 3) * &
                                    (-1._WP * besselk1(BesselArg)) * &
                                    DSIN(ATAN2((DBLE(IY) - CenterX0(2)) , &
                                   (DBLE(IZ) - CenterX0(3))))
                  CXE(IA, 3) = EFieldConstant * CXE(IA, 3) * &
                                     (-1._WP * besselk1(BesselArg)) * &
                                     DCOS(ATAN2((DBLE(IY) - CenterX0(2)) , &
                                     (DBLE(IZ) - CenterX0(3))))
               END DO
            END DO
         END DO

         PRINT *, "IA is: ", IA
      ENDIF

      DEALLOCATE( R )
      RETURN
END SUBROUTINE EVALE
```

9.2 Appendix B

evalq.f90 for the e-DDA

This subroutine calculates the probability for an electron to lose $\hbar\omega$ of energy to the target, given a set of target polarizations $\mathbf{P}_j(\omega)$ previously calculated by other parts of the e-DDA code [60], via

$$P_{\mathbf{b}}(\hbar\omega) = \frac{1}{\pi\hbar^2}\mathrm{Im}\sum_{j,k=1}^{N}\mathbf{E}^*_{\mathrm{EELS}}(\mathbf{x}_j,\omega)\cdot\mathbf{P}_j, \tag{9.2}$$

in which $\mathbf{E}_{\mathrm{EELS}}(\mathbf{x}_j,\omega)$ is the Fourier component at ω of the incident electric field of the electron at $\mathbf{x}_j$ [11]. This code is designed to be dropped in to DDSCAT 7.1 [47] with minimal modification to the other subroutines. Inputs and outputs must be modified in getfml.f90 and ddscat.f90 to reflect those found in the header of this code. Slight modifications to this code may be necessary to insert it into later versions of DDSCAT.

New variables added to the input/output deck are:

h_bar: Planck's constant, in J-s

h_bar2: Planck's constant, in eV-s

MXRAD: the number of effective radii, an internal variable already in DDSCAT 7.1.

AEFFA: the effective radius of the target, an internal variable already in DDSCAT 7.1.

NAT0: the number of dipoles in the target, an internal variable already in DDSCAT 7.1.

```
!**********************Alex Vaschillo and Nicholas Bigelow 2012*********************
!Modified to output the parameter Gamma as described in:
!"Optical Excitations in electron microscopy", Rev. Mod. Phys. v. 82
!p. 234 equation (46), using the original code for extinction.
!Normalized to units of %/per eV
    SUBROUTINE EVALQ(NAT3,CXE,CXP,CABS,CEXT,CPHA,IMETHD,MXN3, &
                     h_bar,h_bar2,MXRAD,AEFFA,NAT0)
      !All arguments h_bar and after added, some arguments removed by NWB 7/11/12
      USE DDPRECISION,ONLY: WP
      IMPLICIT NONE

!*** Arguments:
      INTEGER :: IMETHD, MXN3, NAT3, NAT0, MXRAD
      REAL(WP) :: CABS, CEXT, CPHA, h_bar, h_bar2, AEFFA(MXRAD), AK(3)
      COMPLEX(WP) :: CXE(MXN3), CXP(MXN3)

!*** Local variables:
      COMPLEX(WP) :: CXA, CXI, DCXA, RABS
      REAL(WP) :: PI, DS
      INTEGER :: J1, J2, J3, NAT

!*** Intrinsic functions:
      INTRINSIC AIMAG, CONJG, REAL, SQRT

!*** SAVE statements:
      SAVE CXI

!*** Data statements:
      DATA CXI/(0._WP,1._WP)/

!***********************************************************************
! Given: NAT3 = 3*number of dipoles
!        CXE(1-NAT3) = components of E field at each dipole, in order
!                      E_1x,E_2x,...,E_NATx,E_1y,E_2y,...,E_NATy,
!                      E_1z,E_2z,...,E_NATz
!        CXP(1-NAT3) = components of polarization vector at each dipole,
!                      in order
!                      P_1x,P_2x,...,P_NATx,P_1y,P_2y,...,P_NATy,
!                      P_1z,P_2z,...,P_NATz
!        IMETHD = 0 or 1
! Finds:
!        CEXT = loss probability, Gamma, in units of eV^-1
!  and, if IMETHD=1, also computes
!        CPHA = 0
!        CABS = 0
```

```
! Inputs and outputs updated by NWB, 7/11/12
! B.T.Draine, Princeton Univ. Obs., 87/1/4
! Copyright (C) 1993,1997,1998,2008,2012 N.W. Bigelow, A. Vaschillo,
! B.T. Draine, and P.J. Flatau
! This code is covered by the GNU General Public License.
!***********************************************************************

      !Zero out variables and define internal constants
      CEXT = 0._WP
      CABS = 0._WP
      CPHA = 0._WP
      PI = 4._WP * ATAN(1._WP) !pi

!*** Compute dipole spacing in meters
      DS = 1E-6_WP * AEFFA(1) * (4._WP * PI / (3._WP * NAT0) )**(1._WP/3._WP)

      IF ( IMETHD==0 ) THEN

         !*** Compute CEXT:
         DO J1=1,NAT3
            CEXT = CEXT + AIMAG(CXP(J1)) * REAL(CXE(J1)) - &
            REAL(CXP(J1)) * AIMAG(CXE(J1)) !ORIGINAL CODE, Eapp* dot P
         ENDDO

         !Compute Gamma using CEXT NWB 7/11/12
         CEXT = CEXT * ((PI * h_bar * h_bar2) ** (-1._WP)) * 1.E-18_WP
         !(10^6)^3 correction factor for um/m

         !Renormalize for dipole spacing
         CEXT = CEXT * (DS * 1.E9_WP)**3._WP

      ELSEIF (IMETHD == 1) THEN

         !*** Compute CEXT:
         DO J1=1,NAT3                              !E dot P
            CXA = CXA + CXP(J1) * CONJG(CXE(J1))
         ENDDO

         !Compute Gamma using CEXT NWB 7/11/12
         CEXT = AIMAG(CXA) * ((PI * h_bar * h_bar2) ** (-1._WP)) * 1.E-18_WP
         !(10^6)^3 correction factor for um/m

         !Renormalize for dipole spacing
         CEXT = CEXT * (DS * 1.E9_WP)**3._WP
```

```
      ENDIF
  RETURN
END SUBROUTINE EVALQ
```

9.3 Appendix C

Additional code for ddscat.f90 and reapar.f90

This section of code can be added to ddscat.f90 immediately following the function call to REAPAR, which reads the parameter file and passes that data to DDSCAT. The first section of code defines the physical variables which the e-DDA uses that are not present in the base code. The second section converts the electron's relativistic kinetic energy into a velocity, using

$$v = c\sqrt{1 - \left(\frac{E_{kin}}{m_e c^2} + 1\right)^{-2}}, \tag{9.3}$$

where c is the speed of light, m_e is the mass of the electron, and E_{kin} is the kinetic energy of the electron [259]. In all the following code new variables need to be defined in the headers of their subroutines.

New variables added to the input/output deck are:

c: the speed of light, in m/s.

e_charge: the charge of electron, in Coulombs.

m_e: the mass of electron, in kg.

DielectricConst: the background dielectric constant.

h_bar: Planck's constant, in j-s.

h_bar2: Planck's constant, in eV-s.

ELENERGY: the kinetic energy of the electron, in keV.

velocity: the speed of the electron, in m/s.

```
!*********************************************************************
! Define variables for eDDA NWB 7/11/12
      c = 3.E8_WP                     !Speed of light, m/s
      e_charge = 1.60217646E-19_WP    !Charge of electron, Coulombs
      m_e = 9.10938188E-31_WP         !Mass of electron, kg
      DielectricConst = 1._WP         !Dielectric constant -- 1 for vacuum
      h_bar = 1.054572E-34_WP         !h_bar, j-s
      h_bar2 = 6.582119E-19_WP        !h_bar, eV-s
!*********************************************************************

!*********************************************************************
! Convert electron energy from keV to electron velocity in m/s
! NWB 7/12/12
         ELENERGY = ELENERGY*1.60217646E-16_WP !Convert to Joules
         velocity = c * (1._WP - ((ELENERGY / (m_e * c**2._WP)) + 1 ) &
                    **(-2._WP))**0.5_WP
!*********************************************************************
```

The following two sections of code should be added to reapar.f90 in order to read in the electron beam's centroid in units of dipole spacings relative to the target frame and the

kinetic energy of the electron beam in keV. This code should be added immediately after the code reading MXNX, MXNY, and MXNZ from the parameter file.

New variables added to the input/output deck are:

CENTER: Centroid of the electron beam, in dipole spacings

ELENERGY: Kinetic energy of the electron, in keV

```
!=====================================================================
! e-BEAM CENTROID READER
! Added by NWB 3/13/12
      READ(IOPAR,FMT=*,ERR=99)CENTER
!=====================================================================
! ELECTRON RELATIVISTIC ENERGY READER
! Added by NWB 7/12/12
      READ(IOPAR,FMT=*,ERR=99)ELENERGY
!=====================================================================
```

Bibliography

[1] I. C. F. D. J. BARBER. "AN INVESTIGATION OF THE ORIGIN OF THE COLOUR OF THE LYCURGUS CUP BY ANALYTICAL TRANSMISSION ELECTRON MICROSCOPY". In: *Archaeometry* 32.1 (1990), 3345. DOI: 10.1111/j.1475-4754.1990.tb01079.x. URL: http://onlinelibrary.wiley.com/doi/10.1111/j.1475-4754.1990.tb01079.x/abstract.

[2] M. Faraday. "Experimental Relations of Gold (and Other Metals) to Light". In: *Philosophical Transactions of the Royal Society* 147 (1857), p. 145.

[3] R. H. Ritchie. "Plasma losses by fast electrons in thin films". In: *Physical Review* 106 (1957), pp. 874–881.

[4] W. A. Murray and W. L. Barnes. "Plasmonic Materials". In: *Advanced Materials* 19 (2007), pp. 3221–3782.

[5] V. Giannini and et. al. "Plasmonic Nanoantennas: Fundamentals and Their Use in Controlling the Radiative Properties of Nanoemitters". In: *Chem. Rev.* 111 (2011), pp. 3888–3912.

[6] R. H. Doremus. "Optical Properties of Small Gold Particles". In: *J. Chem. Phys.* 40.8 (1964).

[7] G. Mie. “Beiträge zur Optik trüber Medien, speziell kolloidaler Metallösungen”. In: *Ann. Phys.* 330 (1908), p. 377.

[8] F. Fujimoto and K. ichiro Komaki. “Plasma Oscillations Excited by a Fast Electron in a Metallic Particle”. In: *J. Phys. Soc. Jpn* 25.6 (1968).

[9] A. Kawabata and R. Kubo. “Electronic Properties of Fine Metallic Particles. II. Plasma Resonance Absorption”. In: *J. Phys. Soc. Jpn* 21.9 (1966).

[10] F. Fujimoto, K. ichiro Komaki, and K. Ishida. “Surface Plasma Oscillation in Aluminum Fine Particles”. In: *J. Phys. Soc. Jpn* 23 (1967), p. 1186.

[11] F. J. García de Abajo. “Optical excitations in electron microscopy”. In: *Rev. Mod. Phys.* 82 (2010), p. 209.

[12] S. Pillai et al. “Surface plasmon enhanced silicon solar cells”. In: *J. Appl. Phys.* 101 (2007), p. 093105.

[13] K. R. Catchpole and A. Polman. “Design principles for particle plasmon enhanced solar cells”. In: *Applied Physics Letters* 93.19, 191113 (2008), p. 191113.

[14] A. J. Morfa et al. “Plasmon-enhanced solar energy conversion in organic bulk heterojunction photovoltaics”. In: *Appl. Phys. Lett.* 92.1 (2008), p. 013504.

[15] S.-S. Kim et al. “Plasmon enhanced performance of organic solar cells using electrodeposited Ag nanoparticles”. In: *Appl. Phys. Lett.* 93 (2008), p. 073307.

[16] G. Haran. “Single-molecule Raman spectroscopy: A probe of surface dynamics and plasmonic fields”. In: *Acc. Chem. Res.* 43.8 (2010), pp. 1135–1143.

[17] H. A. Atwater and A. Polman. "Plasmonics for improved photovoltaic devices". In: *Nat. Mater.* 9.3 (2010), pp. 205–213.

[18] K. Kneipp et al. "Single Molecule Detection Using Surface-Enhanced Raman Scattering (SERS)". In: *Phys. Rev. Lett.* 78 (1997), p. 1667.

[19] S. Nie and S. R. Emory. "Probing Single Molecules and Single Nanoparticles by Surface-Enhanced Raman Scattering". In: *Science* 275 (1997), p. 1102.

[20] A. M. Michaels, J. Jiang, and L. Brus. "Ag Nanocrystal Junctions as the Site for Surface-Enhanced Raman Scattering of Single Rhodamine 6G Molecules". In: *Journal of Physical Chemistry B* 104 (2000), 1196511971.

[21] J. P. Camden et al. "Probing the Structure of Single-Molecule Surface-Enhanced Raman Scattering Hot Spots". In: *J. Am. Chem. Soc. Commun.* 130 (2008), p. 12616.

[22] J. L. Ponsetto, F. Wei, and Z. Liu. "Localized plasmon assisted structured illumination microscopy for wide-field high-speed dispersion-independent super resolution imaging". In: *Nanoscale* 6 (11 2014), pp. 5807–5812.

[23] K. A. Willets. "Super-resolution imaging of interactions between molecules and plasmonic nanostructures". In: *Phys. Chem. Chem. Phys.* 15 (15 2013), pp. 5345–5354.

[24] F. Wei et al. "Wide Field Super-Resolution Surface Imaging through Plasmonic Structured Illumination Microscopy". In: *Nano Letters* 14.8 (2014). PMID: 25014211, pp. 4634–4639. DOI: 10.1021/nl501695c.

[25] E. Y. Lukianova-Hleb et al. "On-demand intracellular amplification of chemoradiation with cancer-specific plasmonic nanobubbles". In: *Nature Medicine* 20 (2014), pp. 778–784.

[26] K. JC et al. "Early diagnosis of oral cancer based on the surface plasmon resonance of gold nanoparticles". In: *Int. J. Nanomedicine* 2.4 (2007).

[27] G. A. Sotiriou et al. "Photothermal Killing of Cancer Cells by the Controlled Plasmonic Coupling of Silica-Coated Au/Fe2O3 Nanoaggregates". In: *Advanced Functional Materials* 24.19 (2014), pp. 2818–2827. ISSN: 1616-3028. DOI: 10.1002/adfm.201303416. URL: http://dx.doi.org/10.1002/adfm.201303416.

[28] F. Hao et al. "Symmetry Breaking in Plasmonic Nanocavities: Subradiant LSPR Sensing and a Tunable Fano Resonance". In: *Nano Letters* 8.11 (2008), pp. 3983–3988.

[29] N. Liu et al. "Planar Metamaterial Analogue of Electromagnetically Induced Transparency for Plasmonic Sensing". In: *Nano Letters* 10.4 (2010), pp. 1103–1107.

[30] J. B. Lassiter et al. "Fano Resonances in Plasmonic Nanoclusters: Geometrical and Chemical Tunability". In: *Nano Letters* 10.8 (2010), pp. 3184–3189.

[31] J. P. Litz, J. P. Camden, and D. J. Masiello. "Spatial, Spectral, and Coherence Mapping of Single Molecule SERS Active Hot Spots via the Discrete-Dipole Approximation". In: *J. Phys. Chem. Lett.* 2 (2011), pp. 1695–1700.

[32] E. Betzig, L. P. Finn, and J. S. Wiener. "Combined shear force and near-field scanning optical microscopy". In: *App. Phys. Lett.* 60.20 (1992).

[33] R. H. Ritchie. "Plasma Losses by Fast Electrons in Thin Films". In: *Phys. Rev. B* 106 (1957), pp. 874–881.

[34] H Watanabe. "Experimental evidence for the collective nature of the characteristic energy loss of electrons in solidsStudies on the dispersion relation of plasma frequency". In: *J. Phys. Soc. Jpn.* 11 (1956), 112119.

[35] C. J. Powell and J. B. Swan. "Origin of the characteristic electron energy losses in aluminum". In: *Phys. Rev.* 115 (1959), 869875.

[36] L. de Broglie. "Waves and quanta". In: *Nature* 112 (1923), p. 540.

[37] B. Schaffer et al. "High-resolution surface plasmon imaging of gold nanoparticles by energy-filtered transmission electron microscopy". In: *Phys. Rev. B* 79 (4 2009), p. 041401.

[38] J. D. Jackson. *Classical Electrodynamics*. 3rd. New York: J. Wiley & Sons, 1999.

[39] K. Yee. "Numerical solution of initial boundary value problems involving maxwell's equations in isotropic media". In: *IEEE T. Antenn. Propag.* 14 (1966), p. 302.

[40] K. Bowman and L. Shenton. *Encyclopedia of Statistical Sciences*. Vol. 5. Canada: John Wiley & Sons, 1985. Chap. Method of moments, pp. 467–453.

[41] A. Taflove and S. C. Hagness. *Computational Electrodynamics: The Finite-difference Time-domain Method*. Norwood, MA: Artech House, 2000.

[42] H. DeVoe. "Optical properties of molecular aggregates. I. Classical mode of electronic absorption and refraction". In: *J. Chem. Phys.* 41 (1964), pp. 292–400.

[43] E. M. Purcell and C. R. Pennypacker. "Scattering and absorption of light by non-spherical dielectric grains". In: *Astrophys. J.* 186 (1973), p. 705.

[44] S. B. Singham and C. F. Bohren. "Light scattering by an arbitrary particle: the scattering-order formulation of the coupled-dipole method". In: *J. Opt. Soc. Am. A* 5.11 (1988), pp. 1867–1872.

[45] S. D. Druger et al. "Light scattering by inhomogeneous particles". In: *Appl. Opt.* 18.23 (1979), pp. 3888–3889.

[46] S. B. Singham. "Intrinsic optical activity in light scattering from an arbitrary particle". In: *Chemical Physics Letters* 130.12 (1986), pp. 139 –144. ISSN: 0009-2614. DOI: http://dx.doi.org/10.1016/0009-2614(86)80441-9. URL: http://www.sciencedirect.com/science/article/pii/0009261486804419.

[47] B. T. Draine and P. J. Flatau. "Discrete-dipole approximation for scattering calculations". In: *J. Opt. Soc. Am. A* 11 (1994), p. 1491.

[48] N. Geuquet and L. Henrard. "EELS and optical response of a noble metal nanoparticle in the frame of a discrete dipole approximation". In: *Ultramicroscopy* 110 (2010), pp. 1075–1080.

[49] J. P. Camden. Personal communication with Prof. Jon P. Camden University of Tennessee at Knoxville, 2012.

[50] B. T. Draine and P. J. Flatau. *User Guide to the Discrete Dipole Approximation Code DDSCAT 7.1*. http://arXiv.org/abs/1002.1505v1. Accessed: 2014-11-06. 2010.

[51] S. O. Guillaume, N. Geuquet, and L. Henrard. “Numerical study of optical and EELS response of coupled metallic nanoparticles”. In: *Proc. SPIE* 8089 (2011), p. 7.

[52] W. H. Press et al. *Numerical Recipes*. Cambridge: Cambridge University Press, 1986.

[53] R. A. Ferrell. “Predicted Radiation of Plasma Oscillations in Metal Films”. In: *Physical Review* 111.5 (1958).

[54] W. Stienmann. “Experimental Verification of Radiation of Plasma Oscillations in Thin Films”. In: *Physical Review Letters* 5.10 (1960).

[55] J. Nelayah et al. “Mapping surface plasmons on a single metallic nanoparticle”. In: *Nature Physics* 3 (2007), pp. 348–353.

[56] J. Radon. “Über die Bestimmung von Funktionen durch ihre Integralwerte lngs gewisser Mannigfaltigkeiten”. In: *Berichte ber die Verhandlungen der Königlich-Sächsischen Akademie der Wissenschaften zu Leipzig, Mathematisch-Physische Klasse* 69 (1917), pp. 262–277.

[57] B. RN. “Two-dimensional Aerial Smoothing in Radio Astronomy”. In: *Australian Journal of Physics* 9 (1956), 297314.

[58] A. M. Cormack. “Representation of a Function by Its Line Integrals, with Some Radiological Applications”. In: *Journal of Applied Physics* 34.9 (1963), pp. 2722–2727. DOI: http://dx.doi.org/10.1063/1.1729798. URL: http://scitation.aip.org/content/aip/journal/jap/34/9/10.1063/1.1729798.

[59] P. Midgley and M. Weyland. “3D electron microscopy in the physical sciences: the development of Z-contrast and {EFTEM} tomography”. In: *Ultramicroscopy* 96.34

(2003). Proceedings of the International Workshop on Strategies and Advances in Atomic Level Spectroscopy and Analysis, pp. 413 –431. ISSN: 0304-3991. DOI: http://dx.doi.org/10.1016/S0304-3991(03)00105-0. URL: http://www.sciencedirect.com/science/article/pii/S0304399103001050.

[60] N. W. Bigelow et al. "Characterization of the Electron- and Photon-Driven Plasmonic Excitations of Metal Nanorods". In: *ACS Nano* 6 (2012), pp. 7497–7504.

[61] H. CP et al. "Study of plasmon resonance in a gold nanorod with an LC circuit model". In: *Optics Express* 17.8 (2009), pp. 6407–6413.

[62] U. Hohenester, H. Ditlbacher, and J. R. Krenn. "Electron-Energy-Loss Spectra of Plasmonic Nanoparticles". In: *Phys. Rev. Lett.* 103 (2009), p. 106801.

[63] A. Alù, A. Salandrino, and N. Engheta. "Negative effective permeability and left-handed materials at optical frequencies". In: *Opt. Express* 14.4 (2006), pp. 1557–1567.

[64] A. Alú and N. Engheta. "The quest for magnetic plasmons at optical frequencies". In: *Optics Express* 17.7 (2009), pp. 5723–5730.

[65] A. Alù and N. Engheta. "Dynamical theory of artificial optical magnetism produced by rings of plasmonic nanoparticles". In: *Phys. Rev. B* 78 (2008), p. 085112.

[66] A. K. Sarychev, G. Shvets, and V. M. Shalaev. "Magnetic plasmon resonance". In: *Physical Review E* 73.3 (2006), p. 036609.

[67] N. W. Bigelow et al. “Signatures of Fano Interferences in the Electron Energy Loss Spectroscopy and Cathodoluminescence of Symmetry-Broken Nanorod Dimers”. In: *ACS Nano* 7 (2013), pp. 4511–4519.

[68] U. Fano. “Effects of Configuration Interaction on Intensities and Phase Shifts”. In: *Phys. Rev.* 124 (1961), pp. 1866–1878.

[69] C. L. G. Alzar, M. A. G. Martinez, and P. Nussenzveig. “Classical analog of electromagnetically induced transparency”. In: *American Journal of Physics* 70.1 (2002), pp. 37–41.

[70] A. Vittorini-Orgeas and A. Bianconi. “From Majorana Theory of Atomic Autoionization to Feshbach Resonances in High Temperature Superconductors”. English. In: *Journal of Superconductivity and Novel Magnetism* 22.3 (2009), pp. 215–221. ISSN: 1557-1939. DOI: 10.1007/s10948-008-0433-x. URL: http://dx.doi.org/10.1007/s10948-008-0433-x.

[71] J. B. Lassiter et al. “Designing and deconstructing the Fano lineshape in plasmonic nanoclusters”. In: *Nano Letters* 12 (2011), pp. 1058–1062.

[72] N. W. Bigelow et al. “Signatures of Fano Interferences in the Electron Energy Loss Spectroscopy and Cathodoluminescence of Symmetry-Broken Nanorod Dimers”. In: *ACS Nano* 7.5 (2013), pp. 4511–4519.

[73] S. Zhang et al. “Substrate-Induced Fano Resonances of a Plasmonic Nanocube: A Route to Increased-Sensitivity Localized Surface Plasmon Resonance Sensors Revealed”. In: *Nano Letters* 11.4 (2011), pp. 1657–1663. DOI: 10.1021/nl200135r.

eprint: http://pubs.acs.org/doi/pdf/10.1021/nl200135r. URL: http://pubs.acs.org/doi/abs/10.1021/nl200135r.

[74] D. Pines and D. Bohm. "A Collective Description of Electron Interactions: II. Collective vs Individual Particle Aspects of the Interactions". In: *Phys. Rev.* 85 (2 1952), pp. 338–353. DOI: 10.1103/PhysRev.85.338.

[75] H. Raether, ed. *Excitation of Plasmons and Interband Transitions by Electrons*. Berlin: Springer-Verlag, 1980.

[76] R. H. Ritchie and A. Howie. "Electron-Excitation and Optical-Potential in Electron-Microscopy". In: *Philos. Mag.* 36 (1977), p. 463.

[77] J. Nelayah et al. "Mapping Surface Plasmons on a Single Metallic Nanoparticle". In: *Nat. Phys.* 3 (2007), p. 348.

[78] J. Nelayah et al. "Two-Dimensional Quasistatic Stationary Short Range Surface Plasmons in Flat Nanoprisms". In: *Nano Lett.* 10.3 (2010), pp. 902–907.

[79] H. Duan et al. "Nanoplasmonics: Classical down to the Nanometer Scale". In: *Nano Lett.* 12 (2012), pp. 1683–1689.

[80] J. A. Scholl, A. Koh, and J. A. Dionne. "Quantum plasmon resonances of individual metallic nanoparticles". In: *Nature* 483 (2012), p. 421.

[81] A. L. Koh et al. "Electron Energy-Loss Spectroscopy (EELS) of Surface Plasmons in Single Silver Nanoparticles and Dimers: Influence of Beam Damage and Mapping of Dark Modes". In: *ACS Nano* 3 (2009), pp. 3015–3022.

[82] B. S. Guiton et al. “Correlated Optical Measurements and Plasmon Mapping of Silver Nanorods”. In: *Nano Lett.* 11 (2011), pp. 3482–3488.

[83] O. Nicoletti et al. “Surface plasmon modes of a single silver nanorod: an electron energy loss study”. In: *Opt. Express* 19 (2011), pp. 15371–15379.

[84] M.-W. Chu et al. “Probing Bright and Dark Surface-Plasmon Modes in Individual and Coupled Noble Metal Nanoparticles Using an Electron Beam”. In: *Nano Lett.* 9 (2009), pp. 399–404.

[85] S. Mazzucco et al. “Ultralocal Modification of Surface Plasmons Properties in Silver Nanocubes”. In: *Nano Lett.* 12 (2012), pp. 1288–1294.

[86] V. Myroshnychenko et al. “Plasmon Spectroscopy and Imaging of Individual Gold Nanodecahedra: A Combined Optical Microscopy, Cathodoluminescence, and Electron Energy-Loss Spectroscopy Study”. In: *Nano Lett.* asap (2012).

[87] A. Yurtsever and A. H. Zewail. “Direct Visualization of Near-Fields in Nanoplasmonics and Nanophotonics”. In: *Nano Lett.* 12 (2012), pp. 3334–3338.

[88] A. Yurtsever, R. M. van der Veen, and A. H. Zewail. “Subparticle Ultrafast Spectrum Imaging in 4D Electron Microscopy”. In: *Science* 335 (2012), pp. 59–64.

[89] N. Mirsaleh-Kohan et al. “Single-Molecule Surface-Enhanced Raman Scattering: Can STEM/EELS Image Electromagnetic Hot Spots?” In: *Journal of Physical Chemistry Letters* 3 (2012), pp. 2303–2309.

[90] P. D. Nellist and S. J. Pennycook. “Subangstrom Resolution by Underfocused Incoherent Transmission Electron Microscopy”. In: *Phys. Rev. Lett.* 81 (1998), p. 4156.

[91] E. Prodan et al. "A Hybridization Model for the Plasmon Response of Complex Nanostructures". In: *Science* 302 (2003), p. 419.

[92] F. J. García de Abajo and A. Howie. "Retarded field calculation of electron energy loss in inhomogeneous dielectrics". In: *Phys. Rev. B* 65 (2002), p. 115418.

[93] C. Matyssek et al. "The T-Matrix method in electron energy loss and cathodoluminescence spectroscopy calculations for metallic nano-particles". In: *Ultramicroscopy* 117 (2012), pp. 46 –52.

[94] A. L. Koh et al. "High-Resolution Mapping of Electron-Beam-Excited Plasmon Modes in Lithographically Defined Gold Nanostructures". In: *Nano Lett.* 11 (2011), pp. 1323–1330.

[95] D. P. Fussell, R. C. McPhedran, and C. Martijn de Sterke. "Decay rate and level shift in a circular dielectric waveguide". In: *Phys. Rev. A* 71 (2005), p. 013815.

[96] L. Novotny and B. Hecht, eds. *Principles of Nano-Optics*. Cambridge: Cambridge University Press, 2006.

[97] F. J. García de Abajo and M. Kociak. "Probing the Photonic Local Density of States with Electron Energy Loss Spectroscopy". In: *Phys. Rev. Lett.* 100 (2008), p. 106804.

[98] K. L. Kelly et al. "The Optical Properties of Metal Nanoparticles: The Influence of Size, Shape, and Dielectric Environment". In: *J. Phys. Chem. B* 107 (2003), p. 668.

[99] B. T. Draine and J. Goodman. "Beyond Clausius-Mossotti: Wave propagation on a polarizable point lattice and the discrete dipole approximation". In: *Astrophys. J.* 405 (1993), p. 685.

[100] D. J. Masiello. "Theory of Molecular Plasmonics and Optics on the Nanoscale". Masiello Group Website, Theory of Molecular Plasmonics and Optics on the Nanoscale. http://faculty.washington.edu/masiello.

[101] P. B. Johnson and R. W. Christy. "Optical Constants of the Noble Metals". In: *Phys. Rev. B* 6 (1972), p. 4370.

[102] D. W. Lynch and W. R. Hunter. "Handbook of Optical Constants of Solids". In: ed. by E. D. Palik. New York: Academic Press, 1985, pp. 275–367.

[103] Y. Wang et al. "A method to correlate optical properties and structures of metallic nanoparticles". In: *Ultramicroscopy* 109 (2009), p. 1110.

[104] M. Fleischmann, P. J. Hendra, and A. J. McQuillan. "Raman spectra of pyridine adsorbed at a silver electrode". In: *Chem. Phys. Lett.* 26 (1974), p. 163.

[105] M. G. Albrecht and J. A. Creighton. "Anomalously intense Raman spectra of pyridine at a silver electrode". In: *Journal of the American Chemical Society* 99.15 (1977), pp. 5215–5217.

[106] D. L. Jeanmaire and R. P. Van Duyne. "Surface Raman spectroelectrochemistry: Part I. Heterocyclic, aromatic, and aliphatic amines adsorbed on the anodized silver electrode". In: *J. Electroanal. Chem.* 84 (1977), p. 1.

[107] S. A. Maier et al. "Plasmonics - A Route to Nanoscale Optical Devices". In: *Advanced Materials* 13 (2001), p. 1501.

[108] M. Moskovits. "Surface-enhanced spectroscopy". In: *Rev. Mod. Phys.* 57 (1985), p. 783.

[109] E. C. Le Ru, P. G. Etchegoin, and Meyer. "Enhancement Factor Distribution around a Single Surface-Enhanced Raman Scattering Hot Spot and Its Relation to Single Molecule Detection". In: *Journal of Chemical Physics* 125 (2006), p. 204701.

[110] J. A. Dieringer et al. "Frequency Domain Existence Proof of Single-Molecule Surface-Enhanced Raman Spectroscopy." In: *The Journal of the American Chemical Society* 129 (2007), 1624916256.

[111] P. G. Etchegoin and E. C. Le Ru. "A perspective on single molecule SERS: current status and future challenges". In: *Phys. Chem. Chem. Phys.* 10 (40 2008), pp. 6079–6089.

[112] H. X. Xu et al. "Electromagnetic Contributions to Single-Molecule Sensitivity in Surface-Enhanced Raman Scattering". In: *Physical Review E* 62 (2000), pp. 4318–4324.

[113] T. R. Jensen et al. "Nanosphere Lithography: Tunable Localized Surface Plasmon Resonance Spectra of Silver Nanoparticles". In: *Journal of Physical Chemistry B* 104 (2000), 1054910556.

[114] E. Petryayeva and U. J. Krull. "Localized Surface Plasmon Resonance: Nanostructures, Bioassays and Biosensing A Review". In: *Anal. Chim. Acta* 706 (2011), pp. 8–24.

[115] M. Fan, G. F. S. Andrade, and A. G. Brolo. "A Review on the Fabrication of Substrates for Surface Enhanced Raman Spectroscopy and Their Applications in Analytical Chemistry". In: *Anal. Chim. Acta* 693 (2011), pp. 7–25.

[116] G. C. Schatz and R. P. Van Duyne. "Handbook of vibrational spectroscopy". In: John Wiley & Sons, 2002. Chap. Electromagnetic mechanism of surface-enhanced spectroscopy.

[117] P. Johansson, H. Xu, and M. Käll. "Surface-enhanced Raman scattering and fluorescence near metal nanoparticles". In: *Phys. Rev. B* 72 (2005), p. 035427.

[118] E. C. Le Ru, M. Meyer, and P. G. Etchegoin. "Proof of Single-Molecule Sensitivity in Surface Enhanced Raman Scattering (SERS) by Means of a Two-Analyte Technique". In: *The Journal of Physical Chemistry B* 110.4 (2006), pp. 1944–1948.

[119] D. C. Marinica et al. "Quantum Plasmonics: Nonlinear Effects in the Field Enhancement of a Plasmonic Nanoparticle Dimer". In: *Nano Letters* 12 (2012), pp. 1333–1339.

[120] E. C. Le Ru et al. "Surface Enhanced Raman Scattering Enhancement Factors: A Comprehensive Study". In: *Journal of Physical Chemistry C* 111 (2007), pp. 13794–13803.

[121] J. Gersten and A. Nitzan. "Electromagnetic theory of Raman scattering by molecules adsorbed on rough surfaces". In: *J. Chem. Phys.* 73 (1980), p. 3023.

[122] H. Metiu and P. Das. "The Electromagnetic Theory of Surface Enhanced Spectroscopy". In: *Annu. Rev. Phys. Chem.* 35 (1984), p. 507.

[123] A. M. Michaels, J. Jiang, and L. Brus. "urface Enhanced Raman Spectroscopy of Individual Rhodamine 6G Molecules on Large Ag Nanocrystals". In: *Journal of the American Chemical Society* 121 (1999), 99329939.

[124] K. L. Wustholz et al. "Structure-Activity Relationships in Gold Nanoparticle Dimers and Trimers for Surface-Enhanced Raman Spectroscopy". In: *J. Am. Chem. Soc.* 132 (2010), pp. 10903–10910.

[125] H. Cang et al. "Probing the electromagnetic field of a 15-nanometre hotspot by single molecule imaging". In: *Nature* 469 (2011), p. 385.

[126] S. M. Stranahan and K. A. Willets. "Super-resolution Optical Imaging of Single-Molecule SERS Hot Spots". In: *Nano Lett.* 10 (2010), pp. 3777–3784.

[127] K. A. Willets, S. M. Stranahan, and M. L. Weber. "Shedding Light on Surface-Enhanced Raman Scattering Hot Spots through Single-Molecule Super-Resolution Imaging". In: *J. Phys. Chem. Lett.* 3 (2012), 12861294.

[128] M. Bosman et al. "Mapping surface plasmons at the nanometre scale with an electron beam". In: *Nanotechnology* 18.16 (2007), p. 165505.

[129] B. S. Guiton et al. "Correlated optical measurements and plasmon mapping of silver nanorods". In: *Nano Letters* 11.8 (2011), pp. 3482–3488.

[130] P. G. Etchegoin et al. "Statistics of Single-Molecule Surface Enhanced Raman Scattering Signals: Fluctuation Analysis with Multiple Analyte Techniques". In: *Anal. Chem.* 79 (2007), pp. 8411–8415.

[131] S. Nie and S. Emory. "Probing Single Molecules and Single Nanoparticles by Surface-Enhanced Raman Scattering". In: *Science* 275 (1997), p. 1102.

[132] H Rose. "Image-Formation by Inelastically Scattered Electrons in Electron-Microscopy". In: *Optik* 45 (1976), pp. 139–158.

[133] D. A. Muller and J. Silcox. “Delocalization in Inelastic-Scattering”. In: *Ultramicroscopy* 59 (1995), pp. 195–213.

[134] M. R. Keenan. “Exploiting Spatial-Domain Simplicity in Spectral Image Analysis”. In: *Surf. Interface Anal.* 41 (2009), pp. 79–87.

[135] P. G. Kotula, M. R. Keenan, and J. R. Michael. “Automated Analysis of SEM X-Ray Spectral Images: A Powerful New Microanalysis Tool”. In: *Microsc. Microanal.* 9 (2003), 117.

[136] B. T. Draine and P. J. Flatau. “Discrete-Dipole Approximation for Periodic Targets: Theory and Tests”. In: *J. Opt. Soc. Am. A* 25 (2008), 26932703.

[137] A. A. Lazarides et al. “Optical Properties of Metal Nanoparticles and Nanoparticle Aggregates Important in Biosensors”. In: *J. Mol. Struc. Theochem.* 529 (2000), pp. 59–63.

[138] A. Alù and N. Engheta. “Achieving transparency with plasmonic and metamaterial coatings”. In: *Physical Review E* 72.1 (2005), p. 016623.

[139] J. Pendry et al. “Extremely low frequency plasmons in metallic mesostructures”. In: *Physical Review Letters* 76.25 (1996), p. 4773.

[140] J. A. Fan et al. “Self-Assembled Plasmonic Nanoparticle Clusters”. In: *Science* 328 (2010), pp. 1135–1138.

[141] S. N. Sheikholeslami, A. García-Etxarri, and J. A. Dionne. “Controlling the interplay of electric and magnetic modes via Fano-like plasmon resonances”. In: *Nano Letters* 11.9 (2011), pp. 3927–3934.

[142] N. Liu et al. “Magnetic Plasmon Formation and Propagation in Artificial Aromatic Molecules”. In: *Nano Letters* 12.1 (2012), pp. 364–369.

[143] N. Liu et al. “Manipulating Magnetic Plasmon Propagation in Metallic Nanocluster Networks”. In: *ACS Nano* 6.6 (2012), pp. 5482–5488.

[144] H Liu et al. “Magnetic plasmon propagation along a chain of connected subwavelength resonators at infrared frequencies”. In: *Physical Review Letters* 97.24 (2006), p. 243902.

[145] H Liu et al. “Magnetic plasmon hybridization and optical activity at optical frequencies in metallic nanostructures”. In: *Physical Review B* 76.7 (2007), p. 073101.

[146] D. Zhu, M. Bosman, and J. K. W. Yang. “A circuit model for plasmonic resonators”. In: *Opt. Express* 22.8 (2014), pp. 9809–9819. DOI: 10.1364/OE.22.009809. URL: http://www.opticsexpress.org/abstract.cfm?URI=oe-22-8-9809.

[147] E. Prodan et al. “A hybridization mdoel for the plasmon response of complex nanostructures”. In: *Science* 302 (2003), pp. 419–422.

[148] F. Wen et al. “Plasmon transmutation: inducing new modes in nanoclusters by adding dielectric nanoparticles”. In: *Nano Letters* 12.9 (2012), pp. 5020–5026.

[149] S. Campione et al. “Enhanced magnetic and electric fields via Fano resonances in metasurfaces of circular clusters of plasmonic nanoparticles”. In: *ACS Photonics* 1.3 (2014), pp. 254–260.

[150] S. N. Sheikholeslami et al. “A metafluid exhibiting strong optical magnetism”. In: *Nano Letters* 13.9 (2013), pp. 4137–4141.

[151] J. Wang et al. "Double Fano resonances due to interplay of electric and magnetic plasmon modes in planar plasmonic structure with high sensing sensitivity". In: *Optics Express* 21.2 (2013), pp. 2236–2244.

[152] H. Alaeian and J. A. Dionne. "Plasmon nanoparticle superlattices as optical-frequency magnetic metamaterials". In: *Optics Express* 20.14 (2012), pp. 15781–15796.

[153] Z. Zhu et al. "Metallic nanofilm half-wave plate based on magnetic plasmon resonance". In: *Optics Letters* 37.4 (2012), pp. 698–700.

[154] A. E. Miroshnichenko et al. "Optically induced interaction of magnetic moments in hybrid metamaterials". In: *ACS Nano* 6.1 (2011), pp. 837–842.

[155] C. Tang et al. "Magnetic field enhancement at optical frequencies through diffraction coupling of magnetic plasmon resonances in metamaterials". In: *Physical Review B* 83.4 (2011), p. 041402.

[156] J. Cao et al. "High sensing properties of magnetic plasmon resonance in the double-rod and tri-rod structures". In: *Applied Physics Letters* 97.7 (2010), p. 071905.

[157] K. H. Li and B. B. Yellen. "Magnetically tunable self-assembly of colloidal rings". In: *Applied Physics Letters* 97.8 (2010), p. 083105.

[158] Y. Lu et al. "Magnetic plasmon resonance: underlying route to plasmonic electromagnetically induced transparency in metamaterials". In: *Physical Review B* 82.19 (2010), p. 195112.

[159] S. Wang et al. "The gain effect in a magnetic plasmon waveguide". In: *Applied Physics Letters* 96.11 (2010), p. 113103.

[160] M. S. Wheeler, J. S. Aitchison, and M. Mojahedi. "Coupled magnetic dipole resonances in sub-wavelength dielectric particle clusters". In: *Journal of the Optical Society of America B* 27.5 (2010), pp. 1083–1091.

[161] C Zhu et al. "Electric and magnetic excitation of coherent magnetic plasmon waves in a one-dimensional meta-chain". In: *Optics Express* 18.25 (2010), pp. 26268–26273.

[162] Z. Hao and A. Chubukov. "Resonance peak in neutron scattering experiments on the cuprates revisited: The case of exciton versus π-resonance and magnetic plasmon". In: *Physical Review B* 79.22 (2009), p. 224513.

[163] T Li et al. "Structural-configurated magnetic plasmon bands in connected ring chains". In: *Optics Express* 17.14 (2009), pp. 11486–11494.

[164] H Liu et al. "Coupled magnetic plasmons in metamaterials". In: *Physica Status Solidi (B)* 246.7 (2009), pp. 1397–1406.

[165] H Liu et al. "Extraordinary optical transmission induced by excitation of a magnetic plasmon propagation mode in a diatomic chain of slit-hole resonators". In: *Physical Review B* 79.2 (2009), p. 024304.

[166] Z. Zhu et al. "Optically pumped nanolaser based on two magnetic plasmon resonance modes". In: *Applied Physics Letters* 94.10 (2009), p. 103106.

[167] T. Li et al. "Dispersion of magnetic plasmon polaritons in perforated trilayer metamaterials". In: *Journal of Applied Physics* 103.2 (2008), p. 023104.

[168] T. Li et al. "Magnetic resonance hybridization and optical activity of microwaves in a chiral metamaterial". In: *Applied Physics Letters* 92.13 (2008), p. 131111.

[169] N. Liu et al. “Plasmonic Building Blocks for Magnetic Molecules in Three-Dimensional Optical Metamaterials”. In: *Advanced Materials* 20.20 (2008), pp. 3859–3865.

[170] D. Lu et al. “Creation of a magnetic plasmon polariton through strong coupling between an artificial magnetic atom and the defect state in a defective multilayer microcavity”. In: *Physical Review B* 77.21 (2008), p. 214302.

[171] S. Wang et al. “Magnetic plasmon modes in periodic chains of nanosandwiches”. In: *Optics Express* 16.6 (2008), pp. 3560–3565.

[172] T. Li et al. “Exploring magnetic plasmon polaritons in optical transmission through hole arrays perforated in trilayer structures”. In: *Applied Physics Letters* 90.25 (2007), p. 251112.

[173] T. Pakizeh et al. “Magnetic-field enhancement in gold nanosandwiches”. In: *Optics Express* 14.18 (2006), pp. 8240–8246.

[174] A. K. Sarychev and V. M. Shalaev. “Magnetic Resonance in Metal Nanoantennas”. In: *Proc. of SPIE* 5508 (2004), p. 129.

[175] J Yang et al. “Magnetic-electric interference in metal-dielectric-metal oligomers: generation of magneto-electric Fano resonance”. In: *Optical Materials Express* 2.10 (2012), pp. 1407–1415.

[176] P. C. Wu et al. “Magnetic plasmon induced transparency in three-dimensional metamolecules”. In: *Nanophotonics* 1.2 (2012), pp. 131–138.

[177] A. Nazir et al. “Fano coil-type resonance for magnetic hot-spot generation”. In: *Nano Letters* (2014).

[178] B. Ögüt et al. “Toroidal plasmonic eigenmodes in oligomer nanocavities for the visible”. In: *Nano Letters* 12.10 (2012), pp. 5239–5244.

[179] N. Talebi et al. “On the symmetry and topology of plasmonic eigenmodes in heptamer and hexamer nanocavities”. In: *Applied Physics A* (2014), pp. 1–8.

[180] A. Guerrero-Martínez, M. Grzelczak, and L. M. Liz-Marzán. “Molecular thinking for nanoplasmonic design”. In: *ACS Nano* 6.5 (2012), pp. 3655–3662.

[181] E. N. Economou. *Green’s functions in quantum physics*. Vol. 3. Springer, 1984.

[182] P. Echenique, A. Howie, and D. Wheatley. “Excitation of dielectric spheres by external electron beams”. In: *Philosophical Magazine B* 56.3 (1987), pp. 335–349.

[183] J. Crowell and R. Ritchie. “Radiative decay of Coulomb-stimulated plasmons in spheres”. In: *Physical Review* 172 (1968), pp. 436–440.

[184] A. Lucas and M. Sunjic. “Fast-electron spectroscopy of surface excitations”. In: *Physical Review Letters* 26 (1971), pp. 229–232.

[185] G. Lipworth et al. “Magnetic Metamaterial Superlens for Increased Range Wireless Power Transfer”. In: *Scientific reports* 4 (2014).

[186] L Palma-Chilla, J. Flores, and P. Vega-Jorquera. “Connections between the dissipated energy of right-handed and left-handed systems: electric and magnetic origin”. In: *Journal of Electromagnetic Waves and Applications* 28.2 (2014), pp. 129–137.

[187] W. M. Zhu et al. “Switchable Magnetic Metamaterials Using Micromachining Processes”. In: *Advanced Materials* 23.15 (2011), pp. 1792–1796. ISSN: 1521-4095. DOI: 10.1002/adma.201004341. URL: http://dx.doi.org/10.1002/adma.201004341.

[188] M. W. Klein et al. "Second-harmonic generation from magnetic metamaterials". In: *Science* 313.5786 (2006), pp. 502–504.

[189] C Enkrich et al. "Magnetic metamaterials at telecommunication and visible frequencies". In: *Physical Review Letters* 95.20 (2005), p. 203901.

[190] S O'Brien et al. "Near-infrared photonic band gaps and nonlinear effects in negative magnetic metamaterials". In: *Physical Review B* 69.24 (2004), p. 241101.

[191] M. Ausloos, P. Clippe, and A. A. Lucas. "Infrared active modes in large clusters of spheres". In: *Phys. Rev. B* 18 (12 1978), pp. 7176–7185. DOI: 10.1103/PhysRevB.18.7176. URL: http://link.aps.org/doi/10.1103/PhysRevB.18.7176.

[192] G. Fujii, D. Fukuda, and S. Inoue. "Direct observation of bosonic quantum interference of surface plasmon polaritons using photon-number-resolving detectors". In: *Phys. Rev. B* 90 (8 2014), p. 085430. DOI: 10.1103/PhysRevB.90.085430. URL: http://link.aps.org/doi/10.1103/PhysRevB.90.085430.

[193] J. S. Fakonas et al. "Two-plasmon quantum interference". In: *Nat. Photon.* 8 (2014), pp. 317–320.

[194] B. Willingham and S. Link. "A Kirchhoff solution to plasmon hybridization". English. In: *Applied Physics B* 113.4 (2013), pp. 519–525. ISSN: 0946-2171. DOI: 10.1007/s00340-013-5501-7. URL: http://dx.doi.org/10.1007/s00340-013-5501-7.

[195] P. W. Atkins. *Physical Chemistry*. 6th ed. Oxford University Press, 1998.

[196] N. Verellen et al. "Fano resonances in individual coherent plasmonic nanocavities". In: *Nano Letters* 9.4 (2009), pp. 1663–1667.

[197] Y. Sonnefraud et al. “Experimental realization of subradiant, superradiant, and Fano resonances in ring/disk plasmonic nanocavities”. In: *ACS Nano* 4.3 (2010), pp. 1664–1670.

[198] K. Suenaga et al. “Visualizing and identifying single atoms using electron energy-loss spectroscopy with low accelerating voltage”. In: *Nat. Chem.* 1.5 (2009), pp. 415–418.

[199] B. Schaffer et al. “Comparison of EFTEM and STEM EELS plasmon imaging of gold nanoparticles in a monochromated TEM”. In: *Ultramicroscopy* 110.8 (2010), pp. 1087 –1093.

[200] G. Bourdarham et al. “Spectral imaging of individual split-ring resonators”. In: *Phys. Rev. Lett.* 105.255501 (2010).

[201] M. Bosman et al. “Surface plasmon damping quantified with an electron nanoprobe”. In: *Sci. Rep.* 3.1312 (2012).

[202] I. Alber et al. “Visualization of Multipolar Longitudinal and Transversal Surface Plasmon Modes in Nanowire Dimers”. In: *ACS Nano* 5.12 (2011), pp. 9845–9853.

[203] I. Alber et al. “Multipole Surface Plasmon Resonances in Conductively Coupled Metal Nanowire Dimers”. In: *ACS Nano* 6.11 (2012), pp. 9711–9717.

[204] Y. Yamamoto, K. Araya, and F. J. García de Abajo. “Photon emission from silver particles induced by a high-energy electron beam”. In: *Phys. Rev. B* 64, 205419 (2001), p. 9.

[205] E. J. R. Vesseur et al. "Direct Observation of Plasmonic Modes in Au Nanowires Using High-Resolution Cathodoluminescence Spectroscopy". In: *Nano Letters* 7.9 (2007), pp. 2843–2846.

[206] R Gómez-Medina et al. "Mapping plasmons in nanoantennas via cathodoluminescence". In: *New Journal of Physics* 10.10 (2008), p. 105009.

[207] S. Lazar, G. A. Botton, and H. W. Zandbergen. "Enhancement of resolution in core-loss and low-loss spectroscopy in a monochromated microscope". In: *Ultramicroscopy* 11.4 (2006), pp. 1091–1103.

[208] O. L. Krivanek et al. "High-energy-resolution monochromator for aberration-corrected scanning transmission electron microscopy/electron energy-loss spectroscopy". In: *Philos. Trans. R. Soc. A-Math. Phys Eng. Sci* 367.1908 (2009), pp. 3683–3697.

[209] S. group. "SOPRA n&k optical database". SOPRA n&k optical database (available at http://www.sopra-sa.com/more/database.asp).

[210] S. A. Maier. *Plasmonics: Fundamentals and Applications,* 1^{st} *ed.* New York: Springer-Verlag, 2007.

[211] D. Jeanmaire and R. VanDuyne. "Surface Raman spectroelectrochemistry. 1. Heterocyclic, aromatic, and aliphatic-amines adsorbed on anodized silver electrode". In: *J. Electroanal. Chem.* 84.1 (1977), pp. 1–20.

[212] D. B. Ingram and S. Linic. "Water Splitting on Composite Plasmonic-Metal/Semiconductor Photoelectrodes: Evidence for Selective Plasmon-Induced Formation of Charge Carriers near the Semiconductor Surface". In: *Journal of the American Chemical Society* 133.14 (2011), pp. 5202–5205.

[213] M. Quinten et al. “Electromagnetic energy transport via linear chains of silver nanoparticles”. In: *Opt. Lett.* 23.17 (1998), pp. 1331–1333.

[214] S. A. Maier et al. “Local detection of electromagnetic energy transport below the diffraction limit in metal nanoparticle plasmon waveguides”. In: *Nat. Mater.* 2.4 (2003), pp. 229–232.

[215] M. I. Stockman. “Nanofocusing of optical energy in tapered plasmonic waveguides”. In: *Phys. Rev. Lett.* 93 (2004), pp. 137404–137404.

[216] R. F. Oulton et al. “hybrid plasmonic waveguide for subwavelength confinement and long-range propagation”. In: *Nat. Photonics* 2.8 (2008), pp. 496–500.

[217] S. A. Maier. “Plasmonics: Metal nanostructures for subwave-length photonic devices”. In: *IEEE J. Sel. Top. Quantum Electron.* 12.6 (2006), pp. 1214–1220.

[218] E. Ozbay. “Plasmonics: Merging photonics and electronics at nanoscale dimensions”. In: *Science* 311.5758 (2006), pp. 189–193.

[219] T. W. Ebbesen, C. Genet, and S. I. Bozhevolnyi. “Surface-plasmon circuitry”. In: *Phys. Today* 61.5 (2008), p. 44.

[220] J. Golab et al. “A surface enhanced hyper-Raman scattering study of pyridine adsorbed onto silver: Experiment and theory”. In: *J. Chem. Phys.* 88 (1988), p. 7942.

[221] K. Kneipp et al. “Surface-enhanced non-linear Raman scattering at the single-molecule level”. In: *Chem. Phys.* 247.1 (1999), pp. 155–162.

[222] J. Kneipp, H. Kneipp, and K. Kneipp. "Two-photon vibrational spectroscopy for biosciences based on surface-enhanced hyper-Raman scattering". In: *Proc. Natl. Acad. Sci. U. S. A.* 103.46 (2006), pp. 17149–17153.

[223] S. A. Maier. "Plasmonic field enhancement and SERS in the effective mode volume picture". In: *Opt. Express* 14.5 (2006), pp. 1957–1964.

[224] C. B. Milojevich et al. "Probing One-Photon Inaccessible Electronic States with High Sensitivity: Wavelength Scanned Surface Enhanced Hyper-Raman Scattering". In: *ChemPhysChem* 12 (2011), pp. 101–103.

[225] C. B. Milojevich et al. "Probing Two-Photon Properties of Molecules: Large Non-Condon Effects Dominate the Resonance Hyper-Raman Scattering of Rhodamine 6G". In: *Journal of the American Chemical Society* 133.37 (2011), pp. 14590–14592.

[226] E. Ringe et al. "Single nanoparticle plasmonics". In: *Phys. Chem. Chem. Phys.* 15.12 (2013), pp. 4110–4129.

[227] T. Sannomiya and J. Vörös. "Single plasmonic nanoparticles for biosensing". In: *Trends Biotechnol.* 29.7 (2011), pp. 343–351.

[228] J. M. McMahon, S. K. Gray, and G. C. Schatz. "Nonlocal optical response of metal nanostructures with arbitrary shape". In: *Phys. Rev. Lett.* 103 (2009), p. 097403.

[229] E. Ringe et al. "Unravelling the effects of size, compositoin, and substrate on the localized surface plasmon resonance frequencies of gold and silver nanocubes: a systematic single-particle approach". In: *J. Phys. Chem. C* 114 (2010), pp. 12511–12516.

[230] L. J. Sherry et al. “Localized surface plasmon resonance spectroscopy of single silver nanocubes”. In: *Nano Letters* 5.10 (2005), pp. 2034–2038.

[231] O. Schubert et al. “Mapping the polarization pattern of plasmon modes reveals nanoparticle symmetry”. In: *Nano Lett.* 8.8 (2008), pp. 2345–2350.

[232] H. Wei et al. “Multipolar plasmon resonances in individual Ag nanorice”. In: *ACS Nano* 4.5 (2010), pp. 2649–2654.

[233] A. Tcherniak et al. “Probing a century old prediction one plasmonic particle at a time”. In: *Nano Lett.* 10.4 (2010), pp. 1398–1404.

[234] E. Ringe et al. “Correlating the structure and localized surface plasmon resonance of single silver right bipyramids”. In: *Nanotechnology* 23.44 (2012), pp. 444005–444005.

[235] B. J. Wiley et al. “Synthesis and optical properties of silver nanobars and nanorice”. In: *Nano Lett.* 7.4 (2007), pp. 1032–1036.

[236] E. Ringe et al. “Plasmon length: A universal parameter to describe size effects in gold nanoparticles”. In: *J. Phys. Chem. Lett.* 3.11 (2012), pp. 1479–1483.

[237] J. J. Mock, D. R. Smith, and S. Schultz. “Local refractive index dependence of plasmon resonance spectra from individual nanoparticles”. In: *Nano Lett.* 3.4 (2003), pp. 485–491.

[238] L. M. Liz-Marzán. “Tailoring surface plasmons through the morphology and assembly of metal nanoparticles”. In: *Langmuir* 22.1 (2006), pp. 32–41.

[239] L. J. Sherry et al. “Localized surface plasmon resonance spectroscopy of single silver triangular nanoprisms”. In: *Nano Letters* 6.9 (2006), pp. 2060–2065.

[240] M.-W. Chu et al. “Probing Bright and Dark Surface-Plasmon Modes in Individual and Coupled Noble Metal Nanoparticles Using an Electron Beam”. In: *Nano Letters* 9.1 (2009), pp. 399–404.

[241] M. NGom et al. “Electron-beam mapping of plasmon resonances in electromagnetically interacting gold nanorods”. In: *Phys. Rev. B* 80, 113411 (2009).

[242] M. NGom et al. “Single Particle Plasmon Spectroscopy of Silver Nanowires and Gold Nanorods”. In: *Nano Letters* 8.10 (2008), pp. 3200–3204.

[243] J. Nelayah et al. “Direct imaging of surface plasmon resonances on single triangular silver nanoprisms at optical wavelengths using low-loss EFTEM imaging”. In: *Optics Letters* 34.7 (2009), pp. 1003–1005.

[244] P. Alonso-Gonzalez et al. “Real-space mapping of Fano interference in plasmonic metamolecules”. In: *Nano Lett.* 11.9 (2011), pp. 3922–3926.

[245] Z. Fang et al. “Removing a wedge from a metallic nanodisk reveals a Fano resonance”. In: *Nano Lett.* 11.10 (2011), pp. 4475–4479.

[246] J. Ye et al. “Plasmonic nanoclusters: Near field properties of the Fano resonance interrogated with SERS”. In: *Nano Lett.* 3.12 (2012), pp. 1660–1667.

[247] P. R. Edwards et al. “Mapping localized surface plasmons within silver nanocubes using cathodoluminescence hyperspectral imaging”. In: *Journal of Physical Chemistry C* 115.29 (2011), pp. 14031–14035.

[248] J. M. McMahon et al. “Correlating the structure, optical spectra, and electrodynamics of single silver nanocubes”. In: *J. Phys. Chem. C* 113.7 (2009), pp. 2731–2735.

[249] M. Rycenga et al. “Generation of hot spots with silver nanocubes for single-molecule detection by surface-enhanced Raman scattering”. In: *Angew. Chem., Int. Ed.* 50.24 (2011), pp. 5473–5477.

[250] D.-S. Kim et al. “Real-space mapping of the strongly coupled plasmons of nanoparticle dimers”. In: *Nano Lett.* 9.10 (2009), pp. 3619–3625.

[251] S. J. Guo et al. “Three-dimensional Pt-on-Au bimetallic dendritic nanoparticle: One-step, high-yield synthesis and its bifunctional plasmonic and catalytic properties”. In: *J. Phys. Chem. C* 114.36 (2010), pp. 15337–15342.

[252] A. Bogner et al. “A history of scanning electron microscopy developments: Towards wet-STEM imaging”. In: *Micron* 38.4 (2007), pp. 390–401.

[253] O. Nicoletti et al. “Three-dimensional imaging of localized surface plasmon resonances of metal nanoparticles”. In: *Nature* 502 (2013), p. 7469.

[254] V. Iberi, N. Mirsaleh-Kohan, and J. P. Camden. “Understanding plasmonic properties in metallic nanostructures by correlating photonic and electronic excitations”. In: *J. Phys. Chem. Lett.* 4.7 (2013), pp. 1070–1078.

[255] S. Bals et al. “Annular Dark Field Tomography in TEM”. In: *Microscopy and Microanalysis* 11 (2005), pp. 2118–2119.

[256] J. Canny. “A Computational Approach To Edge Detection”. In: *IEEE Trans. Pattern Analysis and Machine Intelligence* 8.6 (1986), 679698.

[257] P. F. Liao and A. Wokaun. “Lightning rod effect in surface enhanced Raman scattering”. In: *The Journal of Chemical Physics* 76.1 (1982), pp. 751–752.

[258] A. V. Ermushev et al. “Surface enhancement of local optical fields and the lightning-rod effect”. In: *Quantum Electronics* 23.5 (1993), p. 435.

[259] A. Einstein. “Zur Elektrodynamik bewegter Körper”. In: *Annalen der Physik* 17 (1905).